Computers & Structures Vol. 26, No. 1/2, pp. 357–409, 1987
Printed in Great Britain.

0045-7949/87 $3.00 + 0.00
Pergamon Journals Ltd.

A FINITE ELEMENT FORMULATION FOR NONLINEAR INCOMPRESSIBLE ELASTIC AND INELASTIC ANALYSIS

THEODORE SUSSMAN and KLAUS-JÜRGEN BATHE
Department of Mechanical Engineering,
Massachusetts Institute of Technology, Cambridge, MA 02139, U.S.A.

Abstract—We introduce a displacement–pressure (u/p) finite element formulation for the geometrically and materially nonlinear analysis of compressible and almost incompressible solids. The u/p formulation features the *a priori* replacement of the pressure computed from the displacement field by a separately interpolated pressure; this replacement is performed without reference to any specific material description. Considerations for incremental nonlinear analysis (including contact boundary conditions) are discussed and various u/p elements are studied. Numerical examples show the performance of the u/p formulation for two- and three-dimensional problems involving isotropic, orthotropic, rubber-like and elasto-plastic materials.

1. INTRODUCTION

A general numerical procedure for the analysis of solids and structures should be as robust as possible. The displacement-based finite element method is one such numerical procedure. In part, the effectiveness of the method is due to its conceptual simplicity. Assuming that the nodal point displacements of the finite element mesh completely specify the displacements in the body, an application of the principle of virtual work generates a set of simultaneous equations with the nodal point displacements as unknowns. The displacements can then be used to calculate strains, stresses and other quantities of interest. This procedure can be used for incremental nonlinear analysis, in which case the displacement increments are the principal unknowns [1].

Almost incompressible materials are commonly used in industry. Natural rubber is almost incompressible; the ratio of the bulk modulus to the shear modulus is typically several thousand [2]. Materials that undergo plastic deformations may also be considered as almost incompressible, because a material being plasticially deformed has an effective shear modulus that is much smaller than the bulk modulus.

The displacement-based finite element method can provide accurate solutions to problems involving almost incompressible materials; however, the number of elements required to obtain a given solution accuracy is usually far greater than the number of elements required in a comparable analysis involving compressible materials. In this respect, the displacement-based finite element method is not robust. To study these difficulties, consider a compressible linear isotropic material. Such a material has a pressure–strain relationship of the following form:

$$p = -\kappa e_{ii} \tag{1.1}$$

where p is the hydrostatic pressure, κ is the bulk modulus and

$$e_{ii} = \frac{\partial u_1}{\partial x_1} + \frac{\partial u_2}{\partial x_2} + \frac{\partial u_3}{\partial x_3} \tag{1.2}$$

is the volumetric strain. If we gradually enforce incompressibility, then κ increases to infinity, e_{ii} decreases to zero and p converges to some finite number. It is seen that in the totally incompressible case, eqn (1.1) cannot be used to calculate p. In fact, for a totally incompressible material, p is decoupled from the displacements and, in an analytical solution, must be calculated directly from the equilibrium equations. Therefore it is unreasonable to expect the displacement-based finite element method to predict the stresses within a totally incompressible material.

It is less obvious that the displacement-based finite element method has difficulties in the analysis of almost incompressible materials. These difficulties have been known for at least twenty years [3–6]. Reported undesirable characteristics include ill-conditioning of the stiffness matrix, spurious or incorrect stresses (particularly pressures) and 'locking' (loss of accuracy in the computed response as incompressibility is enforced). If the material is elastic–perfectly plastic, no limit loads may be obtained in limit load calculations [7].

As an example, we consider the linear analysis of the pressure vessel shown in Fig. 1.1. The displacement-based formulation is used with a mesh of 181 six- and eight-node elements (Fig. 1.2) and all stiffness matrices are integrated using 3×3 Gauss integration. This analysis was considered in detail in a previous paper [8]. First we consider $\nu = 0.40$ and plot pressure and effective stress bands (Fig. 1.3). It is seen that the mesh is fine enough for this problem. However, if we consider $\nu = 0.49$, with the same mesh, and plot pressure and effective stress bands

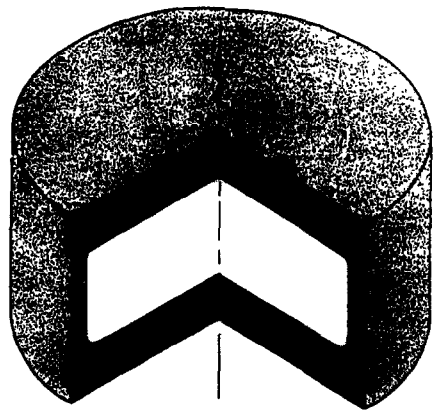

(a)

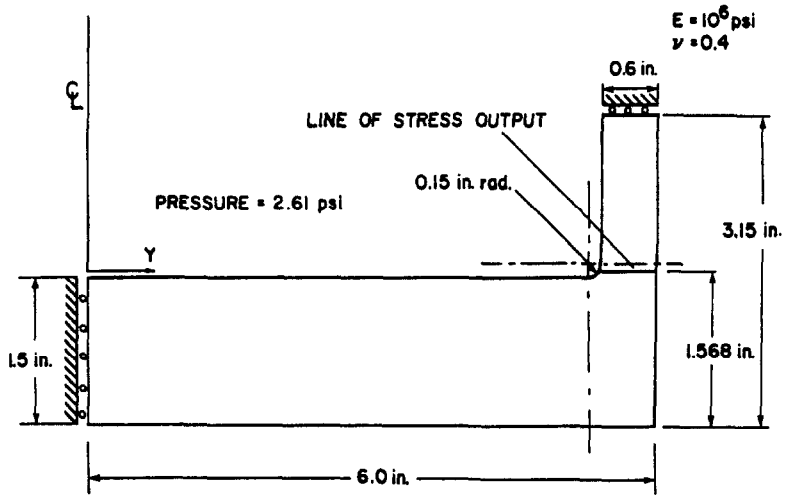

(b)

Fig. 1.1. Axisymmetric pressure vessel geometry. (a) Schematic drawing. (b) Dimensions.

(Fig. 1.4), it is observed that the pressure predictions have drastically deteriorated but that the effective stress predictions are still quite good.

For the above reasons, a great deal of research effort by engineers and mathematicians has been devoted to the development of the finite element method for the analysis of incompressible materials. A complete bibliography of related papers is beyond the scope of this paper, however one survey and discussion of recent work is given by Gadala [9]. We will only briefly describe some of the recent results that are most directly applicable to our paper.

All of the references cited below use the same basic principle—the separate interpolation of a stress variable that is related to the hydrostatic pressure. The differences are in the details of the formulations (for example, the elimination of the additional variables), the types of elements employed and the types of problems to which the formulations are applied.

Herrmann [3] presented a mixed variational formulation for incompressible isotropic materials. This formulation was one of the first to introduce a separately interpolated 'mean stress' parameter. Taylor *et al.* [10] and Key [5] presented different generalizations of Herrmann's formulation for incompressible orthotropic materials. Key's formulation is also applicable to nonlinear analysis. Oden and J. Key [4] presented a formulation for the nonlinear analysis of axisymmetric rubber solids. Nagtegaal *et al.* [7] proposed a mixed formulation for the analysis of elasto-plastic problems.

In the 1970s, many papers discussed some of the difficulties encountered when applying mixed formulations with various types of elements. It was quickly recognized that elements with equal-order interpolations for displacements and pressures are ineffective [11]. The low-order elements also presented difficulties. For example, it was recognized that the constant strain triangle with a separately interpolated pressure cannot be employed in certain analyses [6]. Also, the four-node isoparametric element with a constant pressure exhibits a spurious 'checkerboard' mode in certain problems when a regular mesh is used.

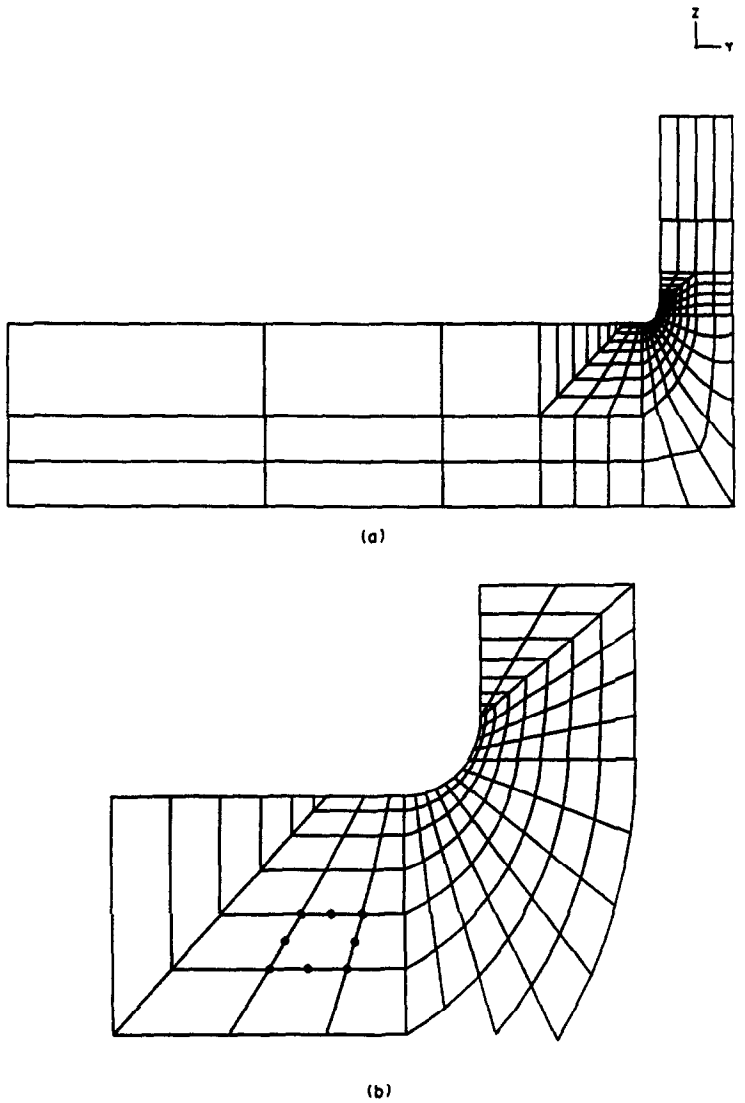

Fig. 1.2. One hundred and eighty-one eight-node element mesh for axisymmetric pressure vessel. (a) Complete mesh. (b) Detail of mesh.

A systematic mathematical investigation of these difficulties began with the derivation of the inf-sup condition independently by Brezzi [12] and Babuška [13, 14] in the early 1970s. Fortin [15] recast the Brezzi–Babuška condition into a more readily used form. The inf-sup condition was used by these researchers and Oden and Kikuchi [16] to analyze different mixed elements. As a result of these and other investigations, the nine-node isoparametric element with three pressure variables was shown to be an effective element for two-dimensional analysis (see also [17]).

Another research area explored in the mid 1970s was the replacement of mixed finite element formulations, in which the contributions corresponding to additional degrees of freedom are assembled into the global stiffness matrix, with equivalent 'displacement-based' finite element formulations. One approach is based on the use of reduced/selective integration: the volumetric terms in the stiffness matrix are integrated using a lower order of Gauss integration than is used to integrate the other terms. Malkus and Hughes [18] showed that selective integration can be equivalent to a mixed formulation, with the number of integration points used to evaluate the volumetric contributions equal to the number of pressure degrees of freedom used in the mixed formulation. The mathematical implications were also discussed by Oden and Kikuchi [16]. However, this strict equivalence only holds for certain types of elements under certain conditions (for example, quadratic isoparametric elements with straight sides) [19, 20]. The proper technique for eliminating the separate degrees of freedom, known as the 'consistent penalty method', is to introduce an artificial compressibility and then, for each element, to use full integration to form the (mixed formulation) element stiffness matrix. Static condensation is used to elimi-

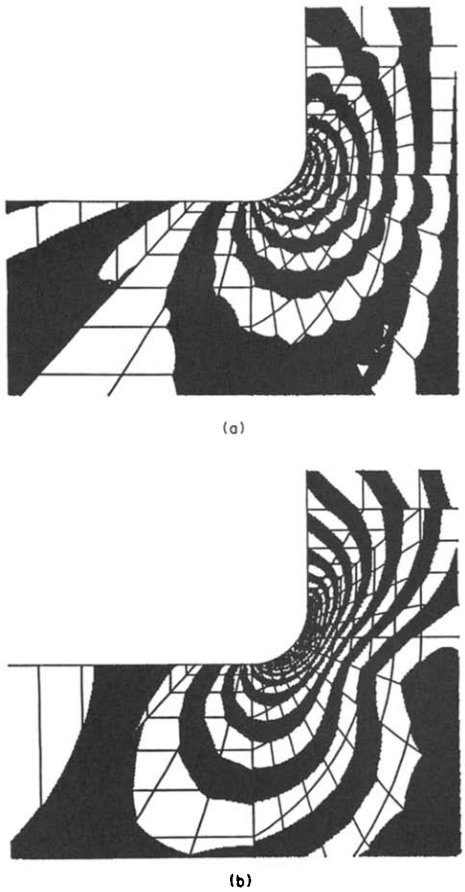

Fig. 1.3. Stress band plots for 181 eight-node element mesh, $\nu = 0.40$, band width = 2.5 psi. (a) Pressure band plot. (b) Effective stress band plot.

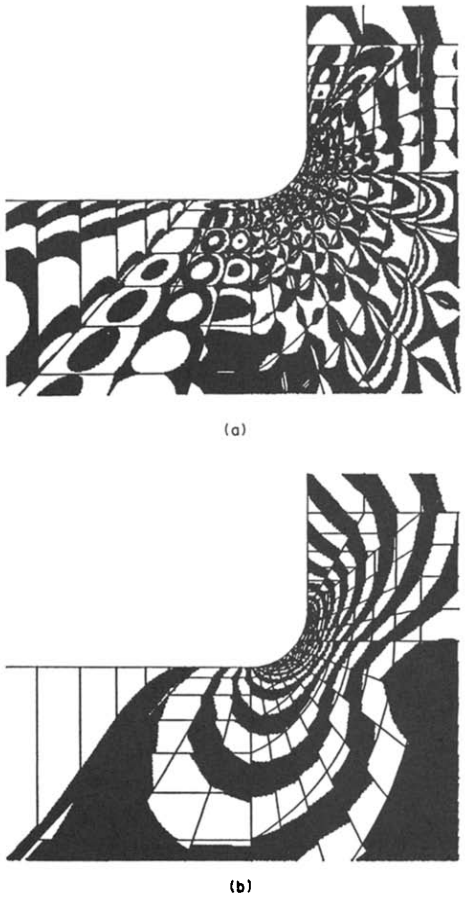

Fig. 1.4. Stress band plots for 181 eight-node element mesh, $\nu = 0.49$, band width = 2.5 psi. (a) Pressure band plot. (b) Effective stress band plot.

nate the pressure degrees of freedom at the element level and therefore the global stiffness matrix contains only displacement degrees of freedom. Bercovier [21] rigorously justified this procedure.

In the 1980s, researchers have made an effort to apply mixed formulations to the practical incremental nonlinear analysis of rubber components [22]. In many cases variants of a formulation presented by Bercovier *et al.* [19] were used [23–25]. The formulation of Zdunek and Bercovier [25] is particularly interesting because it explicitly treats the penalty parameter as a material property (the bulk modulus) and the pressure computed from the displacement field is removed completely from the stress calculations. One notable feature of the formulations discussed in [19, 22–25] is that the constraint equations are algebraically solved for the total pressures and this permits the element force vectors to be written entirely in terms of displacements.

Our contribution in this paper is to synthesize the concepts discussed over the last twenty years into a general purpose formulation for the solution of elastic and inelastic problems involving almost incompressible materials. The formulation is based on a mixed interpolation of the displacements u_i and pressure p; hence we call the formulation the u/p formulation. The major conceptual difference between our formulation and other formulations is that we explicitly replace the pressure computed from the displacement field by a separately interpolated pressure using a *general* procedure; the u/p formulation is therefore directly applicable to elastic and inelastic analysis and also may be used to analyze orthotropic and compressible materials. In incremental nonlinear analysis, we do not entirely eliminate the pressure variables from the incremental equations of motion. Rather, we solve for displacement and pressure increments during an equilibrium iteration, which are used to update the total displacements and pressures.

In the following sections of the paper we derive the general nonlinear u/p formulation from a modified potential, first the total Lagrangian formulation and then the updated Lagrangian formulation. Both of these approaches produce the same incremental equations of motion. We discuss the physical meaning of these equations, with special emphasis on a material restriction implicit in the u/p formulation, and present simplifications for materially-nonlinear-only analysis and linear analysis.

We consider the implementation of the following material descriptions: isotropic linear elasticity, anisotropic linear elasticity, von Mises elasto-plasticity, Mooney–Rivlin nonlinear elasticity and Ogden nonlinear elasticity. Then we consider the solution of the incremental finite element equations in nonlinear analysis and discuss some considerations involving contact boundary conditions. Next, a numerical example is used to show the locking behavior of several *u/p* elements. Finally, the two- and three-dimensional example problems solved show the generality and effectiveness of the solution approach.

2. THEORETICAL DEVELOPMENTS

The name of our formulation, the *u/p* formulation, reflects the use of separate interpolations for the displacements and the (hydrostatic) pressure. Other formulations based on separate interpolations of displacements and pressures have been discussed in the literature; our contribution is to derive the governing equations of motion in a general form that can be applied to inelastic as well as elastic analyses. Our formulation may also be applied to compressible analyses.

In the following derivation, we consider a general nonlinear analysis, in which material and/or geometric nonlinearities are included. The derivations employ many of the concepts and notations used by Bathe in nonlinear analysis [1]. First we use a total Lagrangian (T.L.) formulation to derive the finite element stiffness matrices and force vectors. Then we discuss an updated Lagrangian (U.L.) formulation and show that the two approaches give the same governing equations. Finally we discuss simplifications of the general formulation for the special cases of only material nonlinearities (materially-nonlinear-only analysis) and then no nonlinearities (linear analysis).

Two symbols that we use extensively in this paper are ${}^t\bar{p}$ and ${}^t\tilde{p}$: ${}^t\bar{p}$ denotes the hydrostatic pressure (positive in compression) as computed directly from the displacements and ${}^t\tilde{p}$ denotes the hydrostatic pressure as computed from the separately interpolated pressure variables.

2.1 *Total Lagrangian formulation*

In the following discussion, we make the fundamental assumption that the material description used has an incremental potential; that is, there is a number ${}^t_0\bar{W}$ such that

$$\mathrm{d}\,{}^t_0\bar{W} = {}^t_0\bar{S}_{ij}\,\mathrm{d}\,{}^t_0\varepsilon_{ij},\dagger \tag{2.1}$$

where ${}^t_0\bar{S}_{ij}$ are the components of the second Piola–Kirchhoff stress tensor and ${}^t_0\varepsilon_{ij}$ are the components of the Green–Lagrange strain tensor. Note that the left subscript 'o' denotes 'referred to the original configuration'; in particular ${}^t_0\bar{W}$ represents energy per unit original volume. Also notice that we are using the overbar to emphasize that the quantities are computed from the displacement field. This distinction will become important later and throughout this paper an overbar denotes 'computed from displacements'.

Materials with an incremental potential include elastic materials (sometimes called hyperelastic materials) and also inelastic materials, provided that the normality rule holds [26, 27]. If the material is elastic, the potential ${}^t_0\bar{W}$ physically represents the strain energy density per unit original volume. For an inelastic material, the potential may not have such an obvious physical interpretation, but for our purpose, the numerical value of the potential is not important; what is important is the manner in which ${}^t_0\bar{W}$ changes due to an incremental change in the strains.

A consequence of the material assumption (2.1) is that the tensor

$${}_0\bar{C}_{ijrs} = \frac{\partial\,{}^t_0\bar{S}_{ij}}{\partial\,{}^t_0\varepsilon_{rs}} = \frac{\partial^2\,{}^t_0\bar{W}}{\partial\,{}^t_0\varepsilon_{ij}\,\partial\,{}^t_0\varepsilon_{rs}} \tag{2.2}$$

has the following symmetry property:

$${}_0\bar{C}_{ijrs} = {}_0\bar{C}_{rsij}.$$

For this reason, the displacement-based finite element method produces symmetric element tangent stiffness matrices and so will a potential-based *u/p* formulation. The *u/p* formulation equations of motion are specified totally by the form of the potential; the element force vector and stiffness matrix are derived by chain differentiation.

We can easily establish the equations of motion in terms of the potential as follows. The principle of virtual work is

$$\int_{{}^0V} {}^t_0\bar{S}_{ij}\,\delta\,{}^t_0\varepsilon_{ij}\,{}^0\mathrm{d}V = {}^t\mathscr{R} \tag{2.3}$$

where ${}^t\mathscr{R}$ is the external virtual work at time t. Equation (2.3) can be written as

$$\int_{{}^0V} \frac{\partial\,{}^t_0\bar{W}}{\partial\,{}^t_0\varepsilon_{ij}}\,\delta\,{}^t_0\varepsilon_{ij}\,{}^0\mathrm{d}V = {}^t\mathscr{R}$$

or

$$\delta\left(\int_{{}^0V} {}^t_0\bar{W}\,{}^0\mathrm{d}V\right) = {}^t\mathscr{R}. \tag{2.4}$$

In words, the variation of the integrated 'internal stress' potential (due to variations in the displacements) must equal the variation in the 'external loading' potential. The only admissible variations

† Here and throughout this paper we use the summation convention for repeated indices.

in displacement-based finite element analysis are displacement variations. These are controlled by the nodal point displacements, which we denote as ${}^t\hat{u}_k$. In the u/p formulation, the pressure variables, which we denote as ${}^t\hat{p}_k$, are also unknown and subject to variation. As will be seen, the pressure variations are used to generate constraint equations.

The key step in the construction of the u/p formulation is to properly modify the potential to include the pressure variables. We modify the potential ${}^t_0\bar{W}$ by adding to it an unknown potential ${}^t_0Q$, which is a function of both the displacements and the separately interpolated pressure. The governing equation of motion is then

$$\delta\left(\int_{{}^0V} ({}^t_0\bar{W} + {}^t_0Q)\,{}^0\mathrm{d}V\right) = {}^t\mathscr{R}, \tag{2.5}$$

where we now consider variations in the pressure variables as well as in the displacement variables.

The modified potential ${}^t_0\bar{W} + {}^t_0Q$ must fulfill three basic physical requirements:

(1) The pressure computed from the modified potential must equal the separately interpolated pressure. This must hold for the possibly inaccurate pressure computed from displacements to be removed from the stresses.
(2) Varying the modified potential with respect to a pressure variable must generate a constraint equation relating the separately interpolated pressure to the pressure computed from the displacements. Otherwise the separately interpolated pressure will not have the correct physical meaning.
(3) If the pressure computed from the displacements happens to equal the separately interpolated pressure, the modified potential must equal the unmodified potential. This ensures that the u/p formulation solution includes, as a special case, the displacement-based formulation.

Before deriving ${}^t_0Q$, let us define precisely what we mean by 'pressure computed from a potential'. First, recall that the relationship between the Cauchy stress tensor and the 2nd Piola–Kirchhoff stress tensor is

$${}^t\bar{\tau}_{ij} = \frac{1}{\det {}^t_0\mathbf{X}}\, {}^t_0x_{i,m}\, {}^t_0x_{j,n}\, {}^t_0\bar{S}_{mn}, \tag{2.6}$$

where the ${}^t_0x_{i,j}$ are the components of the deformation gradient tensor ${}^t_0\mathbf{X}$ (in Cartesian coordinates, ${}^t_0x_{i,j} = {}^t_0X_{ij} = \partial {}^tx_i/\partial {}^0x_j$). Hence the hydrostatic pressure contained in the 2nd Piola–Kirchhoff stress tensor is just

$${}^t\bar{p} = -\tfrac{1}{3}\,{}^t\bar{\tau}_{ii} = -\frac{1}{3\det {}^t_0\mathbf{X}}\, {}^t_0C_{mn}\, {}^t_0\bar{S}_{mn}, \tag{2.7}$$

where ${}^t_0C_{mn} = {}^t_0x_{i,m}\, {}^t_0x_{i,n}$ is the right Cauchy–Green deformation tensor. In terms of the potential, we have

$${}^t\bar{p} = -\frac{1}{3\det {}^t_0\mathbf{X}}\, {}^t_0C_{mn}\frac{\partial\, {}^t_0\bar{W}}{\partial\, {}^t_0\varepsilon_{mn}}. \tag{2.8}$$

Because we will be using this operation often, we define the operator ${}_0P$ as follows:

$${}^t\bar{p} = {}_0P({}^t_0\bar{W}), \tag{2.9}$$

where

$${}_0P(\cdot) = -\frac{1}{3\det {}^t_0\mathbf{X}}\, {}^t_0C_{mn}\frac{\partial(\cdot)}{\partial\, {}^t_0\varepsilon_{mn}}. \tag{2.10}$$

Notice that ${}_0P$ essentially represents a differentiation with respect to the strains.†

With this notation, requirement (1) can be written as

$${}_0P({}^t_0\bar{W} + {}^t_0Q) = {}^t\bar{p}, \tag{2.11}$$

or, equivalently,

$${}^t_0\bar{W} + {}^t_0Q = {}_0P^{-1}({}^t\bar{p}). \tag{2.12}$$

Now we apply requirement (2). Mathematically, requirement (2) states that

$$\frac{\partial}{\partial \hat{p}_k}\left(\int_{{}^0V} ({}^t_0\bar{W} + {}^t_0Q)\,{}^0\mathrm{d}V\right)\delta\hat{p}_k = 0 \tag{2.13}$$

represents a constraint equation. Equation (2.13) may be rewritten as

$$\int_{{}^0V} \frac{\partial}{\partial \bar{p}}({}^t_0\bar{W} + {}^t_0Q)\,\delta\bar{p}\,{}^0\mathrm{d}V = 0. \tag{2.14}$$

By eqn (2.12), we have

$$\frac{\partial}{\partial \bar{p}}({}^t_0\bar{W} + {}^t_0Q) = \frac{\partial}{\partial \bar{p}}({}_0P^{-1}({}^t\bar{p})), \tag{2.15}$$

or, since ${}^t_0\bar{W}$ is a function only of the displacements and ${}_0P$ differentiates with respect to strains only,

$$\frac{\partial\, {}^t_0Q}{\partial \bar{p}} = {}_0P^{-1}(1) \tag{2.16}$$

† In mathematical terminology, ${}_0P$ is a linear operator; that is, if c is a constant

$${}_0P(c\,{}^t_0\bar{W}) = c\,{}_0P({}^t_0\bar{W}),$$

and for two potentials ${}^t_0\bar{W}_1$ and ${}^t_0\bar{W}_2$

$${}_0P({}^t_0\bar{W}_1 + {}^t_0\bar{W}_2) = {}_0P({}^t_0\bar{W}_1) + {}_0P({}^t_0\bar{W}_2).$$

Because ${}_0P$ is a linear operator, we may apply the usual rules of differentiation when manipulating ${}_0P$.

and therefore the constraint eqn (2.14) must have the form

$$\int_{{}_0V} {}_0P^{-1}(1)\delta\bar{p}\,{}^0\mathrm{d}V = 0. \tag{2.17}$$

For this constraint equation to be physically realistic, it must relate ${}^t\tilde{p}$ to ${}^t\bar{p}$. The simplest constraint equation that is reasonable is

$$\int_{{}_0V} r({}^t\bar{p} - {}^t\tilde{p})\delta\tilde{p}\,{}^0\mathrm{d}V = 0, \tag{2.18}$$

where r is some function of the displacements. Comparing eqns (2.17) and (2.18) gives

$${}_0P^{-1}(1) = r({}^t\bar{p} - {}^t\tilde{p}) \tag{2.19}$$

or

$$1 = {}_0P(r)({}^t\bar{p} - {}^t\tilde{p}) + r\,{}_0P({}^t\bar{p} - {}^t\tilde{p}). \tag{2.20}$$

Equation (2.20) is satisfied only if

$$r = 1/{}_0P({}^t\bar{p}) \tag{2.21}$$

and simultaneously

$${}_0P(r) = 0. \tag{2.22}$$

Equations (2.21) and (2.22) may be combined to obtain

$${}_0P(1/{}_0P({}^t\bar{p})) = -\frac{1}{({}_0P({}^t\bar{p}))^2}\,{}_0P({}_0P({}^t\bar{p})) = 0$$

or

$${}_0P^2({}^t\bar{p}) = 0, \tag{2.23}$$

where ${}_0P^2(\cdot) = {}_0P({}_0P(\cdot))$. Equation (2.23) is a restriction on the material description used in the analysis; that is, eqn (2.23) must be satisfied for any material modeled with the u/p formulation. This restriction is discussed further in Sec. 2.5, where we note that a large number of material descriptions used in engineering analysis satisfy this material restriction.

Substituting eqn (2.21) into eqn (2.18) gives us the constraint equation

$$\int_{{}_0V} \frac{1}{P({}^t\bar{p})}({}^t\bar{p} - {}^t\tilde{p})\delta\tilde{p}\,{}^0\mathrm{d}V = 0, \tag{2.24}$$

and we can determine ${}^t_0Q$ by integration from eqn (2.16):

$${}^t_0Q = \int_{{}^t\tilde{p}} \frac{1}{{}_0P({}^t\bar{p})}({}^t\bar{p} - {}^t\tilde{p})\mathrm{d}{}^t\tilde{p}$$

$$= -\frac{1}{2\,{}_0P({}^t\bar{p})}({}^t\bar{p} - {}^t\tilde{p})^2, \tag{2.25}$$

in which we have determined the constant of integration (in this case, a function of the displacements) so that ${}^t_0Q$ is zero whenever ${}^t\tilde{p}$ equals ${}^t\bar{p}$. This selection satisfies requirement (3). The modified potential is therefore

$${}^t_0\bar{W} + {}^t_0Q = {}^t_0\bar{W} - \frac{1}{2\,{}_0P({}^t\bar{p})}({}^t\bar{p} - {}^t\tilde{p})^2. \tag{2.26}$$

2.1.1 *Derivation of finite element matrices.* In matrix form, the governing incremental equations of motion for a finite element are [1]:

$$\begin{bmatrix} {}^t\mathbf{KUU} & {}^t\mathbf{KUP} \\ {}^t\mathbf{KPU} & {}^t\mathbf{KPP} \end{bmatrix} \begin{bmatrix} \hat{\mathbf{u}} \\ \hat{\mathbf{p}} \end{bmatrix} = \begin{bmatrix} {}^{t+\Delta t}\mathbf{R} \\ \mathbf{0} \end{bmatrix} - \begin{bmatrix} {}^t\mathbf{FU} \\ {}^t\mathbf{FP} \end{bmatrix}, \tag{2.27}$$

where ${}^{t+\Delta t}\mathbf{R}$ are the nodal point forces corresponding to the external loading at time $t + \Delta t$, $\hat{\mathbf{u}}$ and $\hat{\mathbf{p}}$ are vectors containing the increments in ${}^t\hat{u}_k$ and ${}^t\hat{p}_k$, ${}^t\mathbf{FU}$ and ${}^t\mathbf{FP}$ contain the entries

$${}^tFU_i = \frac{\partial}{\partial\hat{u}_i}\left[\int_{{}_0V}\left({}^t_0\bar{W} - \frac{1}{2\,{}_0P({}^t\bar{p})}({}^t\bar{p} - {}^t\tilde{p})^2\right){}^0\mathrm{d}V\right] \tag{2.28}$$

$${}^tFP_i = \frac{\partial}{\partial\hat{p}_i}\left[\int_{{}_0V}\left({}^t_0\bar{W} - \frac{1}{2\,{}_0P({}^t\bar{p})}({}^t\bar{p} - {}^t\tilde{p})^2\right){}^0\mathrm{d}V\right], \tag{2.29}$$

and ${}^t\mathbf{KUU}$, ${}^t\mathbf{KUP}$, ${}^t\mathbf{KPU}$, ${}^t\mathbf{KPP}$ contain the entries

$${}^tKUU_{ij} = \frac{\partial\,{}^tFU_i}{\partial\hat{u}_j} \tag{2.30}$$

$${}^tKUP_{ij} = \frac{\partial\,{}^tFU_i}{\partial\hat{p}_j} = \frac{\partial\,{}^tFP_j}{\partial\hat{u}_i} = {}^tKPU_{ji} \tag{2.31}$$

$${}^tKPP_{ij} = \frac{\partial\,{}^tFP_i}{\partial\hat{p}_j}. \tag{2.32}$$

Notice that the force vector is partitioned into two parts, one part for displacement variations and the other part for pressure variations. Similarly the stiffness matrix is partitioned into four parts.

Using chain differentiation, we find that

$${}^tFU_i = \int_{{}_0V} {}^t_0S_{kl}\frac{\partial\,{}^t_0\varepsilon_{kl}}{\partial\hat{u}_i}\,{}^0\mathrm{d}V \tag{2.33}$$

$${}^tFP_i = \int_{{}_0V} -{}_0CPP\,({}^t\bar{p} - {}^t\tilde{p})\frac{\partial\,{}^t\tilde{p}}{\partial\hat{p}_i}\,{}^0\mathrm{d}V \tag{2.34}$$

and

$${}^tKUU_{ij} = \int_{{}_0V} {}_0CUU_{klrs}\frac{\partial\,{}^t_0\varepsilon_{kl}}{\partial\hat{u}_i}\frac{\partial\,{}^t_0\varepsilon_{rs}}{\partial\hat{u}_j}\,{}^0\mathrm{d}V + \int_{{}_0V} {}^t_0S_{kl}\frac{\partial^2\,{}^t_0\varepsilon_{kl}}{\partial\hat{u}_i\partial\hat{u}_j}\,{}^0\mathrm{d}V \tag{2.35}$$

$$ {}^{t}KUP_{ij} = \int_{{}_0V} {}_0CUP_{kl} \frac{\partial\, {}^{t}_0\varepsilon_{kl}}{\partial \hat{u}_i} \frac{\partial\, {}^{t}\tilde{p}}{\partial \hat{p}_j}\, {}_0\mathrm{d}V \tag{2.36} $$

$$ {}^{t}KPP_{ij} = \int_{{}_0V} {}_0CPP \frac{\partial\, {}^{t}\tilde{p}}{\partial \hat{p}_i} \frac{\partial\, {}^{t}\tilde{p}}{\partial \hat{p}_j}\, {}_0\mathrm{d}V, \tag{2.37} $$

where we use the definitions

$$ {}_0CPP = -\frac{1}{{}_0P({}^{t}\tilde{p})} \tag{2.38} $$

$$ {}_0CUP_{kl} = -{}_0CPP \frac{\partial\, {}^{t}\tilde{p}}{\partial\, {}^{t}_0\varepsilon_{kl}} - \frac{1}{{}_0CPP^2}({}^{t}\tilde{p} - {}^{t}\tilde{p}) \times \frac{\partial({}_0P({}^{t}\tilde{p}))}{\partial\, {}^{t}_0\varepsilon_{kl}} \tag{2.39} $$

$$ \begin{aligned} {}_0CUU_{klrs} = {}_0\bar{C}_{klrs} &+ {}_0CPP \frac{\partial\, {}^{t}\tilde{p}}{\partial\, {}^{t}_0\varepsilon_{kl}} \frac{\partial\, {}^{t}\tilde{p}}{\partial\, {}^{t}_0\varepsilon_{rs}} \\ &+ {}_0CPP({}^{t}\tilde{p} - {}^{t}\tilde{p}) \frac{\partial^2\, {}^{t}\tilde{p}}{\partial\, {}^{t}_0\varepsilon_{kl}\, \partial\, {}^{t}_0\varepsilon_{rs}} \\ &+ {}_0CPP^2({}^{t}\tilde{p} - {}^{t}\tilde{p}) \\ &\times \left(\frac{\partial({}_0P({}^{t}\tilde{p}))}{\partial\, {}^{t}_0\varepsilon_{kl}} \frac{\partial\, {}^{t}\tilde{p}}{\partial\, {}^{t}_0\varepsilon_{rs}} + \frac{\partial\, {}^{t}\tilde{p}}{\partial\, {}^{t}_0\varepsilon_{kl}} \frac{\partial({}_0P({}^{t}\tilde{p}))}{\partial\, {}^{t}_0\varepsilon_{rs}} \right) \\ &+ {}_0CPP^3({}^{t}\tilde{p} - {}^{t}\tilde{p})^2 \frac{\partial({}_0P({}^{t}\tilde{p}))}{\partial\, {}^{t}_0\varepsilon_{kl}} \frac{\partial({}_0P({}^{t}\tilde{p}))}{\partial\, {}^{t}_0\varepsilon_{rs}} \\ &+ \tfrac{1}{2}\, {}_0CPP^2({}^{t}\tilde{p} - {}^{t}\tilde{p})^2 \frac{\partial^2({}_0P({}^{t}\tilde{p}))}{\partial\, {}^{t}_0\varepsilon_{kl}\, \partial\, {}^{t}_0\varepsilon_{rs}} \end{aligned} \tag{2.40} $$

$$ \begin{aligned} {}^{t}_0S_{kl} = {}^{t}_0\bar{S}_{kl} &+ {}_0CPP({}^{t}\tilde{p} - {}^{t}\tilde{p}) \frac{\partial\, {}^{t}\tilde{p}}{\partial\, {}^{t}_0\varepsilon_{kl}} \\ &+ \tfrac{1}{2}\, {}_0CPP^2({}^{t}\tilde{p} - {}^{t}\tilde{p})^2 \frac{\partial({}_0P({}^{t}\tilde{p}))}{\partial\, {}^{t}_0\varepsilon_{kl}}. \end{aligned} \tag{2.41} $$

Note that, when ${}_0P({}^{t}\tilde{p})$ is constant (as is the case for common material descriptions), several of the terms in the above equations are zero.

Equilibrium is satisfied when, for all degrees of freedom i,

$$ 0 = {}^{t}R_i - \int_{{}_0V} {}^{t}_0S_{kl} \frac{\partial\, {}^{t}_0\varepsilon_{kl}}{\partial \hat{u}_i}\, {}_0\mathrm{d}V \tag{2.42} $$

and

$$ 0 = \int_{{}_0V} {}_0CPP({}^{t}\tilde{p} - {}^{t}\tilde{p}) \frac{\partial\, {}^{t}\tilde{p}}{\partial \hat{p}_i}\, {}_0\mathrm{d}V. \tag{2.43} $$

2.1.2 *Discretization.* To evaluate eqns (2.33)–(2.37), we need to express the change in the Green–Lagrange strain tensor ${}^{t}_0\varepsilon_{kl}$ and the interpolated pressure ${}^{t}\tilde{p}$ in terms of the incremental solution variables $\hat{u}_i$ and $\hat{p}_i$. Here we assume that continuum elements are used and write, for a material point within an element,

$$ {}^{t}u_i = h_L\, {}^{t}u_i^L \tag{2.44} $$

$$ {}^{t}\tilde{p} = g_i\, {}^{t}\hat{p}_i, \tag{2.45} $$

in which the h_L are the interpolation functions for the displacements and the g_i are the interpolation functions for the pressure. Also, ${}^{t}u_i^L$ is the displacement at node L in the ith direction; this variable can be identified with the nodal point displacement degree of freedom ${}^{t}\hat{u}_i$ discussed earlier. For the pressure, we simply obtain

$$ \frac{\partial\, {}^{t}\tilde{p}}{\partial \hat{p}_i} = g_i. \tag{2.46} $$

Since

$$ {}^{t}_0\varepsilon_{kl} = \tfrac{1}{2}({}^{t}_0x_{b,k}\, {}^{t}_0x_{b,l} - \delta_{kl}), \tag{2.47} $$

where δ_{kl} is the Kronecker delta, we obtain for the derivatives with respect to nodal point displacements

$$ \frac{\partial\, {}^{t}_0\varepsilon_{kl}}{\partial u_i^L} = \tfrac{1}{2}({}^{t}_0x_{i,k}\, {}_0h_{L,l} + {}^{t}_0x_{i,l}\, {}_0h_{L,k}) \tag{2.48} $$

$$ \frac{\partial^2\, {}^{t}_0\varepsilon_{kl}}{\partial u_i^L\, \partial u_j^M} = \tfrac{1}{2}({}_0h_{L,k}\, {}_0h_{M,l} + {}_0h_{L,l}\, {}_0h_{M,k})\delta_{ij}. \tag{2.49} $$

We note that the relations in eqns (2.48) and (2.49) are equivalent to the quantities ${}_0e_{ij}$, ${}_0\eta_{ij}$ used in [1].

2.2 *Updated Lagrangian formulation*

In the preceding derivation, we worked with the original configuration as the reference configuration. This generated the total Lagrangian form of the finite element equations of motion. However, we can also derive the updated Lagrangian form of the finite element equations of motion by using the last computed configuration as the reference configuration. Symbolically, this is done by changing all left subscripts from 'o' to 'T'. Configuration T is identical to the configuration at time t; we introduce a different symbol because configuration T is assumed to be fixed and therefore constant when differentiations are performed.

The primary advantage of the updated Lagrangian form of the equations of motion is that the equations can be written in terms of the Cauchy stresses and infinitesimal strains rather than in terms of the 2nd Piola–Kirchhoff stresses and Green–Lagrange strains. This is because, at time $t = T$, ${}^{t}_TS_{ij} = {}^{t}\tau_{ij}$ and $\mathrm{d}\, {}^{t}_T\varepsilon_{ij} = \mathrm{d}\, {}_te_{ij}$ where

$$ \mathrm{d}\, {}_te_{ij} = \frac{1}{2}\left[\frac{\partial\, \mathrm{d}u_i}{\partial\, {}^{t}x_j} + \frac{\partial\, \mathrm{d}u_j}{\partial\, {}^{t}x_i} \right]. \tag{2.50} $$

Now we follow the steps used in the derivation of the total Lagrangian formulation to produce the updated Lagrangian formulation. The material incremental potential is, for time $t = T$,

$$\mathrm{d}\,{}_T^t\bar{W} = {}^t\bar{\tau}_{ij}\,\mathrm{d}\,{}_te_{ij}, \tag{2.51}$$

where ${}_T^t\bar{W}$ represents energy per unit of volume at time T. The relationship between ${}_T^t\bar{W}$ and ${}_0^t\bar{W}$ is given by

$${}_T^t\bar{W}\,{}^T\mathrm{d}V = {}_0^t\bar{W}\,{}^0\mathrm{d}V. \tag{2.52}$$

Using

$${}^T\mathrm{d}V = \det {}_0^T\mathbf{X}\,{}^0\mathrm{d}V, \tag{2.53}$$

eqn (2.52) can be solved for ${}_T^t\bar{W}$ to give

$${}_T^t\bar{W} = \frac{{}_0^t\bar{W}}{\det {}_0^T\mathbf{X}}. \tag{2.54}$$

The governing equation of motion for the displacement-based formulation is

$$\delta\left(\int_{{}^TV} {}_T^t\bar{W}\,{}^T\mathrm{d}V\right) = {}^t\mathscr{R}, \tag{2.55}$$

and for the u/p formulation is

$$\delta\left(\int_{{}^TV} ({}_T^t\bar{W} + {}_T^tQ)\,{}^T\mathrm{d}V\right) = {}^t\mathscr{R}, \tag{2.56}$$

where ${}_T^tQ$ is derived below. In deriving the updated Lagrangian formulation, the operator ${}_TP$ is defined to give

$${}_TP({}_T^t\bar{W}) = {}^t\bar{p} \tag{2.57}$$

and this may also be written as

$${}_TP(\cdot) = -\frac{1}{3\det {}_T^t\mathbf{X}}\,{}_T^tC_{mn}\frac{\partial(\cdot)}{\partial\,{}_T^te_{mn}} \tag{2.58}$$

or, when $t = T$,

$${}_TP(\cdot) = -\frac{1}{3}\sum_{i=1}^{3}\frac{\partial(\cdot)}{\partial\,{}_te_{ii}}.$$

Requirement (1) gives

$${}_T^t\bar{W} + {}_T^tQ = {}_TP^{-1}({}^t\tilde{p}) \tag{2.59}$$

or

$$\frac{\partial\,{}_T^tQ}{\partial\tilde{p}} = {}_TP^{-1}(1) \tag{2.60}$$

and the constraint equation becomes

$$\int_{{}^TV} {}_TP^{-1}(1)\delta\tilde{p}\,{}^T\mathrm{d}V = 0. \tag{2.61}$$

Choosing as a constraint equation (requirement (2))

$$\int_{{}^TV} r({}^t\bar{p} - {}^t\tilde{p})\delta\tilde{p}\,{}^T\mathrm{d}V = 0, \tag{2.62}$$

where r may again be a function of the displacements, gives

$${}_TP^{-1}(1) = r({}^t\bar{p} - {}^t\tilde{p}) \tag{2.63}$$

and eqn (2.63) implies

$$r = 1/{}_TP({}^t\tilde{p}) \tag{2.64}$$

and

$${}_TP(r) = 0. \tag{2.65}$$

Equations (2.64) and (2.65) may be combined to give the material restriction

$${}_TP^2({}^t\tilde{p}) = 0. \tag{2.66}$$

The constraint equation becomes

$$\int_{{}^TV} \frac{1}{{}_TP({}^t\tilde{p})}({}^t\bar{p} - {}^t\tilde{p})\delta\tilde{p}\,{}^T\mathrm{d}V = 0; \tag{2.67}$$

the unknown potential ${}_T^tQ$ becomes

$${}_T^tQ = -\frac{1}{2\,{}_TP({}^t\tilde{p})}({}^t\bar{p} - {}^t\tilde{p})^2; \tag{2.68}$$

and the equation of motion becomes

$$\delta\left[\int_{{}^TV}\left({}_T^t\bar{W} - \frac{1}{2\,{}_TP({}^t\tilde{p})}({}^t\bar{p} - {}^t\tilde{p})^2\right){}^T\mathrm{d}V\right] = {}^t\mathscr{R}. \tag{2.69}$$

Differentiating eqn (2.69) and choosing time $T = t$ gives

$${}^tFU_i = \int_{{}^tV} {}^t\tau_{kl}\frac{\partial\,{}_te_{kl}}{\partial\hat{u}_i}\,{}^t\mathrm{d}V \tag{2.70}$$

$${}^tFP_i = \int_{{}^tV} -{}_TCPP({}^t\bar{p} - {}^t\tilde{p})\frac{\partial\,{}^t\bar{p}}{\partial\hat{p}_i}\,{}^t\mathrm{d}V \tag{2.71}$$

and

$${}^tKUU_{ij} = \int_{{}^tV} {}_TCUU_{klrs}\frac{\partial\,{}_te_{kl}}{\partial\hat{u}_i}\frac{\partial\,{}_te_{rs}}{\partial\hat{u}_j}\,{}^t\mathrm{d}V + \int_{{}^tV} {}^t\tau_{kl}\frac{\partial^2\,{}_te_{kl}}{\partial\hat{u}_i\,\partial\hat{u}_j}\,{}^t\mathrm{d}V \tag{2.72}$$

$$ {}^{t}KUP_{ij} = \int_{{}^{t}V} {}_{T}CUP_{kl} \frac{\partial\, {}_{t}e_{kl}}{\partial \hat{u}_i} \frac{\partial\, {}^{t}\bar{p}}{\partial \hat{p}_j}\, {}^{t}dV \tag{2.73} $$

$$ {}^{t}KPP_{ij} = \int_{{}^{t}V} {}_{T}CPP \frac{\partial\, {}^{t}\bar{p}}{\partial \hat{p}_i} \frac{\partial\, {}^{t}\bar{p}}{\partial \hat{p}_j}\, {}^{t}dV, \tag{2.74} $$

where

$$ {}_{T}CPP = -1/{}_{T}P({}^{t}\bar{p}) \tag{2.75} $$

$$ {}_{T}CUP_{kl} = -{}_{T}CPP \frac{\partial\, {}^{t}\bar{p}}{\partial\, {}_{t}e_{kl}} - \frac{1}{{}_{T}CPP^2} \times ({}^{t}\bar{p} - {}^{t}\tilde{p}) \frac{\partial({}_{T}P({}^{t}\bar{p}))}{\partial\, {}_{t}e_{kl}} \tag{2.76} $$

$$ \begin{aligned} {}_{T}CUU_{klrs} = {}& {}_{T}\bar{C}_{klrs} + {}_{T}CPP \frac{\partial\, {}^{t}\bar{p}}{\partial\, {}_{t}e_{kl}} \frac{\partial\, {}^{t}\bar{p}}{\partial\, {}_{t}e_{rs}} \\ & + {}_{T}CPP({}^{t}\bar{p} - {}^{t}\tilde{p}) \frac{\partial^2\, {}^{t}\bar{p}}{\partial\, {}_{t}e_{kl}\, \partial\, {}_{t}e_{rs}} \\ & + {}_{T}CPP^2({}^{t}\bar{p} - {}^{t}\tilde{p}) \left[\frac{\partial({}_{T}P({}^{t}\bar{p}))}{\partial\, {}_{t}e_{kl}} \frac{\partial\, {}^{t}\bar{p}}{\partial\, {}_{t}e_{rs}} \right. \\ & \left. + \frac{\partial\, {}^{t}\bar{p}}{\partial\, {}_{t}e_{kl}} \frac{\partial({}_{T}P({}^{t}\bar{p}))}{\partial\, {}_{t}e_{rs}} \right] \\ & + {}_{T}CPP^3({}^{t}\bar{p} - {}^{t}\tilde{p})^2 \frac{\partial({}_{T}P({}^{t}\bar{p}))}{\partial\, {}_{t}e_{kl}} \frac{\partial({}_{T}P({}^{t}\bar{p}))}{\partial\, {}_{t}e_{rs}} \\ & + \tfrac{1}{2}\, {}_{T}CPP^2({}^{t}\bar{p} - {}^{t}\tilde{p})^2 \frac{\partial^2({}_{T}P({}^{t}p))}{\partial\, {}_{t}e_{kl}\, \partial\, {}_{t}e_{rs}} \end{aligned} \tag{2.77} $$

$$ \begin{aligned} {}^{t}\tau_{kl} = {}& {}^{t}\bar{\tau}_{kl} + {}_{T}CPP({}^{t}\bar{p} - {}^{t}\tilde{p}) \frac{\partial\, {}^{t}\bar{p}}{\partial\, {}_{t}e_{kl}} \\ & + \tfrac{1}{2}\, {}_{T}CPP^2({}^{t}\bar{p} - {}^{t}\tilde{p})^2 \frac{\partial({}_{T}P({}^{t}\bar{p}))}{\partial\, {}_{t}e_{kl}}. \end{aligned} \tag{2.78} $$

2.2.1 *Discretization.* To discretize the updated Lagrangian form of the equations of motion, we need to express the change in the infinitesimal strain tensor ${}_{t}e_{kl}$ and the interpolated pressure ${}^{t}\bar{p}$ in terms of the incremental solution variables $\hat{u}_i$ and $\hat{p}_i$. The pressure variable is treated in exactly the same manner as in the total Lagrangian formulation. For the strain tensor, we use the relationship

$$ {}_{T}^{t}\varepsilon_{kl} = \tfrac{1}{2}({}_{T}^{t}x_{b,k}\, {}_{T}^{t}x_{b,l} - \delta_{kl}) \tag{2.79} $$

and we therefore obtain

$$ \frac{\partial\, {}_{T}^{t}\varepsilon_{kl}}{\partial u_i^L} = \tfrac{1}{2}({}_{T}^{t}x_{i,k}\, {}_{T}h_{L,l} + {}_{T}^{t}x_{i,l}\, {}_{T}h_{L,k}) \tag{2.80} $$

and

$$ \frac{\partial^2\, {}_{T}^{t}\varepsilon_{kl}}{\partial u_i^L\, \partial u_j^M} = \tfrac{1}{2}({}_{T}h_{L,k}\, {}_{T}h_{M,l} + {}_{T}h_{L,l}\, {}_{T}h_{M,k})\delta_{ij}. \tag{2.81} $$

Since at time $t = T$, ${}_{T}^{t}x_{i,j} = \delta_{ij}$, we see that

$$ \frac{\partial\, {}_{t}e_{kl}}{\partial u_i^L} = \tfrac{1}{2}(\delta_{ik}\, {}_{T}h_{L,l} + \delta_{il}\, {}_{T}h_{L,k}) \tag{2.82} $$

and

$$ \frac{\partial^2\, {}_{t}e_{kl}}{\partial u_i^L\, \partial u_j^M} = \tfrac{1}{2}({}_{T}h_{L,k}\, {}_{T}h_{M,l} + {}_{T}h_{L,l}\, {}_{T}h_{M,k})\delta_{ij}. \tag{2.83} $$

The relations in eqns (2.82) and (2.83) are equivalent to the quantities ${}_{t}e_{ij}$ and ${}_{t}\eta_{ij}$ used in [1].

2.3 *Comparison of the T.L. and U.L. formulations*

The u/p formulations using the total Lagrangian approach and the updated Lagrangian approach give exactly the same finite element equations. The reason for this is that we have made the same assumptions and followed the same procedures in both derivations.

The displacement-based finite element equations of motion are identical because of eqn (2.52). The equations of the u/p formulations are also identical because, in addition,

$$ {}_{o}^{t}Q\, {}^{o}dV = {}_{T}^{t}Q\, {}^{T}dV. \tag{2.84} $$

To prove this equality, we show that

$$ \frac{1}{{}_{o}P({}^{t}\bar{p})}\, {}^{o}dV = \frac{1}{{}_{T}P({}^{t}\bar{p})}\, {}^{T}dV. \tag{2.85} $$

This is true because

$$ \begin{aligned} {}_{o}P({}_{o}^{t}\bar{W}) = {}^{t}\bar{p} = {}_{T}P({}_{T}^{t}\bar{W}) &= {}_{T}P({}_{o}^{t}\bar{W}/\det {}_{o}^{T}\mathbf{X}) \\ &= \frac{1}{\det {}_{o}^{T}\mathbf{X}}\, {}_{T}P({}_{o}^{t}\bar{W}), \end{aligned} \tag{2.86} $$

so that (since ${}_{o}^{t}\bar{W}$ is arbitrarily chosen in eqn (2.86))

$$ \frac{1}{{}_{o}P({}^{t}\bar{p})}\, {}^{o}dV = \frac{\det {}_{o}^{T}\mathbf{X}}{{}_{T}P({}^{t}\bar{p})}\, {}^{o}dV = \frac{1}{{}_{T}P({}^{t}\bar{p})}\, {}^{T}dV. $$

From eqn (2.85) we also note that the constraint equation, when written in the updated Lagrangian form, is identical to the constraint equation when written in the total Lagrangian form.

The other point of interest in the comparison of the two formulations lies in the nature of the material restriction. In the total Lagrangian formulation, we require that ${}_{o}P^2({}^{t}\bar{p}) = 0$ and in the updated Lagrangian formulation, we require that ${}_{T}P^2({}^{t}\bar{p}) = 0$. These conditions are indeed equivalent since

$$ \begin{aligned} {}_{o}P^2({}^{t}\bar{p}) = {}_{o}P({}_{o}P({}^{t}\bar{p})) &= {}_{o}P\left(\frac{1}{\det {}_{o}^{T}\mathbf{X}}\, {}_{T}P({}^{t}\bar{p})\right) \\ &= \left[\frac{1}{\det {}_{o}^{T}\mathbf{X}}\right]^2 {}_{T}P^2({}^{t}\bar{p}). \end{aligned} \tag{2.87} $$

Here, as before, T, and therefore $\det {}_0^T\mathbf{X}$, are assumed to be fixed during the differentiation process.

Because the potentials generated by both approaches agree, the force vectors and stiffness matrices generated by the differentiations also agree. The choice of which set of expressions to use is determined entirely by numerical considerations. For example, if the stresses are most naturally derived in terms of 2nd Piola–Kirchhoff stresses, then the total Lagrangian expressions are usually preferable.

2.4 *Reduction to small strain, small displacement conditions*

The preceding formulations make no assumptions regarding the magnitude of the displacements or strains (provided, of course, that an appropriate material description is used). However, if the displacements and strains are always small, it is more effective to use a materially–nonlinear-only (M.N.O.) formulation. The corresponding equations are obtained from the total Lagrangian form of the general equations by replacing ${}_0^tS_{kl}$ by ${}^t\tau_{kl}$, ${}_0^te_{kl}$ by ${}^te_{kl}$ (where ${}^te_{kl}$ is the infinitesimal strain tensor) and $\det {}_0^t\mathbf{X}$ by 1.0. Also it is assumed that $|{}^t\bar{\tau}_{kl}| \ll |\bar{C}_{klrs}|$, where

$$\bar{C}_{klrs} = \frac{\partial {}^t\bar{\tau}_{kl}}{\partial {}^te_{rs}}. \tag{2.88}$$

With the above simplications,

$${}^tFU_i = \int_V {}^t\tau_{kl} \frac{\partial {}^te_{kl}}{\partial {}^t\hat{u}_i} \, dV \tag{2.89}$$

$${}^tFP_i = \int_V - CPP({}^t\bar{p} - {}^t\bar{p}) \frac{\partial {}^t\bar{p}}{\partial {}^t\hat{p}_i} \, dV \tag{2.90}$$

and

$${}^tKUU_{ij} = \int_V CUU_{klrs} \frac{\partial {}^te_{kl}}{\partial {}^t\hat{u}_i} \frac{\partial {}^te_{rs}}{\partial {}^t\hat{u}_j} \, dV \tag{2.91}$$

$${}^tKUP_{ij} = \int_V CUP_{kl} \frac{\partial {}^te_{kl}}{\partial {}^t\hat{u}_i} \frac{\partial {}^t\bar{p}}{\partial {}^t\hat{p}_j} \, dV \tag{2.92}$$

$${}^tKPP_{ij} = \int_V CPP \frac{\partial {}^t\bar{p}}{\partial {}^t\hat{p}_i} \frac{\partial {}^t\bar{p}}{\partial {}^t\hat{p}_j} \, dV, \tag{2.93}$$

where now

$$CPP = -\frac{1}{P({}^t\bar{p})} \tag{2.94}$$

$$CUP_{kl} = -CPP \frac{\partial {}^t\bar{p}}{\partial {}^te_{kl}} - \frac{1}{CPP^2}({}^t\bar{p} - {}^t\bar{p}) \frac{\partial (P({}^t\bar{p}))}{\partial {}^te_{kl}} \tag{2.95}$$

$$\begin{aligned} CUU_{klrs} = \bar{C}_{klrs} &+ CPP \frac{\partial {}^t\bar{p}}{\partial {}^te_{kl}} \frac{\partial {}^t\bar{p}}{\partial {}^te_{rs}} \\ &+ CPP({}^t\bar{p} - {}^t\bar{p}) \frac{\partial^2 {}^t\bar{p}}{\partial {}^te_{kl} \, \partial {}^te_{rs}} \\ &+ CPP^2({}^t\bar{p} - {}^t\bar{p}) \\ &\times \left[\frac{\partial (P({}^t\bar{p}))}{\partial {}^te_{kl}} \frac{\partial {}^t\bar{p}}{\partial {}^te_{rs}} + \frac{\partial {}^t\bar{p}}{\partial {}^te_{kl}} \frac{\partial (P({}^t\bar{p}))}{\partial {}^te_{rs}} \right] \\ &+ CPP^3({}^t\bar{p} - {}^t\bar{p})^2 \frac{\partial (P({}^t\bar{p}))}{\partial {}^te_{kl}} \frac{\partial (P({}^t\bar{p}))}{\partial {}^te_{rs}} \\ &+ \tfrac{1}{2} CPP^2({}^t\bar{p} - {}^t\bar{p})^2 \frac{\partial^2 (P({}^t\bar{p}))}{\partial {}^te_{kl} \, \partial {}^te_{rs}} \end{aligned} \tag{2.96}$$

$$\begin{aligned} {}^t\tau_{kl} = {}^t\bar{\tau}_{kl} &+ CPP({}^t\bar{p} - {}^t\bar{p}) \frac{\partial {}^t\bar{p}}{\partial {}^te_{kl}} \\ &+ \tfrac{1}{2} CPP^2({}^t\bar{p} - {}^t\bar{p})^2 \frac{\partial (P({}^t\bar{p}))}{\partial {}^te_{kl}}, \end{aligned} \tag{2.97}$$

in which the pressure operator is

$$P(\cdot) = -\frac{1}{3} \sum_{i=1}^{3} \frac{\partial (\cdot)}{\partial {}^te_{ii}}. \tag{2.98}$$

Again, we are restricted to using material descriptions for which

$$P^2({}^t\bar{p}) = 0. \tag{2.99}$$

If we further assume that the material law is linear, then an incremental solution procedure is no longer required and we can directly obtain the total solution using

$$\begin{bmatrix} \mathbf{KUU} & \mathbf{KUP} \\ \mathbf{KUP}^T & \mathbf{KPP} \end{bmatrix} \begin{bmatrix} {}^t\hat{\mathbf{u}} \\ {}^t\hat{\mathbf{p}} \end{bmatrix} = \begin{bmatrix} {}^t\mathbf{R} \\ \mathbf{0} \end{bmatrix}, \tag{2.100}$$

where the stiffness matrix is formed as in M.N.O. analysis. Since the material law is completely specified in terms of the constitutive constants tensor $\bar{C}_{klrs}$, we can write

$${}^t\bar{p} = -\tfrac{1}{3} \bar{C}_{aakl} {}^te_{kl} \tag{2.101}$$

so that

$$P({}^t\bar{p}) = \frac{\bar{C}_{aabb}}{9} \tag{2.102}$$

$$CPP = -9/\bar{C}_{aabb} \tag{2.103}$$

$$CUP_{kl} = -3\bar{C}_{aakl}/\bar{C}_{aabb} \tag{2.104}$$

$$CUU_{klrs} = \bar{C}_{klrs} - \frac{\bar{C}_{aakl} \bar{C}_{bbrs}}{\bar{C}_{aabb}}. \tag{2.105}$$

Since $P^2({}^t\bar{p})$ is always zero in this case, we need not make any material restriction.

2.5 *Some observations regarding the governing equations*

Equations (2.42) and (2.43) give the governing equations for the u/p formulation. The first equation represents the principle of virtual work. However, we notice that the stress tensor computed from displacements, ${}^t_0S_{kl}$, has been replaced by a new stress tensor, ${}^t_0S_{kl}$, which is given in eqn (2.41). This new stress tensor has the property that the pressure corresponding to the new stresses is equal to the separately interpolated pressure—the pressure computed from the displacements has been subtracted out.

The second equation is the constraint equation relating the separately interpolated pressure to the pressure computed from the displacements. Mathematically, this equation sets ${}^t\bar{p}$ to the projection of ${}^t\bar{p}$ onto the space of functions spanned by ${}^t\bar{p}$. Physically, this equation may be explained as follows. The quantity ${}^t\bar{p}$ contains some useful information and this information can be transferred to ${}^t\tilde{p}$. For example, the average of ${}^t\bar{p}$ over a finite element may be much more accurate than the value of ${}^t\bar{p}$ at specific points. Therefore we may wish to set the average of ${}^t\tilde{p}$ equal to the average of ${}^t\bar{p}$ over the finite element. The amount of information to be transferred from ${}^t\bar{p}$ to ${}^t\tilde{p}$ is governed by the order of the interpolation functions used for ${}^t\tilde{p}$ (the choice of interpolation functions will be discussed in greater detail below).

We may also interpret eqn (2.43) as a weakening of the material relationship between the pressure (${}^t\tilde{p}$) and the strains (represented by ${}^t\bar{p}$). The amount of weakening is governed by the order of the interpolation functions for ${}^t\tilde{p}$. Hence, even in linear elastic analysis, the stress–strain relationship is not satisfied at every point when the u/p formulation is employed. However the constraint equation ensures that the stress–strain relationship is satisfied on average within each element as described above.

The operation ${}_oP({}^t_o\bar{W})$ can also be written as

$$ {}^t\bar{p} = {}_oP({}^t_o\bar{W}) = -\frac{\mathrm{d}\,{}^t_o\bar{W}}{\mathrm{d}(\det {}^t_oX)}, \tag{2.106} $$

in which $\mathrm{d}(\det {}^t_oX)$ is an independent infinitesimal quantity. Consider the following increment in the Cauchy–Green deformation tensor:

$$ \mathrm{d}\,{}^t_oC_{ij} = ({}^t_oC_{ij})(\mathrm{d}\alpha) \tag{2.107} $$

where

$$ \mathrm{d}\alpha = \frac{2}{3\det {}^t_oX}\,\mathrm{d}(\det {}^t_oX). \tag{2.108} $$

This change in the Cauchy–Green deformation tensor causes a corresponding change in the potential;

$$ \mathrm{d}\,{}^t_o\bar{W} = \frac{\partial\,{}^t_o\bar{W}}{\partial\,{}^t_oC_{ij}}\,\mathrm{d}\,{}^t_oC_{ij} = \frac{1}{2}\frac{\partial\,{}^t_o\bar{W}}{\partial\,{}^t_o\varepsilon_{ij}}\,\mathrm{d}\,{}^t_oC_{ij} $$

(since ${}^t_o\varepsilon_{ij} = \tfrac{1}{2}({}^t_oC_{ij} - \delta_{ij})$)

$$ = \frac{1}{2}\frac{\partial\,{}^t_o\bar{W}}{\partial\,{}^t_o\varepsilon_{ij}}\,{}^t_oC_{ij}(\mathrm{d}\alpha) $$

$$ = \frac{1}{3\det {}^t_oX}\,{}^t_oC_{ij}\frac{\partial\,{}^t_o\bar{W}}{\partial\,{}^t_o\varepsilon_{ij}}\,\mathrm{d}(\det {}^t_oX) \tag{2.109} $$

and eqn (2.106) follows.

The reason we use $\mathrm{d}(\det {}^t_oX)$ to control the magnitude of the change in ${}^t_oC_{ij}$ given in eqn (2.107) is that the corresponding change in $\det {}^t_oX$ is simply

$$ (1+\mathrm{d}\alpha)^{3/2}(\det {}^t_oC)^{1/2} - (\det {}^t_oC)^{1/2} $$

$$ = \left[1 + \frac{3}{2}\left(\frac{2}{3\det {}^t_oX}\right)\mathrm{d}(\det {}^t_oX) - 1\right]\det {}^t_oX $$

$$ = \mathrm{d}(\det {}^t_oX). \tag{2.110} $$

This procedure can be applied to any function $f({}^t_oC_{ij})$ to determine ${}_oP(f)$. Simply choose $\mathrm{d}(\det {}^t_oX)$, compute the corresponding change in the Cauchy–Green deformation tensor, $\mathrm{d}\,{}^t_oC_{ij}$, compute the corresponding change in the function, $\mathrm{d}f$, and divide $-\mathrm{d}f$ by $\mathrm{d}(\det {}^t_oX)$ to obtain ${}_oP(f)$. The procedure may be used to determine whether ${}_oP(f)$ is zero; if $\mathrm{d}f$ is zero, ${}_oP(f)$ is also zero. We call a function for which ${}_oP(f)$ is zero a function that is insensitive to the magnitude of the volume ratio $\det {}^t_oX$. These functions are useful when constructing material descriptions, as we discuss in Sec. 3.

To study the meaning of ${}_oP({}^t\bar{p})$, assume that the material law used is that of linear isotropic elasticity and that small strains are considered. Then

$$ {}^t\bar{p} = -\kappa\,{}^te_{ii}, \tag{2.111} $$

where κ is the bulk modulus. From this

$$ P({}^t\bar{p}) = -\frac{1}{3}\sum_{i=1}^{3}\frac{\partial\,{}^t\bar{p}}{\partial e_{ii}} = \kappa. \tag{2.112} $$

Also $P^2({}^t\bar{p})$ is zero, so that the material restriction is satisfied. Now suppose that the material is nonlinear elastic, with the pressure a function only of $\det {}^t_oX$. Then

$$ {}_oP({}^t\bar{p}) = -\frac{\mathrm{d}\,{}^t\bar{p}}{\mathrm{d}(\det {}^t_oX)} \tag{2.113} $$

and the material restriction is

$$ {}_oP^2({}^t\bar{p}) = \frac{\mathrm{d}^2\,{}^t\bar{p}}{\mathrm{d}(\det {}^t_oX)^2} = 0. \tag{2.114} $$

We can integrate the last equation to give, assuming that the pressure is zero for zero deformations,

$$ {}^t\bar{p} = -\kappa(\det {}^t_0\mathbf{X} - 1), \tag{2.115} $$

in which $\kappa = {}_0P({}^t\bar{p})$ is the bulk modulus. From these examples, we see that, in an isotropic material, ${}_0P({}^t\bar{p})$ physically represents a bulk modulus and that the material restriction is that the bulk modulus be insensitive to changes in the volume ratio $\det {}^t_0\mathbf{X}$.

Finally we mention that the final constraint eqn (2.43) depends upon our initial choice for the form of the constraint equation (eqn (2.18)). As was seen, the material restriction (2.23) is a direct consequence of this choice. If we wanted to consider materials that do not satisfy eqn (2.23), we would have to revise our initial choice of constraint equation. For our purposes, the material restriction (2.23) is not overly restrictive, so we do not discuss other constraint equations in this paper. Indeed, in the following discussions we assume that ${}_0P({}^t\bar{p})$ is constant.

3. IMPLEMENTATION OF SOME MATERIAL DESCRIPTIONS

In this section, we summarize the material descriptions used in the example problems. The emphasis of this section is on the calculation of the additional quantities needed in the *u/p* formulation. For the general nonlinear formulation, these quantities are

$$ {}^t\bar{p}, \quad {}_0P({}^t\bar{p}), \quad \frac{\partial {}^t\bar{p}}{\partial {}^t_0\varepsilon_{kl}}, \quad \frac{\partial^2 {}^t\bar{p}}{\partial {}^t_0\varepsilon_{kl}\, \partial {}^t_0\varepsilon_{rs}} $$

using the total Lagrangian expressions or

$$ {}^t\bar{p}, \quad {}_TP({}^t\bar{p}), \quad \frac{\partial {}^t\bar{p}}{\partial {}_te_{kl}}, \quad \frac{\partial^2 {}^t\bar{p}}{\partial {}_te_{kl}\, \partial {}_te_{rs}} $$

using the updated Lagrangian expressions. For the small strain formulations, these reduce to

$$ {}^t\bar{p}, \quad P({}^t\bar{p}), \quad \frac{\partial {}^t\bar{p}}{\partial {}^te_{kl}}, \quad \frac{\partial^2 {}^t\bar{p}}{\partial {}^te_{kl}\, \partial {}^te_{rs}}. $$

A material law subroutine in a finite element program must return these quantities as well as the quantities required in displacement-based finite element analysis.

3.1 *Isotropic linear elasticity (small strains, small displacements)*

The simplest material description is that of isotropic linear elasticity, in which

$$ \bar{C}_{klrs} = \lambda\delta_{kl}\delta_{rs} + \mu(\delta_{kr}\delta_{ls} + \delta_{ks}\delta_{lr}) \tag{3.1} $$

where λ and μ are the Lamé constants

$$ \lambda = \frac{Ev}{(1+v)(1-2v)} \tag{3.2a} $$

$$ \mu = \frac{E}{2(1+v)}. \tag{3.2b} $$

We obtain

$$ {}^t\bar{p} = -\kappa\, {}^te_{mm} \tag{3.3a} $$

$$ P({}^t\bar{p}) = \kappa \tag{3.3b} $$

$$ \frac{\partial {}^t\bar{p}}{\partial e_{kl}} = -\kappa\delta_{kl} \tag{3.3c} $$

$$ \frac{\partial^2 {}^t\bar{p}}{\partial e_{kl}\, \partial e_{rs}} = 0, \tag{3.3d} $$

where κ is the bulk modulus

$$ \kappa = \frac{E}{3(1-2v)} \tag{3.4} $$

and we see that

$$ CPP = -1/\kappa \tag{3.5} $$

$$ CUP_{kl} = -\delta_{kl} \tag{3.6} $$

$$ CUU_{klrs} = \bar{C}_{klrs} - \kappa\delta_{kl}\delta_{rs}. \tag{3.7} $$

As a consequence

$$ {}^t\tau_{kl} = {}^ts_{kl} - \delta_{kl}\, {}^t\bar{p}, \tag{3.8} $$

where ${}^ts_{kl}$ is the deviatoric stress tensor. Here we can directly see that the pressure computed from displacements has been eliminated from the stress tensor.

3.2 *Anisotropic linear elasticity (small strains, small displacements)*

The most general form of small strain, small displacement linear elasticity consistent with the assumption of a potential is

$$ {}^t\bar{\tau}_{kl} = \bar{C}_{klrs}\, {}^te_{rs};\ \bar{C}_{klrs} = \bar{C}_{rskl}. \tag{3.9} $$

The formation of CPP, CUP_{kl} and CUU_{klrs} was discussed in Sec. 2.4. Here we want to compare the equations corresponding to the anisotropic material to those of the isotropic material.

For the anisotropic material description

$$ {}^t\tau_{kl} = {}^t\bar{\tau}_{kl} + CPP({}^t\bar{p} - {}^t\tilde{p})\frac{\partial {}^t\bar{p}}{\partial e_{kl}} $$

$$ = \left(\bar{C}_{klrs} - \frac{\bar{C}_{aakl}\bar{C}_{bbrs}}{\bar{C}_{aabb}}\right){}^te_{rs} - \left(\frac{3\bar{C}_{aakl}}{\bar{C}_{aabb}}\right){}^t\tilde{p}. \tag{3.10} $$

We see that, compared with the isotropic description,

$$\left(\bar{C}_{klrs} - \frac{\bar{C}_{aakl}\bar{C}_{bbrs}}{\bar{C}_{aabb}}\right){}^{t}e_{rs}$$

is analogous to the deviatoric stresses and

$$\frac{3\bar{C}_{aakl}}{\bar{C}_{aabb}}$$

is analogous to the Kronecker delta. Also the term $\bar{C}_{aabb}/9$ is equivalent to the isotropic bulk modulus and when it becomes infinite, ${}^{t}\bar{p}$ is decoupled from the strains.

However

$$\left(\bar{C}_{klrs} - \frac{\bar{C}_{aakl}\bar{C}_{bbrs}}{\bar{C}_{aabb}}\right){}^{t}e_{rs} \neq {}^{t}s_{kl}$$

and

$$\frac{3\bar{C}_{aakl}}{\bar{C}_{aabb}} \neq \delta_{kl}$$

in general. Trying to use the decomposition

$${}^{t}\tau_{kl} = {}^{t}s_{kl} - \delta_{kl}{}^{t}\bar{p} \tag{3.11}$$

as the basis of the anisotropic u/p formulation is not desirable because the relationship between ${}^{t}s_{kl}$ and ${}^{t}e_{rs}$ is not in general symmetric:

$$\begin{aligned} {}^{t}s_{kl} &= {}^{t}\bar{\tau}_{kl} + \delta_{kl}{}^{t}\bar{p} \\ &= (\bar{C}_{klrs} - \tfrac{1}{3}\delta_{kl}\bar{C}_{aars}){}^{t}e_{rs}. \end{aligned} \tag{3.12}$$

Also note that as $\bar{C}_{aabb}/9$ increases to infinity ${}^{t}\bar{p}$ does not necessarily become decoupled from the volumetric strain. Rather ${}^{t}\bar{p}$ becomes decoupled from the weighted sum of strains

$$\frac{3\bar{C}_{aars}}{\bar{C}_{aabb}}{}^{t}e_{rs}$$

which in isotropic analysis reduces to the volumetric strain.

A new term is needed to describe materials for which

$$\frac{3\bar{C}_{aars}}{\bar{C}_{aabb}}{}^{t}e_{rs}$$

is always zero. We propose the term 'semideformable' materials—incompressible materials are then a special case of semideformable materials. It is this more general class of semideformable materials which requires the use of the u/p formulation for effective finite element analysis.

3.3 *Elasto-plasticity (small strains, small displacements)*

An often-used elasto-plastic material description incorporates a von Mises yield condition and isotropic hardening (no hardening can also be obtained as a special case). This material description is discussed in [1] and in particular the incremental elastic–plastic stress–strain matrix $\mathbf{C}^{EP}$ is derived. In this section, we discuss only how this material description is incorporated into the u/p formulation.

There are two important facts that simplify the process of installing this material description into the u/p formulation:

(1) The yield surface does not depend on the hydrostatic pressure.
(2) The relationship between the pressure and the volumetric strain is simple,

$$\mathrm{d}\,{}^{t}\bar{p} = -\kappa\,\mathrm{d}\,{}^{t}e_{mm}, \tag{3.13}$$

in which κ is the bulk modulus defined above and this relationship is valid for elastic or plastic conditions.

Because of the simple pressure–strain relationship, we can directly write

$$P({}^{t}\bar{p}) = \kappa \tag{3.14a}$$

$$\frac{\partial\,{}^{t}\bar{p}}{\partial e_{ij}} = -\kappa\delta_{ij} \tag{3.14b}$$

$$\frac{\partial^2\,{}^{t}\bar{p}}{\partial e_{ij}\,\partial e_{rs}} = 0. \tag{3.14c}$$

Given the stress at time t, the stress computed from displacements at time $t + \Delta t$ is calculated by evaluating

$${}^{t+\Delta t}\bar{\tau}_{kl} = {}^{t}\tau_{kl} + \int_{{}^{t}e_{rs}}^{{}^{t+\Delta t}e_{rs}} \bar{C}_{klrs}\,\mathrm{d}e_{rs} \tag{3.15}$$

using, for example, the effective-stress-function algorithm [28]. The corresponding pressure computed from displacements is then calculated using ${}^{t+\Delta t}\bar{p} = -\frac{1}{3}{}^{t+\Delta t}\bar{\tau}_{ii}$ and the stress at time $t + \Delta t$ is simply

$${}^{t+\Delta t}\tau_{kl} = {}^{t+\Delta t}\bar{\tau}_{kl} + \delta_{kl}({}^{t+\Delta t}\bar{p} - {}^{t+\Delta t}\bar{p}). \tag{3.16}$$

We note that the entire integration from time t to time $t + \Delta t$ can be performed without knowledge of the interpolated pressure ${}^{t+\Delta t}\bar{p}$ because the contents of $\bar{C}_{klrs}$ are pressure-independent. For more complicated material descriptions (e.g. the Drucker–Prager models), the interpolated pressure might have to be introduced into the calculation of $\bar{C}_{klrs}$.

3.4 *Mooney–Rivlin material description*

The Mooney–Rivlin material description is used to characterize rubber-like materials undergoing large strains. The conventional Mooney–Rivlin material is [29, 30]

$$ {}^t_0\bar{W} = C_1({}^t_0I_1 - 3) + C_2({}^t_0I_2 - 3); \quad {}^t_0I_3 = 1, \tag{3.17} $$

where C_1, C_2 are material constants and

$$ {}^t_0I_1 = {}^t_0C_{kk} \tag{3.18a} $$

$$ {}^t_0I_2 = \tfrac{1}{2}({}^t_0I_1)^2 - {}^t_0C_{ij}\,{}^t_0C_{ij} \tag{3.18b} $$

$$ {}^t_0I_3 = \det {}^t_0\mathbf{C}. \tag{3.18c} $$

A neo-Hookean material description is a Mooney–Rivlin material description with $C_2 = 0$. Note that, for small strains, $2(C_1 + C_2)$ represents the shear modulus and $6(C_1 + C_2)$ represents the Young's modulus.

This material description assumes that rubber is totally incompressible. A better assumption is that the bulk modulus of rubber is several thousand times as large as the shear modulus [2, 31, 32]. Therefore it is reasonable to assume that rubber is almost incompressible. This is accomplished by dropping the restriction ${}^t_0I_3 = 1$ and including a hydrostatic work term in the strain energy function. We obtain

$$ {}^t_0\bar{W} = C_1({}^t_0I_1 - 3) + C_2({}^t_0I_2 - 3) + W_H({}^t_0I_3). \tag{3.19} $$

However, we cannot directly use this description because all three terms contribute to the pressure:

$$ {}^t\bar{p} = C_1\,{}_0P({}^t_0I_1) + C_2\,{}_0P({}^t_0I_2) + {}_0P(W_H({}^t_0I_3)) \tag{3.20} $$

and in particular ${}_0P^2({}_0P({}^t_0I_1))$ and ${}_0P^2({}_0P({}^t_0I_2))$ are nonzero. To see that ${}_0P({}^t_0I_1)$ and ${}_0P({}^t_0I_2)$ contribute to the pressure, notice that ${}^t_0I_1$ and ${}^t_0I_2$ are sensitive to the magnitude of the volume ratio, therefore ${}^t_0I_1$ and ${}^t_0I_2$ change as the perturbation (2.107) is applied. To circumvent this problem, we use the reduced invariants [31]

$$ {}^t_0J_1 = {}^t_0I_1\,{}^t_0I_3^{-1/3} \tag{3.21a} $$

$$ {}^t_0J_2 = {}^t_0I_2\,{}^t_0I_3^{-2/3}. \tag{3.21b} $$

These are insensitive to the magnitude of the volume ratio, therefore ${}_0P({}^t_0J_1)$ and ${}_0P({}^t_0J_2)$ are zero. We find it easier to work with $\det {}^t_0\mathbf{X}$ rather than $\det {}^t_0\mathbf{C}$ so we define

$$ {}^t_0J_3 = \det {}^t_0\mathbf{X} = {}^t_0I_3^{1/2}. \tag{3.22} $$

With these substitutions, the strain energy density becomes

$$ {}^t_0\bar{W} = C_1({}^t_0J_1 - 3) + C_2({}^t_0J_2 - 3) + W_H({}^t_0J_3). \tag{3.23} $$

Now we choose W_H to satisfy the material restriction ${}_0P^2({}^t\bar{p}) = 0$. Since ${}^t\bar{p}$ depends only on ${}^t_0J_3$, we can use the results of Sec. 2.5 to obtain

$$ {}^t\bar{p} = -\kappa({}^t_0J_3 - 1) \tag{3.24a} $$

$$ {}_0P({}^t\bar{p}) = \kappa \tag{3.24b} $$

$$ {}^t_0W_H = \tfrac{1}{2}\kappa({}^t_0J_3 - 1)^2. \tag{3.25} $$

Here κ is an additional material constant representing the bulk modulus.

The stresses (computed from displacements) corresponding to the strain energy density are computed using

$$ {}^t_0\bar{S}_{kl} = \frac{1}{2}\left(\frac{\partial\,{}^t_0\bar{W}}{\partial\,{}^t_0\varepsilon_{kl}} + \frac{\partial\,{}^t_0\bar{W}}{\partial\,{}^t_0\varepsilon_{lk}}\right) \tag{3.26} $$

and the constitutive tensor is computed using

$$ {}_0\bar{C}_{klrs} = \frac{1}{2}\left(\frac{\partial\,{}^t_0\bar{S}_{kl}}{\partial\,{}^t_0\varepsilon_{rs}} + \frac{\partial\,{}^t_0\bar{S}_{kl}}{\partial\,{}^t_0\varepsilon_{sr}}\right). \tag{3.27} $$

The details of these calculations are given in Appendix A. The calculation of the pressure derivatives needed for the u/p formulation is performed using chain differentiation:

$$ \frac{\partial\,{}^t\bar{p}}{\partial\,{}^t_0\varepsilon_{kl}} = -\kappa\,{}^t_0J_3\,{}^0_tC_{kl} \tag{3.28} $$

$$ \frac{\partial^2\,{}^t\bar{p}}{\partial\,{}^t_0\varepsilon_{kl}\,\partial\,{}^t_0\varepsilon_{rs}} = \kappa\,{}^t_0J_3\,{}^0_tC_{kl}\,{}^0_tC_{rs} - \kappa\,{}^t_0J_3^{-1}(\hat{\varepsilon}_{krc}\,\hat{\varepsilon}_{lsf} + \hat{\varepsilon}_{ksc}\,\hat{\varepsilon}_{lrf})\,{}^t_0C_{cf}, \tag{3.29} $$

where $\hat{\varepsilon}_{ijk}$ is the permutation tensor and ${}^0_tC_{kl}$ is the inverse of the Cauchy–Green deformation tensor.

3.5 *Ogden material description*

The Ogden material description is used to characterize rubber-like materials undergoing large strains. It is often used in the three-term form [33]

$$ {}^t_0\bar{W} = \sum_{n=1}^{3} \frac{\mu_n}{\alpha_n}(\lambda_1^{\alpha_n} + \lambda_2^{\alpha_n} + \lambda_3^{\alpha_n} - 3); \quad \lambda_1\lambda_2\lambda_3 = 1, \tag{3.30} $$

where the λ_i are the principal stretches of the stretch tensor ${}^t_0\mathbf{U} = ({}^t_0\mathbf{C})^{1/2}$ and the μ_i and α_i are material constants determined from experimental data. We

note that the sum $\frac{1}{2}\sum_{n=1}^{3}\alpha_n\mu_n$ is the small-strain shear modulus. The Mooney–Rivlin material description can be obtained from the Ogden description by using

$$\mu_1 = 2C_1, \qquad \mu_2 = -2C_2, \qquad \mu_3 = 0$$

$$\alpha_1 = 2, \qquad \alpha_2 = -2, \qquad \alpha_3 = 0.$$

We prefer to work with the principal values of ${}^t_0\mathbf{C}$, which we denote as L_1, L_2, L_3, rather than with the principal values of ${}^t_0\mathbf{U}$. Using the L_i, the Ogden description becomes

$${}^t_0\bar{W} = \sum_{n=1}^{3}\frac{\mu_n}{\alpha_n}(L_1^{\alpha_n/2} + L_2^{\alpha_n/2} + L_3^{\alpha_n/2} - 3); \qquad L_1L_2L_3 = 1. \quad (3.31)$$

As in the case of the Mooney–Rivlin material, we assume that rubber is almost incompressible; therefore we drop the condition $L_1L_2L_3 = 1$ and include a hydrostatic work term W_H in the strain energy density function. Now we notice that

$${}_0P({}^t_0\bar{W}) = \frac{1}{2}\sum_{n=1}^{3}\mu_n[(L_1^{\alpha_n/2-1}\,{}_0P(L_1) + L_2^{\alpha_n/2-1}\,{}_0P(L_2) + L_3^{\alpha_n/2-1}\,{}_0P(L_3)] + {}_0P(W_H), \quad (3.32)$$

where ${}_0P(L_i) \neq 0$ because L_i is sensitive to the magnitude of the volume ratio. Therefore we replace the L_i with the terms $L_i(L_1L_2L_3)^{-1/3}$, which are unaffected by the magnitude of the volume ratio. The modified Ogden material description is

$${}^t_0\bar{W} = \sum_{n=1}^{3}\left\{\frac{\mu_n}{\alpha_n} \times [(L_1^{\alpha_n/2} + L_2^{\alpha_n/2} + L_3^{\alpha_n/2})(L_1L_2L_3)^{-\alpha_n/6} - 3]\right\} + W_H({}^t_0J_3), \quad (3.33)$$

where ${}^t_0J_3$ is defined in eqn (3.22).

As with the Mooney–Rivlin description, we use eqn (3.25) to define W_H. The stresses (as computed from displacements) are calculated from (3.26) and the constitutive tensor is calculated from (3.27). The results for two-dimensional analysis are given in Appendix B. Finally the pressure derivatives needed for the u/p formulation are identical to those used in the Mooney–Rivlin material description (eqns (3.28) and (3.29)).

4. SOLUTION OF EQUATIONS IN INCREMENTAL NONLINEAR ANALYSIS

For incremental nonlinear analysis, the equations have the form given in eqn (2.27). The goal of the equation solution procedure is to obtain displacements and pressures so that the right-hand-side of (2.27) is identically zero. Equation (2.27) gives increments to the displacements and pressures that will (hopefully) reduce the magnitude of the right-hand-side entries.

In theory, we could solve the equations in the form of (2.27). However, because we use pressure discretizations that are discontinuous between elements, it is more efficient to statically condense out the pressure degrees of freedom at the element level. In other words, for a finite element, we have

$$\mathbf{KUU}\,\hat{\mathbf{u}} + \mathbf{KUP}\,\hat{\mathbf{p}} = \mathbf{R} - \mathbf{FU} \quad (4.1)$$

$$\mathbf{KUP}^T\hat{\mathbf{u}} + \mathbf{KPP}\,\hat{\mathbf{p}} = \mathbf{0} - \mathbf{FP} \quad (4.2)$$

(omitting left superscripts for brevity). We solve for $\hat{\mathbf{p}}$ using the second equation (note that $\hat{\mathbf{u}}$ is unknown at this point)

$$\hat{\mathbf{p}} = \mathbf{KPP}^{-1}(-\mathbf{FP} - \mathbf{KUP}^T\hat{\mathbf{u}}) \quad (4.3)$$

and substitute eqn (4.3) into eqn (4.1) to obtain

$$\mathbf{K}\hat{\mathbf{u}} = \mathbf{R} - \mathbf{F}, \quad (4.4)$$

where

$$\mathbf{K} = \mathbf{KUU} - \mathbf{KUP}\,\mathbf{KPP}^{-1}\,\mathbf{KUP}^T \quad (4.5)$$

$$\mathbf{F} = \mathbf{FU} - \mathbf{KUP}\,\mathbf{KPP}^{-1}\,\mathbf{FP}. \quad (4.6)$$

In practice, the calculation of $\mathbf{K}$ and $\mathbf{F}$ is performed using Gauss elimination. The element stiffness matrix $\mathbf{K}$ and force vector $\mathbf{F}$ are then assembled into the global stiffness matrix and force vector in the usual way. Once the global set of equations has been solved, $\hat{\mathbf{u}}$ is known and the pressure increments are recovered at the element level using eqn (4.3).

An important point is that, within each iteration, we are solving for the increments in ${}^t\hat{\mathbf{p}}$ and ${}^t\hat{\mathbf{u}}$. The total pressures are obtained by summing increments in a manner analogous to that used in calculating the total displacements. We are only using the static condensation procedure to speed up the equation solution procedure; we would obtain the same numerical results had we used the original eqns (2.27).

In contact analysis, we use the following procedure when the out-of-balance load vector is employed to calculate reactions. First the true out-of-balance load vector $\mathbf{R} - \mathbf{FU}$ is used to calculate reactions. Then $\mathbf{R} - \mathbf{FU}$ is updated by $\mathbf{KUP}\,\mathbf{KPP}^{-1}\,\mathbf{FP}$ to produce $\mathbf{R} - \mathbf{F}$. This procedure ensures that the additional vector $\mathbf{KUP}\,\mathbf{KPP}^{-1}\,\mathbf{FP}$ is not included in the contact reaction calculations, because this vector is only a mathematical entity used in the static condensation procedure.

The equation solution procedure outlined in eqns (4.1) through (4.6) may be contrasted with the

approach used by Bercovier *et al.* [19], Häggblad and Sundberg [23], Zdunek and Bercovier [25] and Häggblad and Bathe [22]. In these formulations ${}^t\hat{p}$ is written in terms of the total displacements. The resulting expressions are used to replace the separately interpolated pressures in the out-of-balance force vector, which is therefore written entirely in terms of displacements. The corresponding tangent stiffness matrix is derived by linearization. Hence the constraint equation is always satisfied and the pressure variables are removed from the incremental equations of motion. This approach can result in convergence difficulties when using the full Newton iteration procedure.

5. SELECTION OF EFFECTIVE ELEMENTS

In this section, we compare the solution behavior of different two-dimensional u/p elements. The displacement interpolations considered are standard isoparametric interpolations that are at most parabolic. For the pressures, we assume a polynomial expansion of the form

$$ {}^t\tilde{p} = {}^tp_1 + {}^tp_2 r + {}^tp_3 s + {}^tp_4 rs + \cdots, \quad (5.1) $$

Table 5.1. Polynomial expansions for separately interpolated pressure

Number of pressure degrees of freedom	Pressure interpolation functions								
	g_1	g_2	g_3	g_4	g_5	g_6	g_7	g_8	g_9
1	1								
3	1	r	s						
4	1	r	s	rs					
6	1	r	s	rs	r^2	s^2			
8	1	r	s	rs	r^2	s^2	r^2s	rs^2	
9	1	r	s	rs	r^2	s^2	r^2s	rs^2	r^2s^2

${}^t\tilde{p} = \sum g_L {}^tp_L$.

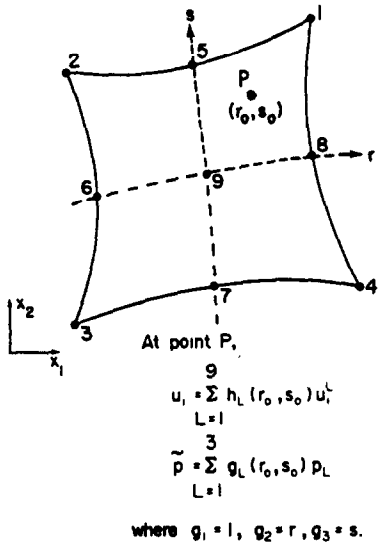

Fig. 5.1. Nine/three displacement–pressure element.

where ${}^tp_1, {}^tp_2, \ldots$ are internal element variables and r, s are the element isoparametric coordinates (Table 5.1). The variables ${}^tp_1, {}^tp_2, \ldots$ may be associated with the pressure degrees of freedom ${}^t\hat{p}_i$ introduced earlier. Notice that the pressure may be discontinuous between elements; therefore static condensation is employed at the element level as described in Sec. 4. Figure 5.1 shows a typical u/p element with nine nodes and three pressure variables. We call this a 9/3 element and the same nomenclature is used for other u/p elements. (If the number of pressure variables is not given for an element, the element is displacement-based.)

One characteristic of the u/p elements is that the patch test [1] is always satisfied. Another characteristic is that as the number of pressure degrees of freedom is increased (holding the number of nodes fixed), a u/p element behaves more and more like a

Table 5.2. Eigenvalues of the nine-node element shown in Fig. 5.2

Mode number	Number of pressure degrees of freedom						
	1	3	4	6	8	9	Disp.-based
1	0	0	0	0	0	0	0
2	0	0	0	0	0	0	0
3	0	0	0	0	0	0	0
4	5.452×10^1	1.019×10^2	1.027×10^2	1.984×10^2	2.171×10^2	3.119×10^2	3.119×10^2
5	8.744×10^1	1.711×10^2	1.961×10^2	2.487×10^2	3.131×10^2	4.234×10^2	4.234×10^2
6	2.023×10^2	2.779×10^2	3.958×10^2	4.161×10^2	5.263×10^2	5.861×10^2	5.861×10^2
7	2.388×10^2	4.173×10^2	4.969×10^2	5.123×10^2	5.893×10^2	6.398×10^2	6.398×10^2
8	4.170×10^2	5.068×10^2	5.069×10^2	6.188×10^2	6.529×10^2	7.531×10^2	7.531×10^2
9	4.832×10^2	6.570×10^2	6.944×10^2	7.260×10^2	9.489×10^2	1.058×10^3	1.058×10^3
10	7.185×10^2	7.811×10^2	8.036×10^2	8.225×10^2	1.096×10^3	2.160×10^3	2.160×10^3
11	7.866×10^2	8.412×10^2	9.258×10^2	1.059×10^3	2.057×10^4	2.162×10^4	2.162×10^4
12	8.162×10^2	9.671×10^2	1.044×10^3	1.167×10^3	1.081×10^5	1.086×10^5	1.086×10^5
13	1.052×10^3	1.140×10^3	1.204×10^3	7.330×10^4	1.448×10^5	1.499×10^5	1.499×10^5
14	1.132×10^3	1.211×10^3	1.722×10^3	1.563×10^5	2.154×10^5	2.373×10^5	2.373×10^5
15	1.221×10^3	1.734×10^3	3.493×10^5	3.550×10^5	3.689×10^5	3.757×10^5	3.757×10^5
16	2.722×10^3	3.493×10^5	3.653×10^5	3.728×10^5	4.027×10^5	4.048×10^5	4.048×10^5
17	3.005×10^3	6.353×10^5	6.356×10^5	6.442×10^5	6.717×10^5	6.808×10^5	6.808×10^5
18	3.696×10^5	7.776×10^5	8.530×10^5	8.676×10^5	9.396×10^5	9.423×10^5	9.423×10^5

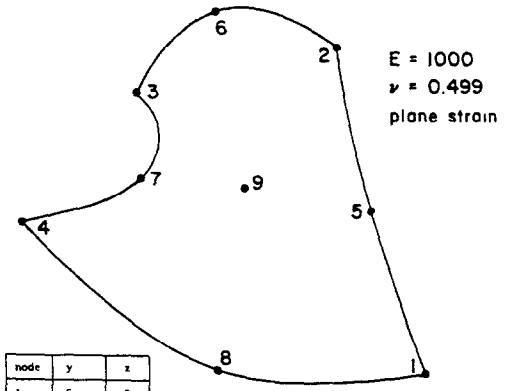

node	y	z
1	5	0
2	4	4
3	1.5	3.5
4	0	2
5	4.4	2
6	2.5	4.5
7	1.5	2.5
8	2.4	0.1
9	2.8	2.3

Fig. 5.2. Distorted 9/3 element used in eigenvalue calculations.

displacement-based element. This behavior can be seen in linear analysis by computing the eigenvalues of the element stiffness matrix for different pressure interpolations. As an example, in Table 5.2 we tabulate the eigenvalues of the nine-node element shown in Fig. 5.2 in which we use 1, 3, 4, 6, 8 and 9 pressure degrees of freedom. Three by three Gauss integration is employed to integrate the element stiffness matrix and static condensation is employed. It is seen that the element stiffens as the number of pressure degrees of freedom is increased and that the element always contains the correct number of rigid-body modes. An interesting observation is that when the number of pressure degrees of freedom equals the number of integration points, the stiffness matrix of the displacement-based element is recovered (the eigenvalues of the 9/9 element equal the eigenvalues of the displacement-based element). This always happens if the number of pressure degrees of freedom equals the number of integration points because, in this case, the only way in which the constraint equations can be satisfied is to select the coefficients of ${}^t\tilde{p}$ so that ${}^t\tilde{p} = {}^t\bar{p}$ at each integration point.

Evidently we must use fewer pressure degrees of freedom than integration points in an effective u/p element. However, if we do not use enough pressure degrees of freedom, then the element will be unable to model complex pressure variations. Therefore we would like to use as many pressure degrees of freedom as possible. On the other hand, if the element has too many pressure degrees of freedom, the solution accuracy of an assemblage of elements may degrade as the bulk modulus (or Poisson's ratio in isotropic linear elastic analysis) increases. This 'locking' behavior can have a disastrous effect in the response prediction. Therefore the best pressure approximation corresponding to a given displacement interpolation is the one of highest order for which assemblages of elements do not lock [34].

As an example, we consider the analysis of a square block subjected to concentrated loads (Fig. 5.3). We perform a linear analysis assuming an isotropic material. The mesh used to test the eight- and nine-node elements is shown in Fig. 5.3; the mesh used to test the four-node elements is obtained by subdividing each element into four smaller ele-

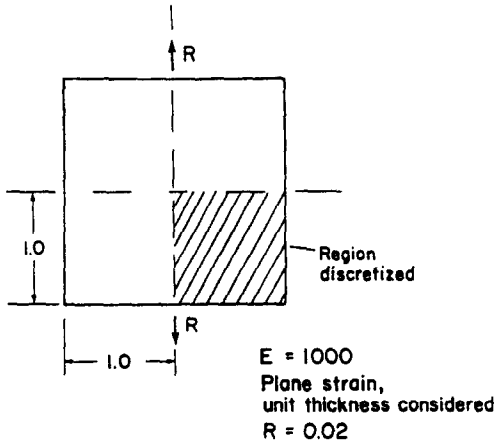

(a)

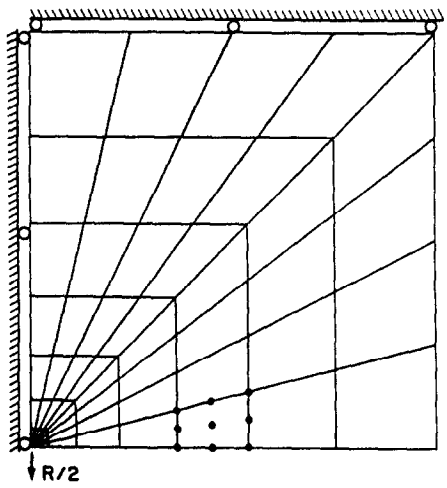

(b)

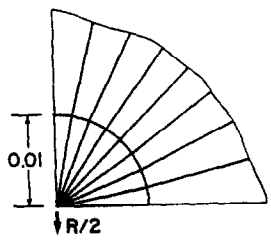

(c)

Fig. 5.3. Square block subjected to concentrated loads. (a) Dimensions. (b) Mesh layout. (c) Detail of mesh at loading point.

ments. Three by three Gauss integration is employed for the eight- and nine-node elements and 2×2 Gauss integration is employed for the four-node elements. We note that a $1/r$ stress singularity is present and expect that the finite elements will not be able to give accurate stresses near the point of load application. However, for the purpose of this study, we are not primarily interested in obtaining an accurate solution, but are only interested in comparing the relative effectiveness of different elements in almost incompressible analysis.

We use the total strain energy,

$$ {}^{t}\mathscr{U}_{tot} = \int_V \tfrac{1}{2}\, {}^{t}\tau_{ij}\, {}^{t}e_{ij}\, dV, \tag{5.2} $$

volumetric strain energy,

$$ {}^{t}\mathscr{U}_{vol} = \int_V \frac{{}^{t}p^2}{2\kappa}\, dV, \tag{5.3} $$

and root-mean-square pressure,

$$ {}^{t}p_{rms} = \sqrt{\frac{\int_V {}^{t}p^2\, dV}{\int_V dV}} = \sqrt{\frac{2\kappa\, {}^{t}\mathscr{U}_{vol}}{\int_V dV}}, \tag{5.4} $$

to evaluate the degree of locking of each solution. In the calculation of these quantities, we do not include the elements closest to the point of load application because of the singularity at that point (Fig. 5.3). For the eight- and nine-node element meshes, the first

Table 5.3. Total strain energy, volumetric strain energy and root-mean-square pressure for square block analyses (results given to three significant digits)

Element type	ν	Total strain energy	Volumetric strain energy	Root-mean-square pressure
Four-node	0.0	2.81×10^{-7}	7.76×10^{-8}	0.00719
	0.4	2.63×10^{-7}	3.60×10^{-8}	0.0110
	0.49	2.28×10^{-7}	3.90×10^{-8}	0.0361
	0.499	1.38×10^{-7}	4.11×10^{-8}	0.117
	0.4999	8.50×10^{-8}	9.33×10^{-9}	0.176
	0.49999	7.61×10^{-8}	1.07×10^{-9}	0.189
	0.499999	7.51×10^{-8}	1.09×10^{-10}	0.190
	0.4999999	7.50×10^{-8}	1.09×10^{-11}	0.191
	0.49999999	7.50×10^{-8}	1.09×10^{-12}	0.191
4/1				
	0.0	2.81×10^{-7}	7.73×10^{-8}	0.00718
	0.4	2.65×10^{-7}	3.06×10^{-8}	0.0101
	0.49	2.52×10^{-7}	3.48×10^{-9}	0.0108
	0.49999999	2.51×10^{-7}	3.53×10^{-15}	0.0109
Eight-node				
	0.0	2.87×10^{-7}	7.96×10^{-8}	0.00728
	0.4	2.68×10^{-7}	3.24×10^{-8}	0.0104
	0.49	2.55×10^{-7}	1.19×10^{-8}	0.0199
	0.49999999	8.27×10^{-8}	4.46×10^{-9}	8.62
8/4				
	0.0	2.87×10^{-7}	7.96×10^{-8}	0.00728
	0.4	2.68×10^{-7}	3.13×10^{-8}	0.0102
	0.49	2.57×10^{-7}	4.67×10^{-9}	0.0125
	0.49999999	2.77×10^{-7}	2.90×10^{-13}	0.0984
8/3				
	0.0	2.87×10^{-7}	7.96×10^{-8}	0.00728
	0.4	2.68×10^{-7}	3.12×10^{-8}	0.0102
	0.49	2.54×10^{-7}	3.58×10^{-9}	0.0109
	0.49999999	2.53×10^{-7}	3.69×10^{-15}	0.0111
Nine-node				
	0.0	2.86×10^{-7}	7.96×10^{-8}	0.00728
	0.4	2.68×10^{-7}	3.22×10^{-8}	0.0104
	0.49	2.53×10^{-7}	9.71×10^{-9}	0.0180
	0.49999999	1.57×10^{-7}	1.06×10^{-11}	0.595
9/4				
	0.0	2.86×10^{-7}	7.96×10^{-8}	0.00728
	0.4	2.68×10^{-7}	3.12×10^{-8}	0.0102
	0.49	2.54×10^{-7}	3.54×10^{-8}	0.0109
	0.49999999	2.52×10^{-7}	3.60×10^{-15}	0.0110
9/3				
	0.0	2.86×10^{-7}	7.95×10^{-8}	0.00728
	0.4	2.68×10^{-7}	3.12×10^{-8}	0.0102
	0.49	2.54×10^{-7}	3.53×10^{-9}	0.0108
	0.49999999	2.52×10^{-7}	3.58×10^{-15}	0.0109

ring of elements is not included. For the four-node element meshes, the first and second rings of elements are not included because two rings of four-node elements are used to model the same region as one ring of eight- or nine-node elements.

Some numerical results are given in Table 5.3. First we consider the four-node element and the 4/1 element. Of particular interest is the behavior of the root-mean-square pressure from the displacement-based element results; as ν is increased, the root-mean-square pressure increases by a factor of 25 and then levels off. This behavior is physically unrealistic and is characteristic of locking. The 4/1 element also locks, but the degree of locking is small; the pressure increases by only a factor of 1.52. Here the locking is more readily observed using pressure band plots for ν equals 0.4 and 0.4999 (Fig. 5.4).

Next we consider eight-node elements. The eight-node displacement-based element locks with a pressure increase of a factor of 1200. The 8/4 element also locks with a pressure increase of a factor of 14. The 8/3 element also locks; the pressure increase is very slight (a factor of 1.52) but pressure band plots (Fig. 5.5) show the locking. We do not consider the 8/1 element because the constant pressure assumption implies that the element is unlikely to be effective.

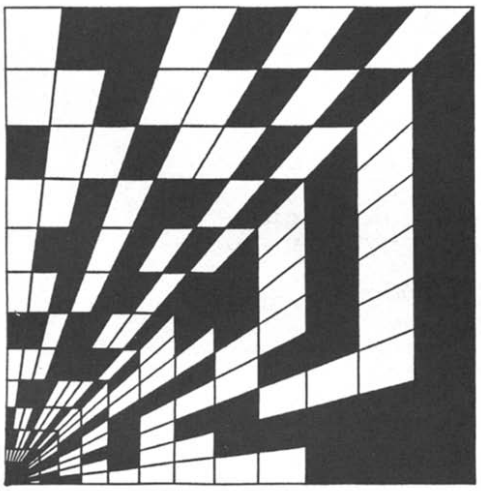

(a)

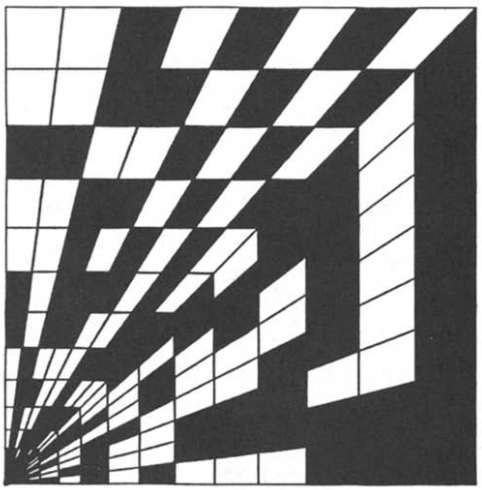

(b)

Fig. 5.4. Pressure band plots for 256 4/1 element mesh of square block, band width = 0.001. (a) $\nu = 0.4$. (b) $\nu = 0.4999$.

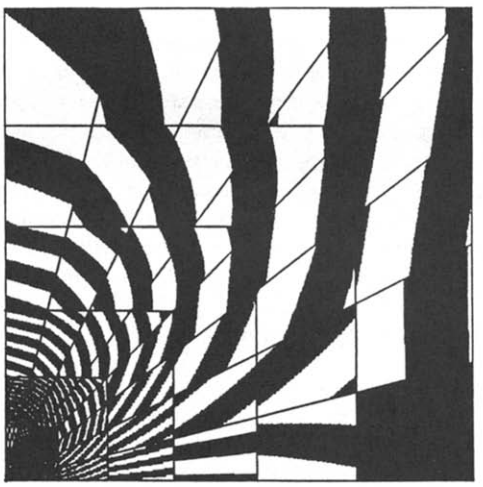

(a)

(b)

Fig. 5.5. Pressure band plots for 64 8/3 element mesh of square block, band width = 0.001. (a) $\nu = 0.4$. (b) $\nu = 0.4999$.

Now we consider nine-node elements. The nine-node displacement-based element locks with a pressure increase of a factor of 80. The 9/4 element also locks; the pressure increases by only a factor of 1.51, but pressure band plots (Fig. 5.6) show the locking. The 9/3 element exhibits a pressure increase of a factor of 1.5 and the pressure band plots (Fig 5.7) show that there is no locking. (Note that the analytical solution has a pressure increase of a factor of 1.5.)

The above results are supported by theoretical *a priori* analyses. Briefly, the pertinent theoretical

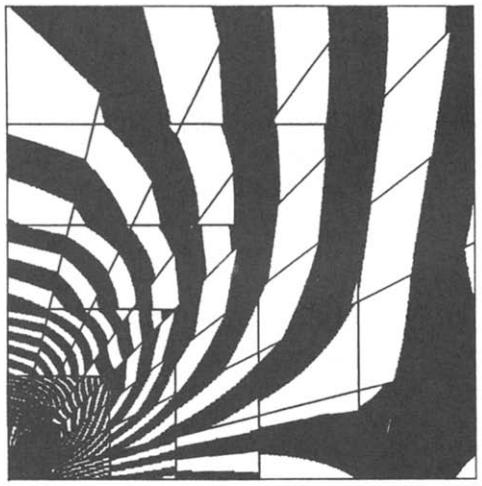

(a)

(b)

Fig. 5.6. Pressure band plots for 64 9/4 element mesh of square block, band width = 0.001. (a) $\nu = 0.4$. (b) $\nu = 0.4999$.

criterion used to determine element locking is the inf-sup condition of Brezzi and Babuška [12–14]

$$\inf_{q \in D_h} \sup_{\mathbf{v}_h \in V_h} \frac{\int_\Omega q \operatorname{div} \mathbf{v}_h \, d\Omega}{\|\mathbf{v}_h\| \, \|q\|} \geqslant \beta > 0, \qquad (5.5)$$

where V_h is the space of all displacement approximations, D_h is the space of all pressure approximations and β is a constant independent of the characteristic element size in the mesh. If this condition is satisfied, the element assemblage will not lock. The criterion (5.5) is equivalent to (and more easily used as)

$$\forall \mathbf{u} \in V, \quad \exists \, \mathbf{u}_I \in V_h$$

such that

$$\int_\Omega \operatorname{div}(\mathbf{u} - \mathbf{u}_I) q \, d\Omega = 0, \quad \forall q \in D_h, \qquad (5.6)$$

where V is the space of all displacement fields, $\mathbf{u}$ is the exact displacement solution and $\mathbf{u}_I$ is an interpolant. A more complete discussion of eqns (5.5) and (5.6) is given in [34]. Notice that the integrals are taken over the entire assemblage of elements.

It is well known that the 8/1 element and the 9/3 element satisfy the inf-sup condition [16, 34]. Because $\mathbf{u}_I$ can be constructed element-by-element, the condition (5.6) is satisfied for any assemblage of these elements. However, for other element types, it is very difficult to prove that (5.6) is not satisfied for a given assemblage. Therefore the solution behavior of elements for which the condition (5.6) cannot be proved beforehand must be predicted using numerical experiments. The most conservative approach is simply to use elements for which the inf-sup condition is always satisfied, and this is why the 9/3 element is a very attractive element.

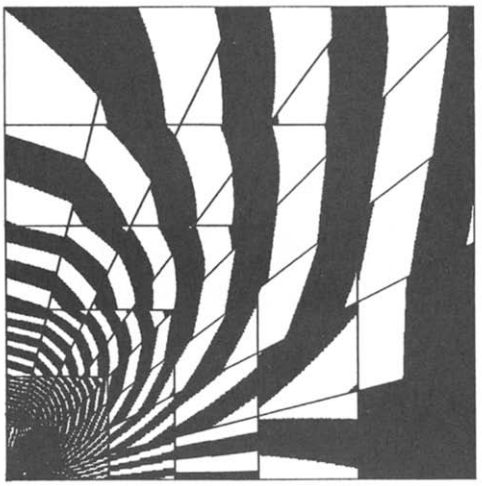

(a)

(b)

Fig. 5.7. Pressure band plots for 64 9/3 element mesh of square block, band width = 0.001. (a) $\nu = 0.4$. (b) $\nu = 0.4999$.

In three-dimensional analysis, the inf-sup condition shows that the 27/4 element, where

$$ {}^{t}\tilde{p} = {}^{t}p_1 + {}^{t}p_2 r + {}^{t}p_3 s + {}^{t}p_4 t \tag{5.7} $$

and r, s, t are the isoparametric coordinates, does not lock. However, this element can be quite expensive and it may be advantageous to develop more effective elements for three-dimensional analysis [35]. In the present paper, we only use the 27/4 element.

A cost comparison of the 9/3 and 27/4 elements with the corresponding displacement-based elements shows that the u/p elements are only slightly more expensive. The additional cost is mainly associated with the static condensation of the element stiffness matrices; this cost is low because the number of pressure variables per element is relatively small.

6. SAMPLE SOLUTIONS

We present, in this section, some examples that demonstrate the effective use of the u/p elements in compressible and almost incompressible analyses. The examples considered throughout this paper were run using the ADINA program [36] in which the u/p elements have been implemented. Unless otherwise specified, the following solution procedures are employed. Three by three Gauss integration is used to integrate the element stiffness matrices and force vectors in two-dimensional analysis and $3 \times 3 \times 3$ Gauss integration is used in three-dimensional analysis. For nonlinear analyses, simple load stepping is employed; for each load step, the prespecified load (or displacement) increment is applied and equilibrium iterations are used with the full Newton algorithm to re-establish equilibrium. Note that no special procedures, such as those described in [19, 22, 37], are used in the nonlinear analyses. Also no specific attention is given to the use of optimal meshes or optimal solution strategies.

6.1 *Isotropic linear elasticity—analysis of an axisymmetric pressure vessel*

The first example is the analysis of the axisymmetric pressure vessel already shown in Fig. 1.1. The

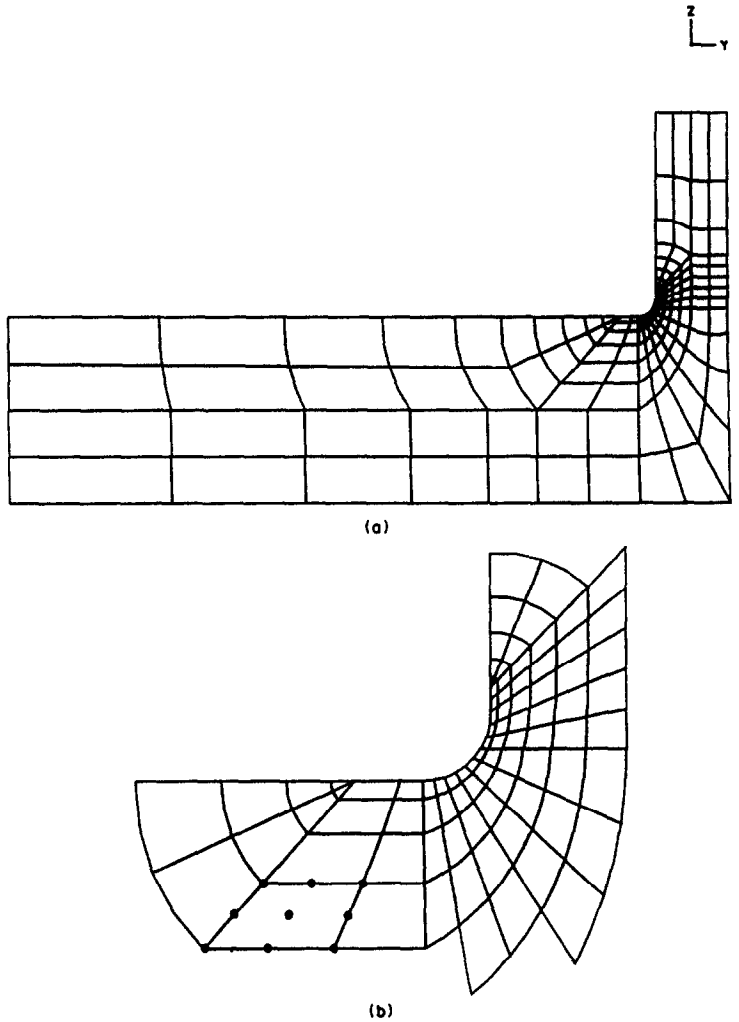

Fig. 6.1. One hundred and sixty 9/3 element mesh for axisymmetric pressure vessel. (a) Complete mesh. (b) Detail of mesh.

goal of the analysis is to determine the stress distribution due to the internal pressure loading, with special emphasis on the principal stresses on the 'line of stress output' shown in Fig. 1.1. The problem is to be solved assuming first a Poisson's ratio of 0.4 and then a Poisson's ratio of 0.49.

This problem was first considered in a paper by Floyd [38]. We presented some solutions for $\nu = 0.4$ [39], Brebbia *et al.* analyzed it using boundary elements [40] and we presented additional solutions using the u/p formulation [8]. Here we summarize the major results of the analysis discussed in [8].

We consider the 160 element mesh of 9/3 elements shown in Fig. 6.1. The solutions are compared with solutions from the 181 element mesh of eight-node displacement-based elements shown in Fig. 1.2. For $\nu = 0.4$, the pressure band and effective stress band plots are shown in Figs 6.2 and 1.3. (For brevity, we are showing only plots of the region near the stress concentration.) The two sets of plots agree quite well,

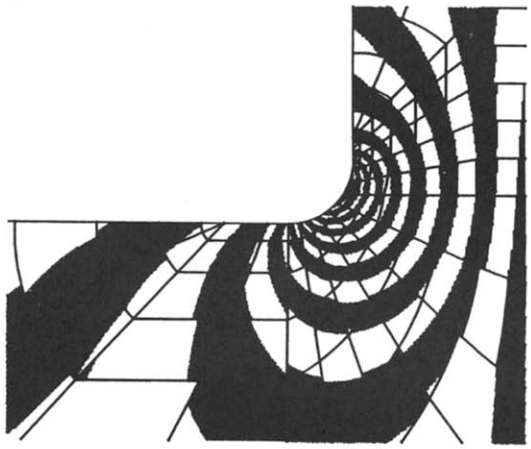

(a)

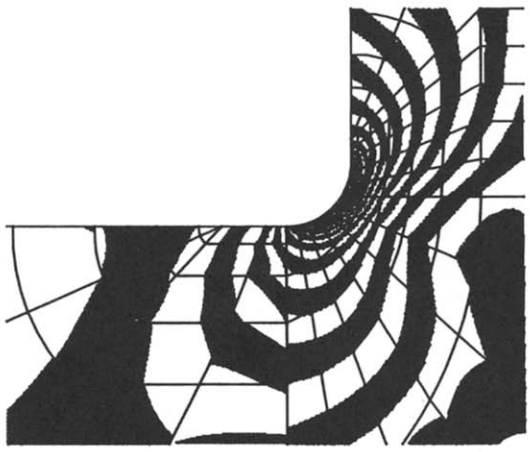

(b)

Fig. 6.2. Stress band plots for 160 9/3 element mesh, $\nu = 0.40$, band width = 2.5 psi. (a) Pressure band plot. (b) Effective stress band plot.

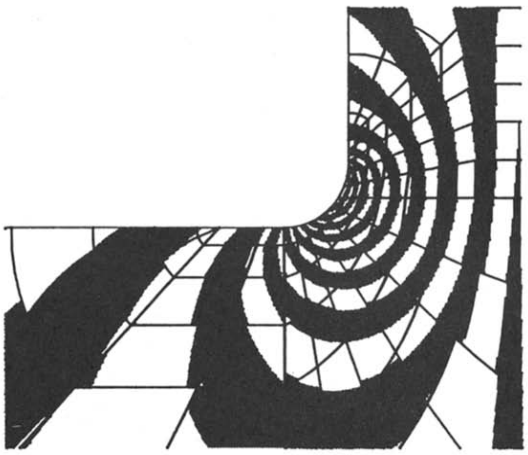

(a)

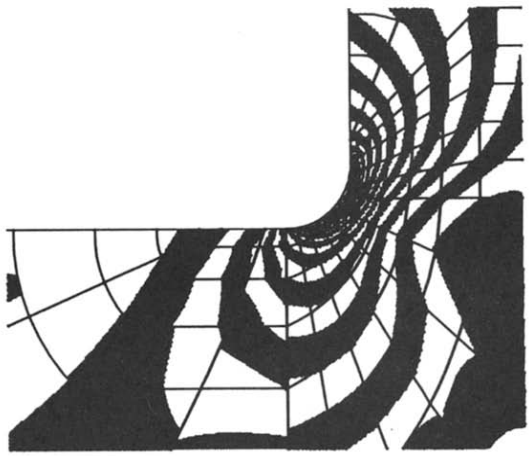

(b)

Fig. 6.3. Stress band plots for 160 9/3 element mesh, $\nu = 0.49$, band width = 2.5 psi. (a) Pressure band plot. (b) Effective stress band plot.

although the 181 element mesh pressure bands are somewhat wavy. For $\nu = 0.49$, the pressure band and effective stress band plots are shown in Figs 6.3 and 1.4. The 181 element mesh has locked; the pressure bands are totally indistinguishable, whereas the 160 element mesh pressure solution shows no degradation. Notice that the effective stress bands from both meshes agree quite well.

Graphs of the stresses along the line of stress output from the 160 element mesh solution corresponding to $\nu = 0.49$ are shown in Fig. 6.4. These results compare favorably with the boundary element results given by Floyd and Brebbia *et al.*

6.2 *Orthotropic linear elasticity—analysis of a cylinder under internal pressure*

We consider the axisymmetric analysis of an orthotropic cylinder under internal pressure loading

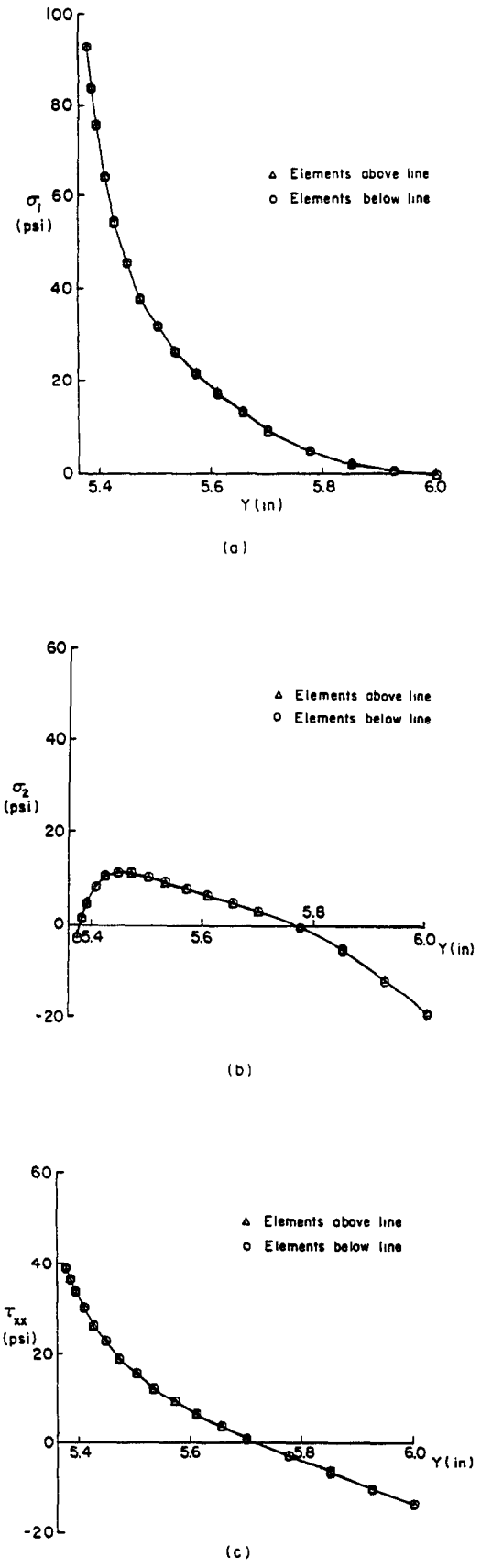

Fig. 6.4. Stress line graphs for 160 9/3 element mesh, $\nu = 0.49$. (a) Maximum in-plane principal stress. (b) Minimum in-plane principal stress. (c) Hoop stress.

(Fig. 6.5). The material constants for the cylinder are

$$E_r = 10^6 g \text{ MPa}, \quad E_\theta = 10^6 \text{ MPa}, \quad E_z = 10^6 \text{ MPa}$$

$$\nu_{r\theta} = \frac{0.25}{g}, \quad \nu_{\theta z} = 0.25, \quad \nu_{rz} = \frac{0.25}{g}$$

$$G_{rz} = 4 \times 10^5 \text{ MPa},$$

where r, θ, z denote the coordinate axes and g is a number used to control the degree of orthotropy. The cylinder may be thought of as being stiffened in the θ and z directions by the amount $1/g$. This set of material constants is specially chosen to produce a semideformable material when $g = 1/6$. To show that we deal with a semideformable material, we construct the inverse of the constitutive matrix

$$\bar{\mathbf{C}}^{-1} = \frac{1}{10^6 g}\begin{bmatrix} 1 & -0.25 & -0.25 \\ -0.25 & g & -0.25\,g \\ -0.25 & -0.25\,g & g \end{bmatrix}. \quad (6.1)$$

(We need to consider only the matrix associated with the normal stresses and strains.) Then we invert $\bar{\mathbf{C}}^{-1}$ to obtain

$$\bar{\mathbf{C}} = \frac{10^6}{\frac{15}{16}g - \frac{5}{32}}\begin{bmatrix} \frac{15}{16}g^2 & \frac{5}{16}g & \frac{5}{16}g \\ \frac{5}{16}g & g - \frac{1}{16} & \frac{1}{4}g + \frac{1}{16} \\ \frac{5}{16}g & \frac{1}{4}g + \frac{1}{16} & g - \frac{1}{16} \end{bmatrix} \quad (6.2)$$

and $\bar{\mathbf{C}}$ provides the pressure–strain relationship

$${}^t\bar{p} = -\frac{1}{3}\frac{10^6 g}{15g - 5/2}[(15g + 10)\,{}^te_{rr} + 25\,{}^te_{\theta\theta} + 25\,{}^te_{zz}] \quad (6.3)$$

and the 'bulk modulus'

$$\kappa = P({}^t\bar{p}) = \frac{1}{9}\frac{10^6 g}{15g - 5/2}(15g + 60). \quad (6.4)$$

The bulk modulus becomes infinite when g is decreased to 1/6. For $g = 1/6$, the pressure–strain relationship is

$${}^t\bar{p} = -\infty[\tfrac{1}{2}\,{}^te_{rr} + {}^te_{\theta\theta} + {}^te_{zz}] \quad (6.5)$$

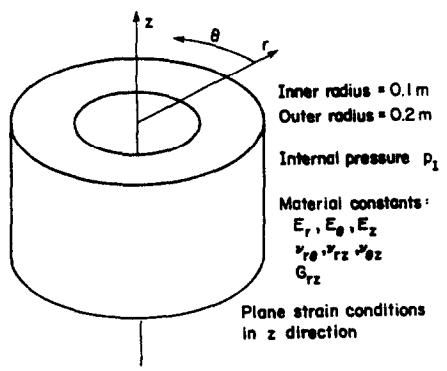

Fig. 6.5. Orthotropic cylinder under internal pressure.

so that the requirement that ${}^t\bar{p}$ be finite means that

$$\tfrac{1}{2}{}^te_{rr} + {}^te_{\theta\theta} + {}^te_{zz} = 0. \tag{6.6}$$

This constraint is analogous to the incompressibility constraint. However, as discussed in Sec. 3, this material is not incompressible, but is instead semi-deformable.

The analytical solution to the cylinder problem is [41]

$$\tau_{rr} = \frac{p_I c^{k+1}}{1-c^{2k}}\left(\frac{r}{b}\right)^{k-1} - \frac{p_I}{1-c^{2k}}c^{k+1}\left(\frac{r}{b}\right)^{-k-1} \tag{6.7a}$$

$$\tau_{\theta\theta} = \frac{p_I c^{k+1}}{1-c^{2k}}k\left(\frac{r}{b}\right)^{k-1} + \frac{p_I}{1-c^{2k}}kc^{k+1}\left(\frac{r}{b}\right)^{-k-1} \tag{6.7b}$$

$$\tau_{zz} = \nu_{rz}\tau_{rr} + \nu_{\theta z}\tau_{\theta\theta}, \tag{6.7c}$$

where p_I is the applied internal pressure, a is the internal radius, b is the external radius, $c = a/b$, r is the radial coordinate and

$$k = \sqrt{\frac{(1-\nu_{rz}\nu_{zr})E_\theta}{(1-\nu_{\theta z}\nu_{z\theta})E_r}}. \tag{6.7d}$$

Our four element finite element mesh is shown in Fig. 6.6. Table 6.1 shows the root-mean-square pressure (defined in eqn (5.4)) for different values of g when 9-node and 9/3 elements are used. The displacement-based element mesh locks, with the root-mean-square pressure increasing by a factor of 260, whereas the u/p element mesh does not lock. Figure 6.7 shows stress graphs from the 9/3 element mesh solution for $g = 0.16666667$. These graphs compare very well with the analytical solution (using $g = 1/6$) discussed above.

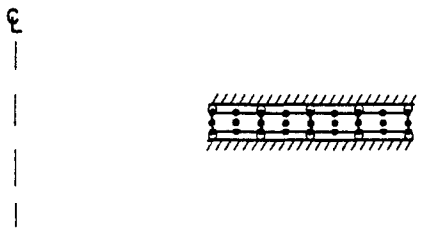

Fig. 6.6. Four 9/3 element mesh for orthotropic cylinder.

Table 6.1. Root-mean-square pressure vs g for orthotropic cylinder problem

g	P_{rms} (disp–based)	P_{rms} (u/p)
1	27.78	27.78
0.5	25.53	25.51
0.2	21.28	19.38
0.17	85.39	17.77
0.167	754.7	17.59
0.1667	3919	17.57
0.16667	6752	17.56
0.166667	7281	17.57
0.1666667	7338	17.57
0.16666667	7343	17.57

6.3 *Rubber-like elasticity (using the total Lagrangian formulation)*

6.3.1 *Rubber cylinder drawn through a die.* A rubber cylinder is pulled through a frictionless die that reduces the diameter of the cylinder from 2 in. to 1 in. (see Fig. 6.8). A neo-Hookean material description is used to model the rubber, with $C_1 = 100$ psi and $\kappa = 10^6$ psi. The goal of the analysis is to determine the steady-state drawing force.

The analytical solution for this problem, assuming total incompressibility, is easily derived assuming that the deformation of the drawn rubber is homogeneous. The drawing force can be computed either by use of the principle of virtual work or by integrating the stress field from the known displacements:

$$R = C_1\left[2\left(\frac{r_2}{r_1}\right)^2 + \left(\frac{r_1}{r_2}\right)^4 - 3\right](\pi r_2^2), \tag{6.8}$$

where r_1 is the original radius and r_2 is the final radius of the rubber. For the given geometric and material data, $R = 1060$ lb.

To solve this problem, we use the mesh of 50 9/3 elements shown in Fig. 6.9. Also shown is the target surface that represents the frictionless die. For the contact conditions the algorithm available in ADINA is used [42]. A prescribed displacement is applied to the elements on the left side of the mesh. The adjacent diagonal elements are used only to help draw the cylinder of rectangular elements on the right side of the mesh into the die. Some important modeling considerations are that the die taper must be gradual and that enough elements must be used in the axial (horizontal) direction; otherwise the contact algorithm will show convergence difficulties as the rubber is drawn into the die.

A prescribed displacement of 10 in. is applied to the left side of the mesh in 100 equal load steps. Some plots of the deformed configuration, in which only the rectangular elements are shown for clarity, are shown in Fig. 6.10. We see that the elements are undergoing large displacements and strains. A force–deflection curve is given in Fig. 6.11. Below a displacement of 7 in., the diagonal elements are being pulled through the neck of the die. After this displacement is reached, a few rectangular elements have been pulled through the die and the steady-state load is quite close to the analytical solution.

6.3.2 *Rubber cylinder pressed between two plates.* A problem of practical engineering importance is the determination of stresses within a toroidal rubber ring that is pressed between two plates [43]. For the purpose of analysis, this problem can be idealized as a plane strain rubber cylinder pressed between two frictionless plates, see Fig. 6.12. We would like to determine the force–deflection curve for the cylinder

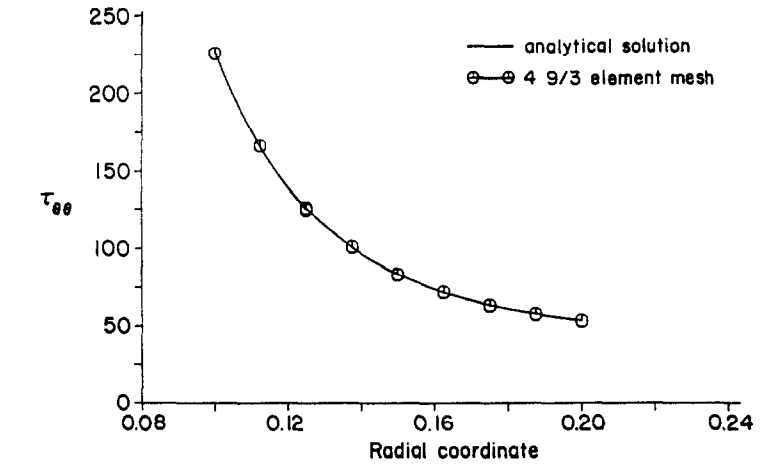

(a)

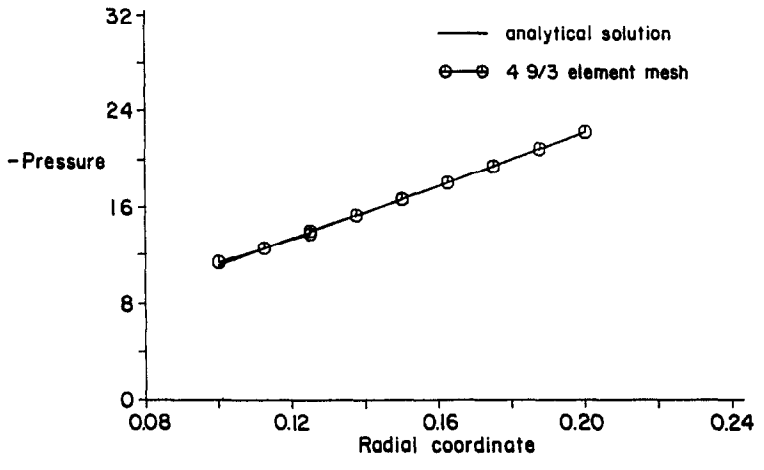

(b)

Fig. 6.7. Stress line graphs for orthotropic cylinder. (a) Hoop stress. (b) Pressure.

and also the location and magnitude of the maximum stresses when the applied displacement equals one-half of the initial diameter of the cylinder.

For small displacements, the Hertz contact assumptions are valid and the following force–deflection relationship results [44]:

$$\Delta = \frac{4R(1-\nu^2)}{\pi E}\left(\frac{1}{3} + \ln\frac{2D}{b}\right), \tag{6.9}$$

where R is the load per unit thickness, D is the cylinder diameter, b is the contact zone width

$$b = 1.60\sqrt{RD\left(\frac{1-\nu^2}{E}\right)} \tag{6.10}$$

and E, ν are the small strain Young's modulus and Poisson's ratio. For larger displacements, an approx-

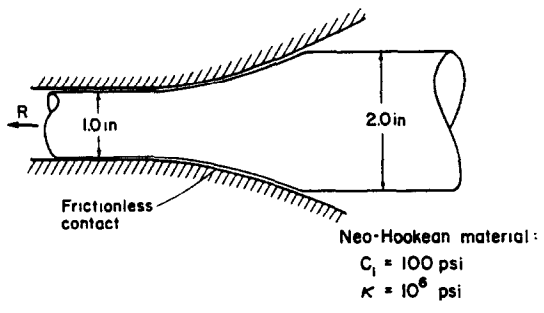

Fig. 6.8. Rubber cylinder drawn through a die.

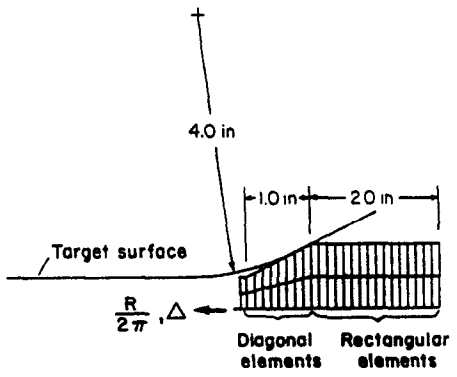

Fig. 6.9. Fifty 9/3 element mesh for rubber cylinder.

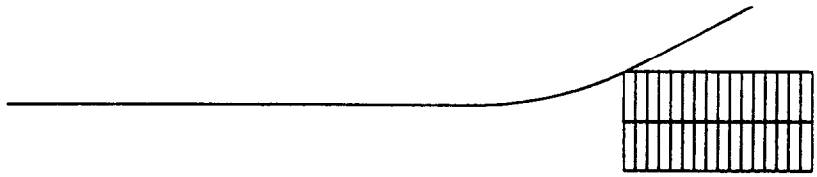

(a)

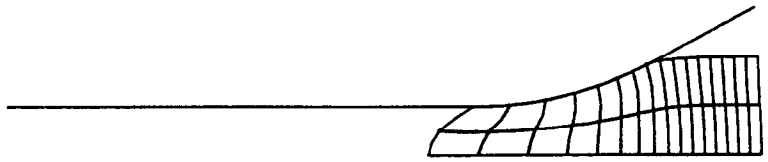

(b)

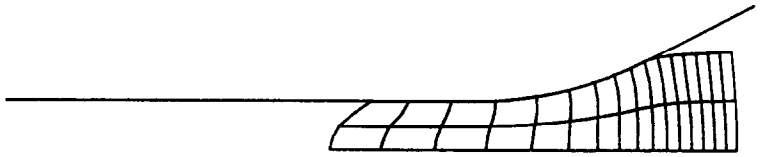

(c)

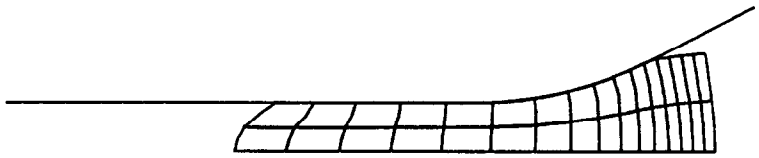

(d)

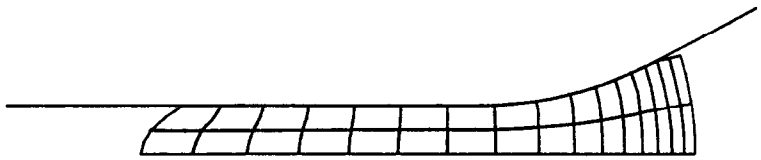

(e)

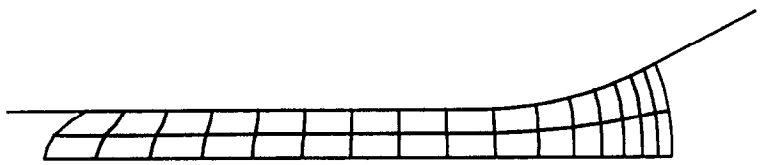

(f)

Fig. 6.10. Deformations of rubber cylinder, plotting only the initially rectangular elements. (a) $\Delta = 0$ in. (b) $\Delta = 6$ in. (c) $\Delta = 7$ in. (d) $\Delta = 8$ in. (e) $\Delta = 9$ in. (f) $\Delta = 10$ in.

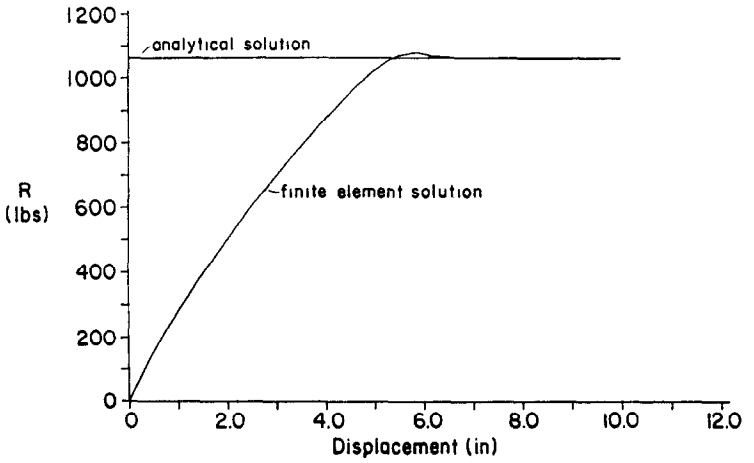

Fig. 6.11. Force–deflection curve for rubber cylinder.

imate solution based on experimental data is [43]:

$$R = ED\left[1.25\left(\frac{\Delta}{D}\right)^{3/2} + 50\left(\frac{\Delta}{D}\right)^{6}\right]. \qquad (6.11)$$

In this relationship, it is assumed that the Young's modulus is constant.

We idealize the rubber using a Mooney–Rivlin description, with $C_1 = 0.293$ MPa, $C_2 = 0.177$ MPa and $\kappa = 1410$ MPa. For small strains, the Young's modulus is $E = 2.82$ MPa and the bulk modulus to shear modulus ratio is 1,500.

Two finite element meshes of 9/3 elements are used, one with 16 elements and the other with 64 elements (Fig. 6.13). The ADINA contact algorithm is used in conjunction with a rigid frictionless target surface. The load is applied by prescribing the displacements at the top of the mesh.

First we consider small displacements. A displacement of $\Delta = 0.02$ m is applied in ten equal load steps (using the total Lagrangian formulation). The results are shown in Fig. 6.14(a). We see that the Hertz and Lindley solutions do not agree for this range of displacements. Below $\Delta = 0.01$ m, only one node in the 16 element mesh is in contact and this makes the force–deflection curve for this mesh artificially soft. After the next node comes into contact, the stiffness of the mesh noticeably increases. The 64 element mesh is in close agreement with the Hertz solution, although the difference between these solutions increases as the deflection is increased.

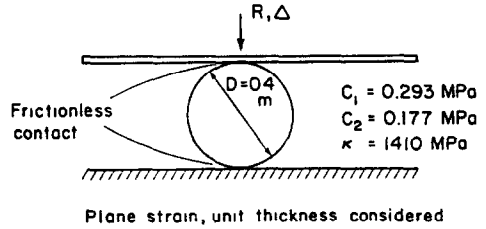

Fig. 6.12. Rubber cylinder pressed between two plates.

For the large displacement solution, a displacement of $\Delta = 0.2$ m is applied in ten equal load steps. The resulting force–deflection curves are shown in Fig. 6.14(b). For this range of deflection, the two finite element solutions are in close agreement. The Hertz solution is too soft (it is not intended to be used for large displacements). The Lindley solution is also softer than the finite element solutions, but it predicts the rapid stiffening of the cylinder as $\Delta = 0.2$ m is approached. The differences between the Lindley and finite element solutions are probably largely due to the assumption of a constant Young's modulus in the Lindley solution.

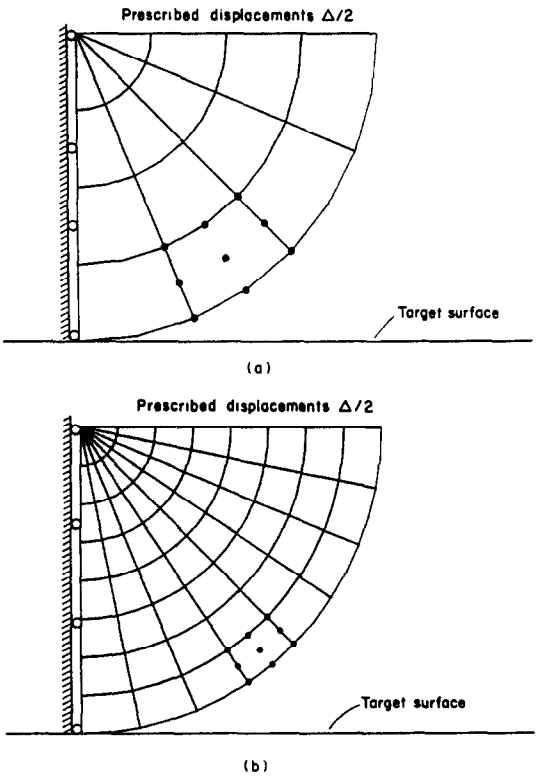

Fig. 6.13. Meshes used for rubber cylinder. (a) 16 9/3 elements. (b) 64 9/3 elements.

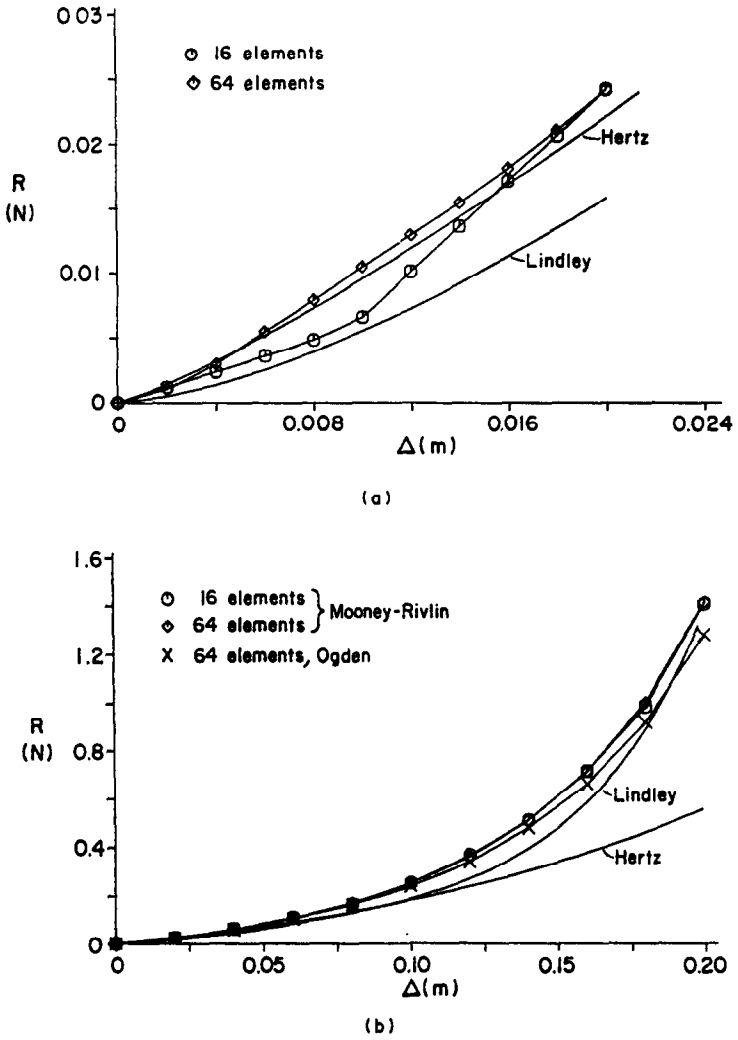

Fig. 6.14. Force–deflection curves for rubber cylinder. (a) Small displacement analysis. (b) Large displacement analysis.

The deformed 64 element mesh for $\Delta = 0.2$ m is given in Fig. 6.15. The deformed shape agrees with a photograph by Göbel [45] (Fig. 6.16). Stress band plots for $\Delta = 0.2$ m using the 64 element mesh are shown in Fig. 6.17. The stress bands are continuous, indicating that the mesh is adequate. The locations and magnitudes of the largest stresses are also indicated.

Also shown in Fig. 6.14(b) is a force–deflection curve obtained using the Ogden material description with the following coefficients:

$$\mu_1 = 0.746 \text{ MPa} \qquad \mu_2 = -0.306 \text{ MPa}$$

$$\mu_3 = 6.609 \times 10^{-5} \text{ MPa}$$

$$\alpha_1 = 1.748 \qquad \alpha_2 = -1.656$$

$$\alpha_3 = 7.671$$

These coefficients were chosen to fit the same experimental data as were the Mooney–Rivlin coefficients [22]. We see that the force–deflection curve obtained using the Ogden model is close to the curve obtained using the Mooney–Rivlin model.

6.3.3 *Symmetric bifurcations of a rubber cylinder.* The solid cylinder shown in Fig. 6.18 is subjected to a uniform compression. The cylinder consists of a neo-Hookean material and its deformations are constrained to be axisymmetric. As long as the compressive force is less than a critical load, the deformations are homogeneous. However, once the critical load is reached, axisymmetric bifurcations are possible (Fig. 6.19).

Wilkes [46] analyzed this problem using analytical techniques and the results are plotted in Fig.

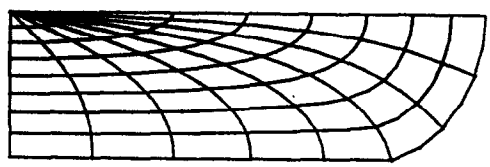

Fig. 6.15. Deformed 64 9/3 element mesh of rubber cylinder, $\Delta = 0.2$ m.

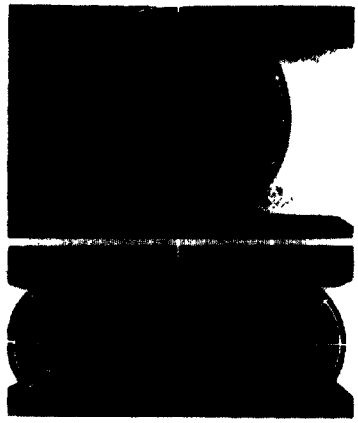

Fig. 6.16. Photograph of rubber cylinder pressed between two plates; from [45, Fig. 3.20].

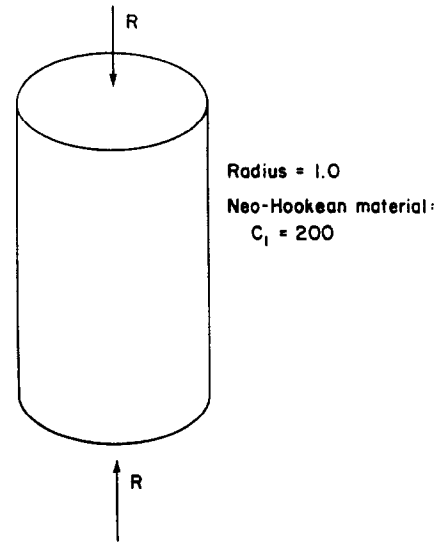

Fig. 6.18. Rubber cylinder in uniaxial compression.

6.20. The largest stretch at which a bifurcation occurs corresponds to a wavelength ratio of 0.76; the load corresponding to this stretch is the critical load.† For loads larger than the critical load, bifurcations with other wavelengths are possible. In all cases, the shape of the bifurcation is a sinusoidal wrinkling of the surface of the cylinder.

Miller [47] analyzed this problem using a mixed formulation finite element method, and obtained physically realistic results only with an eight-node element with three discontinuous pressure variables. His mesh was constructed to model one bifurcation wavelength. We analyze this problem using the general mesh layout shown in Fig. 6.21. A large height to radius ratio (10 : 1) is used to allow the mesh to contain possible bifurcations with very long wavelengths and to show that the obtained bifurcations are periodic.

The general method of solution is to increase the load level until the tangent stiffness matrix contains a negative eigenvalue. Then a separate linearized buckling analysis with the algorithm available in ADINA is performed using two configurations with loads close to the critical load of the model. The linearized buckling analysis produces estimates of the analytical critical load and associated bifurcation.

Our first mesh contains 90 9/3 elements. The first three bifurcations along with the associated estimates of the analytical critical load and wavelength

† Wilkes obtains a wavelength ratio of 0.47 at a critical axial stretch of 0.446; however his estimate was obtained using asymptotic expansions of the Bessel functions whereas our estimate, using his equations, is obtained using Taylor series expansions of the Bessel functions.

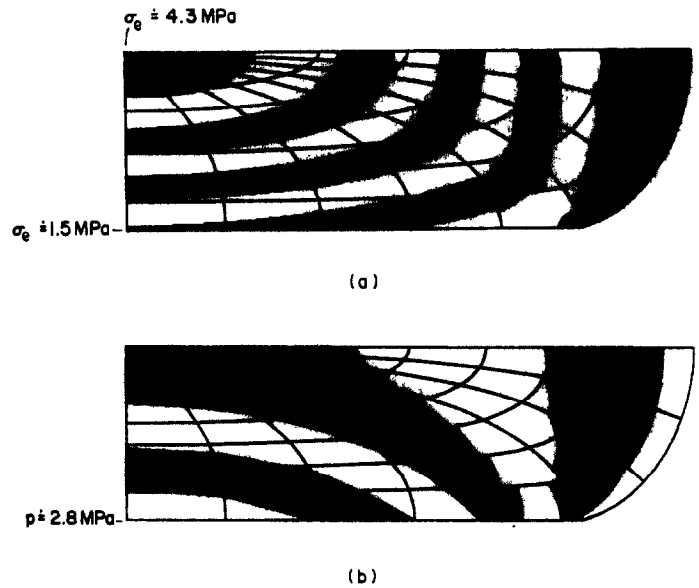

Fig. 6.17. Stress band plots for 64 9/3 element mesh, $\Delta = 0.2$ m, band width = 0.5 MPa. (a) Effective stress band plot. (b) Pressure band plot.

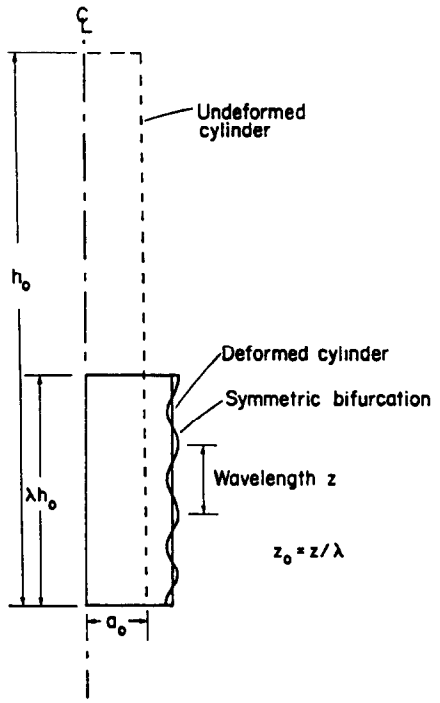

Fig. 6.19. Symmetric bifurcations of rubber cylinder.

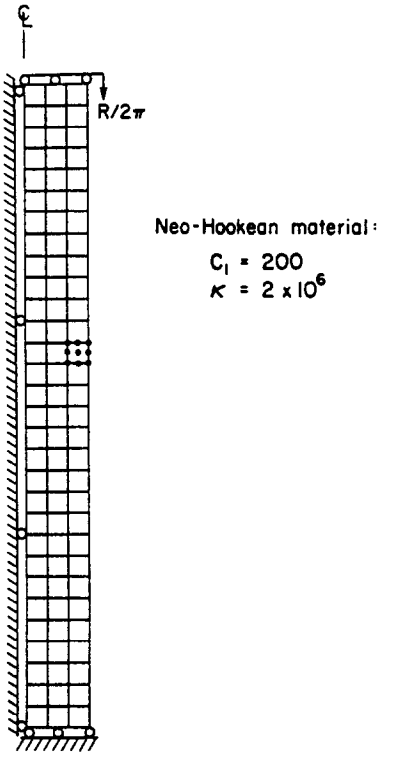

Fig. 6.21. Ninety 9/3 element mesh for rubber cylinder.

are given in Fig. 6.22. The estimates of the critical load are almost identical and are about 16% larger than the analytical solution of Wilkes. However, the three predicted wavelengths from the finite element solutions are much larger than the analytical value.

Next we divide each element in the mesh into four smaller elements to produce a 360 element mesh of 9/3 elements. The first three bifurcations and associated estimates of the analytical critical load are shown in Fig. 6.23. The estimates of the critical load are now only 4% larger than the analytical solution. However, the smallest predicted wavelength is still about twice as large as the analytical value.

These wavelength predictions from the two meshes can be explained as follows. Both meshes overestimate the critical buckling load; therefore both meshes underestimate the critical axial stretch. Using the axial stretches corresponding to the smallest predicted buckling loads and Fig. 6.20, we find that the corresponding bifurcation wavelengths are also too large; they are 2.60 and 1.75 for the 90 and 360 element meshes respectively. The large difference between these values and the value of 0.76 is clearly due to the fact that the curve in Fig. 6.20 is almost horizontal in the region of $z_o/a_o = 0.76$. Hence the convergence to the analytical value of the critical wavelength, as a function of the number of elements used, must be expected to be very slow.

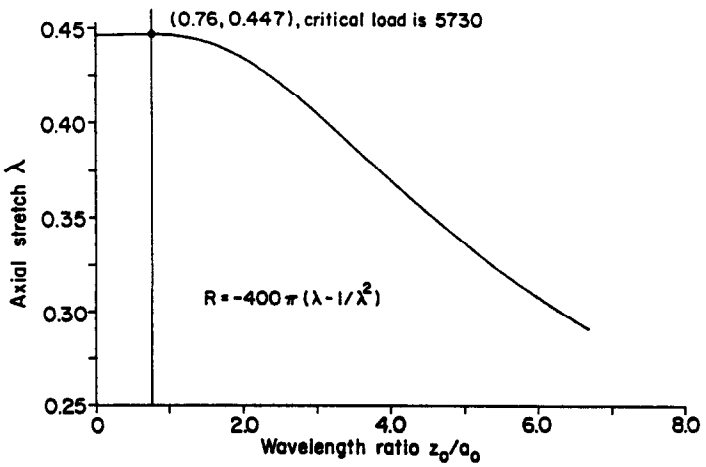

Fig. 6.20. Critical stretch vs wavelength ratio for rubber cylinder, analytical solution.

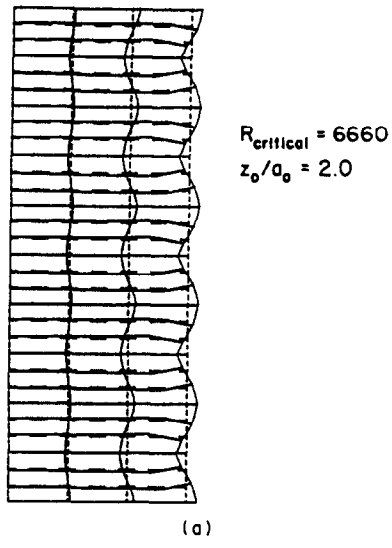

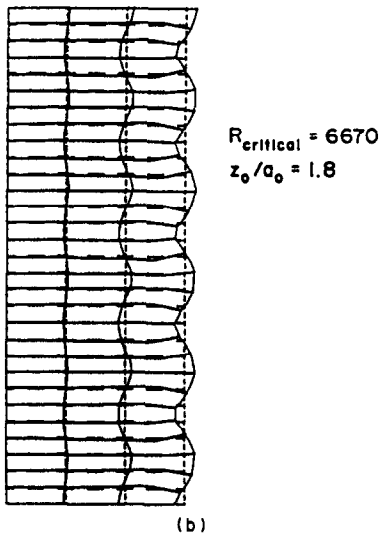

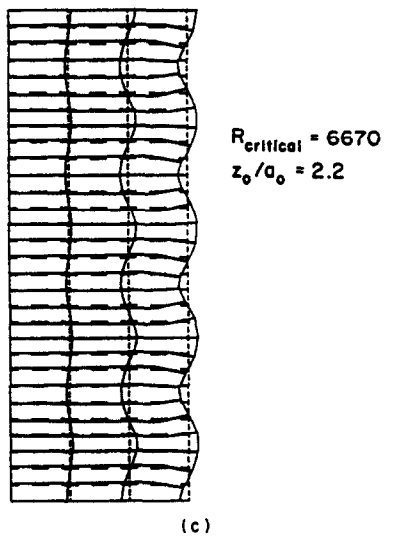

Fig. 6.22. Bifurcations of 90 9/3 element mesh; $'*R/2\pi$ = 1050; $'^1R/2\pi$ = 1060. (a) First bifurcation. (b) Second bifurcation. (c) Third bifurcation.

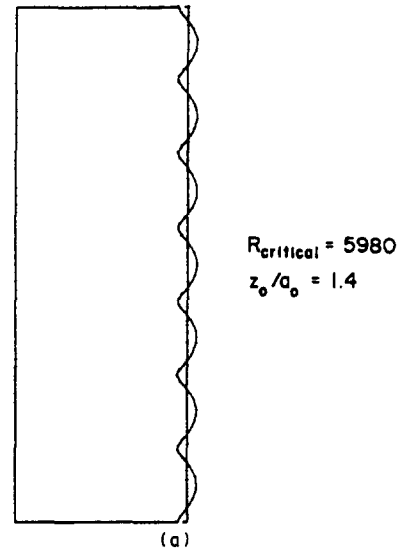

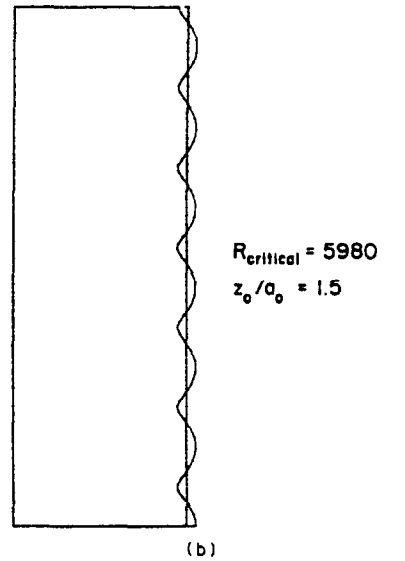

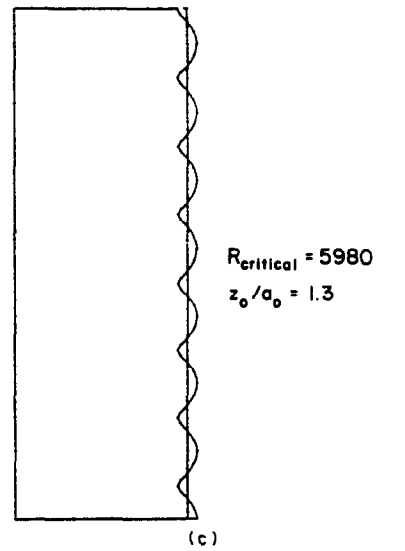

Fig. 6.23. Bifurcations of 360 9/3 element mesh; only mesh outline shown; $'*R/2\pi$ = 950; $'^1R/2\pi$ = 960. (a) First bifurcation. (b) Second bifurcation. (c) Third bifurcation.

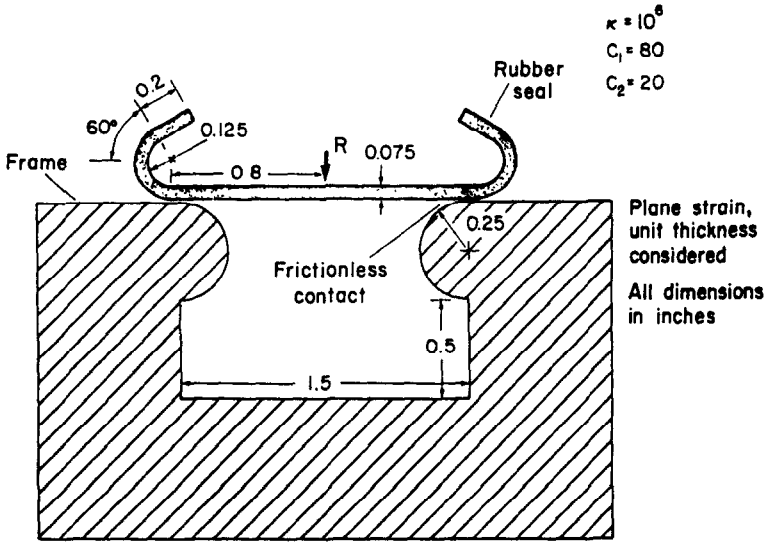

Fig. 6.24. Insertion of a rubber seal.

6.3.4 *Insertion of a rubber seal.* Figure 6.24 shows a highly idealized rubber seal and its frame. As shown, the seal is to be pushed into the frame by the force R. We would like to determine the force required to insert the seal and also the deformed shape of the seal and the contact forces between the seal and frame after insertion. No analytical or experimental results are available for this problem.

We use the mesh of 39 9/3 elements shown in Fig. 6.25. The mesh is constructed to have enough contact segments (two per element) to adequately model the contact between the seal and the curved section of the frame. The mesh is inserted by prescribing the displacement on the top of the truss element. Fifty equal load steps are used to apply the final displacement of one inch. Once this displacement is reached, the truss is removed (using the element birth/death option in ADINA) and one more load step is performed to determine the final equilibrium state and the contact forces.

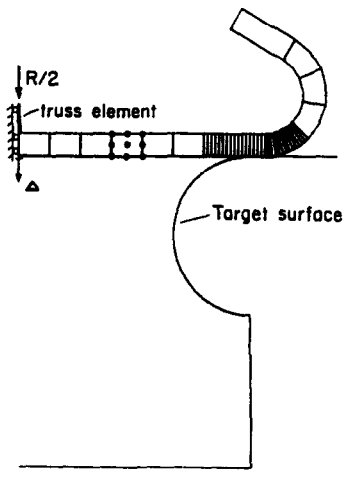

Fig. 6.25. Thirty-nine 9/3 element mesh for rubber seal.

Some of the intermediate mesh configurations are shown in Fig. 6.26. Notice that the contact area always lies within the refined region of the mesh. The force–deflection curve is shown in Fig. 6.27. The abrupt change in slope at a displacement of roughly 0.8 in. is due to the region of contact moving to elements with slightly longer contact segments. The contact forces acting on the inserted seal are depicted in Fig. 6.28.

6.3.5 *Stress analysis of a rubber bushing.* Figure 6.29 shows the cross-section of a rubber bushing. The frame and internal shaft are assumed to be rigid and it is assumed that the rubber is perfectly bonded to these components. The goal of the analysis is to determine the force–deflection curve of the unit and also the stresses and deformations corresponding to a displacement of 3 mm.

For small displacements, an approximate value of the bushing stiffness is [48]:

$$k = \beta G, \tag{6.12}$$

where β is equal to 135 for a long bushing with the given dimensions and G is the shear modulus. From the given data, $k = 60$ N/mm. For large displacements we can compare our solutions with those obtained by Zdunek and Bercovier [25], who also analyzed this problem with their mixed finite element formulation.

To solve this problem, we choose the 72 4/1 element mesh used by Zdunek and Bercovier (Fig. 6.30(a))†. A mesh of 32 9/3 elements (Fig. 6.30(b)) is used to compare the effectiveness of the 9/3 element with the 4/1 element. Also considered are refinements of these meshes obtained by dividing each element into four smaller elements: a 288 4/1 element mesh and a 128 9/3 element mesh.

† Two by two Gauss integration is used for the 4/1 elements.

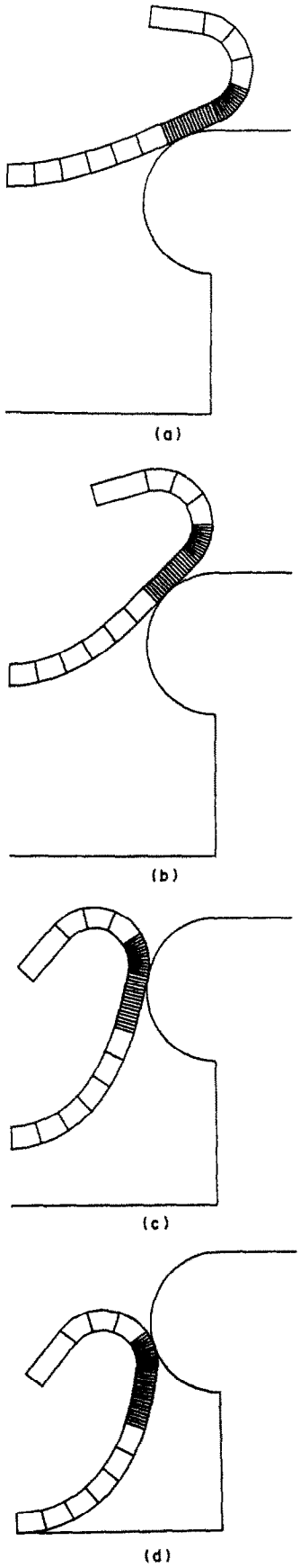

Fig. 6.26. Deformations of rubber seal. (a) $\Delta = 0.2$ in. (b) $\Delta = 0.4$ in. (c) $\Delta = 0.8$ in. (d) $\Delta = 1.0$ in.

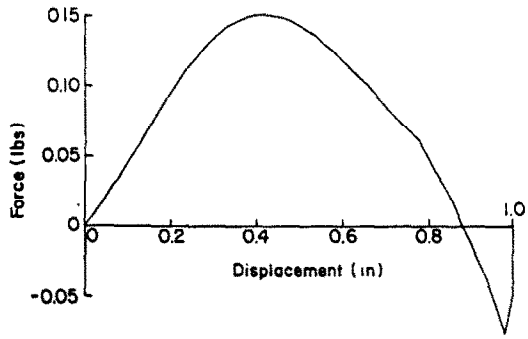

Fig. 6.27. Force–deflection curve for rubber seal.

The force–deflection curves given in Fig. 6.31 show the results obtained by specifying a displacement increment of 1 mm in each load step. All of the solutions agree with each other up to a displacement of about 4 mm; above this displacement, the 72 4/1 element mesh becomes highly distorted and stiffens excessively. The 72 4/1 element mesh force–deflection curve agrees with the corresponding curve shown in [25] over the displacement range considered in that paper (0–4.8 mm). We note that the bushing response is almost linear.

We now examine the displacements and stresses for an applied displacement of 3.0 mm. Figure 6.32 shows pressure band plots. The deformations of the 72 4/1 element mesh agree with the solution given in [25]. However, we cannot directly compare the pressures with the results in [25] because the pressure contour plot in [25] utilizes smoothed data. (Also, the pressure constraint equation used in Zdunek and Bercovier's analysis was different from the one used in our analysis [49].) We see that the 9/3 mesh stress solutions are smoother than the 4/1 mesh solutions.

6.3.6 *Torsion of a rubber cylinder.* In this example, we consider a simple three-dimensional problem. The solid rubber cylinder shown in Fig. 6.33 is constrained in the axial direction and is twisted by the applied moment. We would like to determine the moment–rotation curve and the axial force–rotation curve for the cylinder.

This problem was solved analytically by Rivlin, assuming total incompressibility. The solutions are [50]:

$$M = \pi(C_1 + C_2)r^4(\theta/L) \tag{6.13}$$

$$N = \frac{\pi}{2}(C_1 + 2C_2)r^4(\theta/L)^2, \tag{6.14}$$

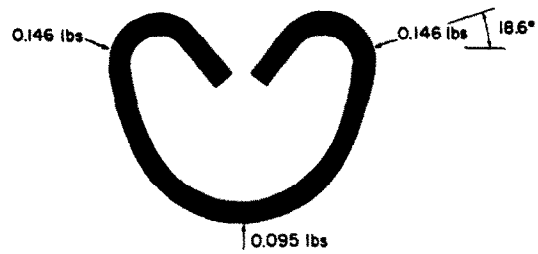

Fig. 6.28. Contact forces acting on rubber seal, $\Delta = 1.0$ in.

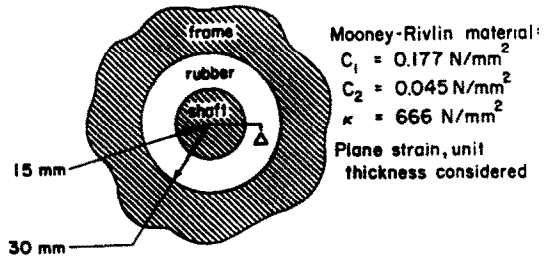

Fig. 6.29. Rubber bushing.

where M is the applied moment, N is the axial force (positive in compression), r is the cylinder radius, L is the cylinder length and θ is the total angular displacement. (In this problem, the cylinder radius does not change as the cylinder is twisted because of the incompressibility constraint.)

We use the mesh layout of eight collapsed 27-node elements shown in Fig. 6.34 to model the cylinder. We consider both displacement-based and 27/4 elements. On the far end of the cylinder, all of the nodes are fixed. On the near end, the angular displacement of the center node is prescribed and rigid links placed between this node and the other nodes on the near end cause the entire cross-section to rotate by this amount. A stiff truss element is connected to the center node and ground; this element constrains the cylinder in the axial direction and is used to measure the axial reaction force.

We apply a total angular displacement of 0.1 rad in ten equal load steps. The moment–rotation curves are shown in Fig. 6.35, where we see that the two finite element solutions agree very well with the analytical solution. The axial force–rotation curves are shown in Fig. 6.36. Here the 27/4 element solution agrees with the analytical solution but the displacement-based element solution stiffens excessively as the rotation is increased. Notice that the displacements of the mesh are still quite small at a rotation of 0.1 rad.

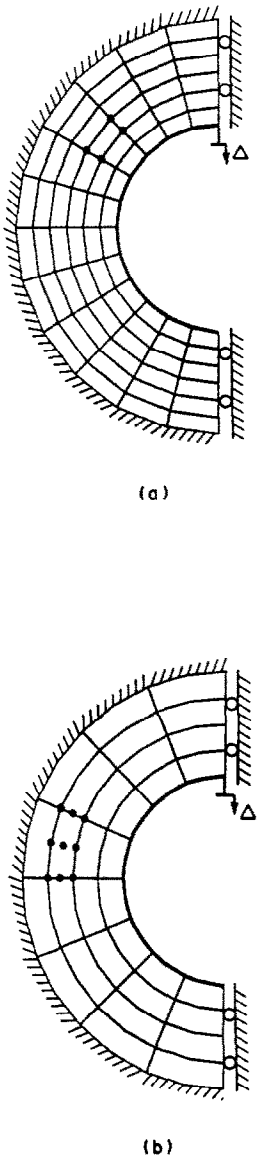

Fig. 6.30. Meshes used for rubber bushing. (a) 72 4/1 element mesh. (b) 32 9/3 element mesh.

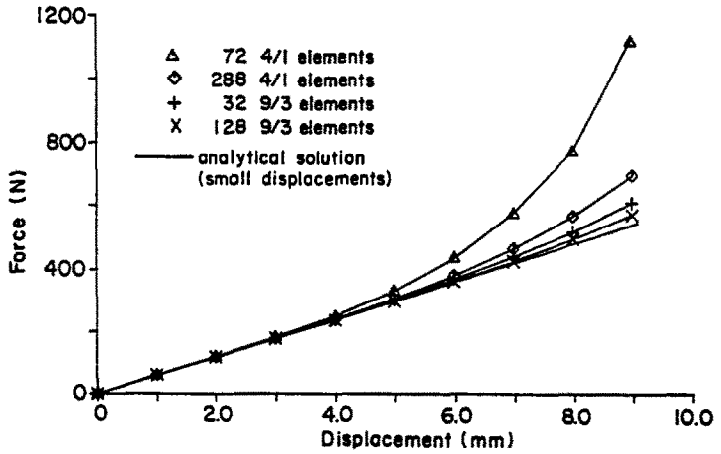

Fig. 6.31. Force–deflection curves for rubber bushing.

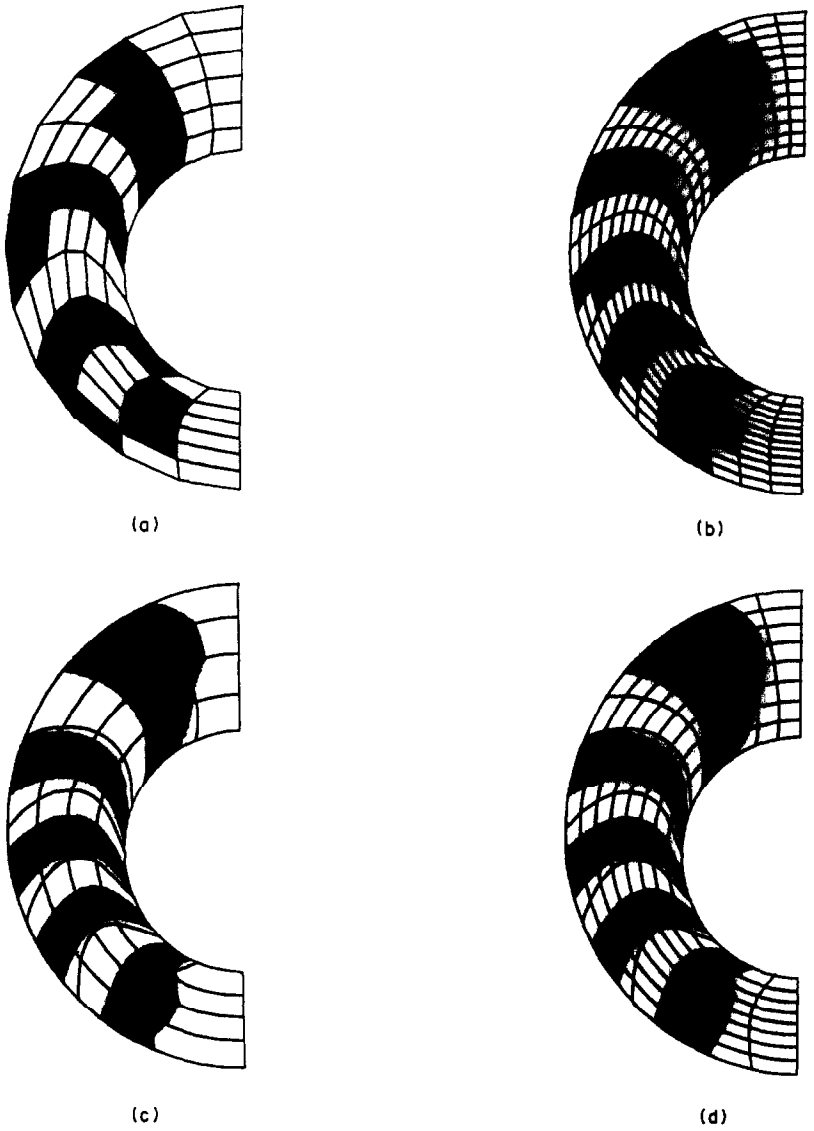

Fig. 6.32. Pressure band plots for rubber bushing, $\Delta = 3.0$ mm, band width = 0.5 N/mm^2. (a) 72 4/1 element mesh. (b) 288 4/1 element mesh. (c) 32 9/3 element mesh. (d) 128 9/3 element mesh.

6.4 *Elasto-plasticity (using the materially–nonlinear-only formulation)*

6.4.1 *Bending of a beam.* A simple verification problem is to determine the limit load of a thick beam with rectangular cross-section when subjected to a moment (Fig. 6.37). The analytical limit load is

$$M_L = \frac{2}{\sqrt{3}} \sigma_y \left(\frac{h}{2}\right)^2, \tag{6.15}$$

where M_L is the limit moment (per unit thickness), σ_y is the yield stress in uniaxial tension and h is the cross-sectional height. Substituting the geometric and material data gives $M_L = 30{,}020$.

To solve this problem, we use the mesh of five distorted nine-node elements shown in Fig. 6.38. We use distorted elements to show the robustness of the u/p elements; for the solution to be accurate using only a few displacement-based elements, the elements must be undistorted [51]. An angular displacement of 0.005 radians is applied using constraint equations in ten load steps. The moment–rotation curves for a mesh of five 9-node displacement-based elements and a mesh of five 9/3

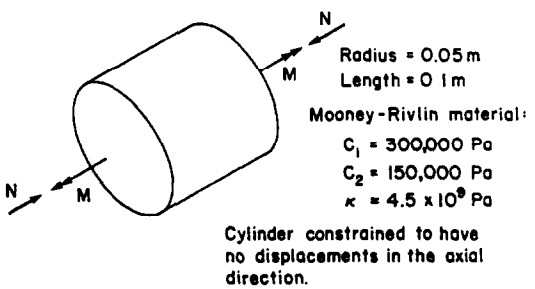

Fig. 6.33. Torsion of a rubber cylinder.

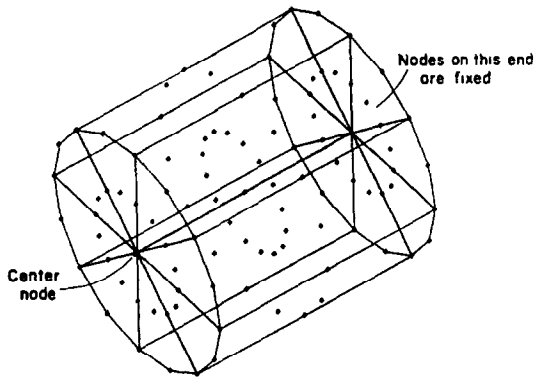

Fig. 6.34. Eight collapsed 27/4 element mesh for rubber cylinder.

elements are given in Fig. 6.39. The slope of the displacement-based element curve does not tend to zero as the rotation is applied but instead attains a finite value of $dM/d\theta = 80{,}000$. In contrast, the slope of the 9/3 element curve is almost zero at the correct limit load.

6.4.2 *Indentation of an elastic–perfectly plastic half-space by a smooth punch.* A well-known problem is the determination of the limit load of a smooth rigid punch pressed into an elastic–perfectly plastic half-space (Fig. 6.40). For a rigid–perfectly plastic material, considering only material nonlinearities, the limit load is [52]:

$$R = (2 + \pi)(b)(\sigma_y/\sqrt{3}), \tag{6.16}$$

where R is the load per unit thickness and b is the punch width. For the geometric and material data given, $R = 154{,}000$ lb.

Our basic mesh layout is shown in Fig. 6.41(a). The 10 nine-node element mesh shown is subdivided once to obtain a 40 element mesh and twice to obtain a 160 element mesh. We consider both 9-node displacement-based elements and 9/3 elements. Note that the meshes have collapsed elements at the punch corner and that all of the element nodes on the collapsed element sides have the same degrees of freedom. The loading and boundary conditions associated with the punch are shown in Fig. 6.41(b). These boundary conditions are consistent with the assumption of only material nonlinearities; in a geometrically nonlinear analysis, it is necessary to

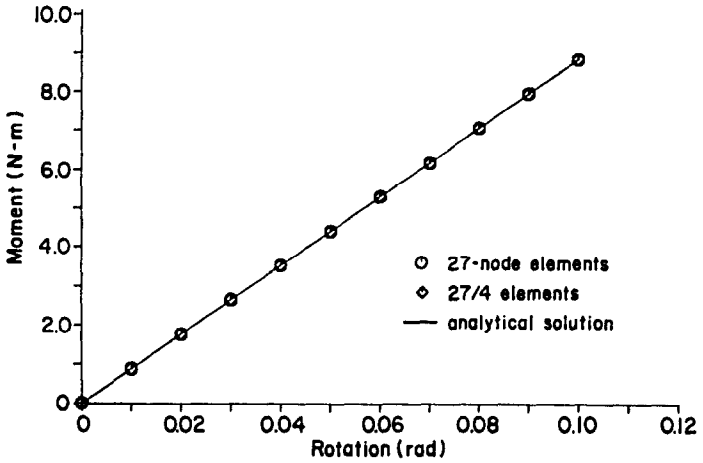

Fig. 6.35. Moment–rotation response of rubber cylinder.

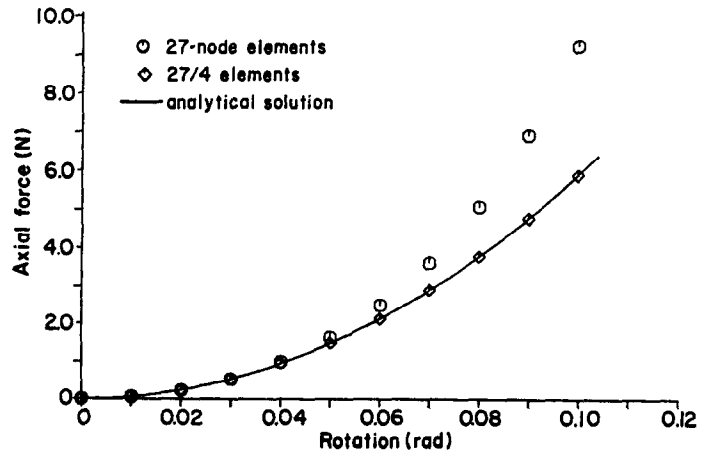

Fig. 6.36. Axial force–rotation response of rubber cylinder.

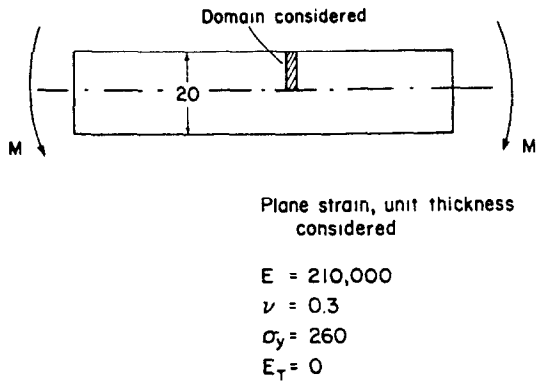

Fig. 6.37. Elasto-plastic beam in bending.

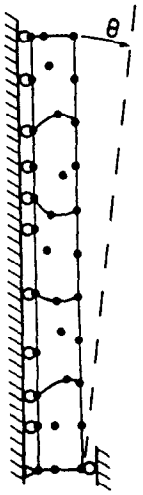

Fig. 6.38. Five 9/3 element mesh for beam in bending.

employ a contact algorithm to model the punch indentation.

A prescribed displacement of 0.1 in. is applied in 100 equal load steps. The plastic zones and pressure bands for the 160 element meshes corresponding to a displacement of 0.1 in. are shown in Fig. 6.42. The outlines of the plastic zones show considerable detail.† The pressure bands for the displacement-based elements correspond to, but are much less distinct than, the pressure bands for the 9/3 elements. (In the displacement-based analysis of elasto-plastic materials, the pressures used in the pressure band plots are calculated by extrapolating the pressures computed at the integration points in an element throughout the rest of the element with Lagrange polynomials.)

The force–deflection curves for all six solutions are shown in Fig. 6.43. We see that, for the same mesh layout, the u/p elements give a more accurate limit load than the displacement-based elements. Also the final slopes from the u/p formulation analyses are lower than the final slopes from the displacement-based formulation analyses. Notice that both formulations overestimate the analytical solution, and that the overestimate is less for the more refined meshes.

6.4.3 *Elasto-plastic fracture mechanics analysis of a cracked specimen.* We consider the plane strain cracked specimen in tension shown in Fig. 6.44. The load R is evenly distributed over the top and bottom edges of the specimen and is statically equivalent to a force applied along the center of the uncracked specimen. The goal of the analysis is to determine the limit load and the J-integral vs displacement curve, assuming only material nonlinearities and that the crack does not propagate.

The J-integral is defined as [53]

$$J = \oint \left(W \, dx_2 - T_i \frac{\partial u_i}{\partial x_1} \, ds \right), \tag{6.17}$$

where the specimen is located in the x_1–x_2 plane with the crack parallel to the x_1 axis, W is the strain energy density and T_i is the traction vector. In the

† We note that the plastic zone plots have some unrealistic features, such as the single plastic integration point at the lower left-hand corner of the mesh and sometimes a few unloaded spots in the middle of a plastic region.

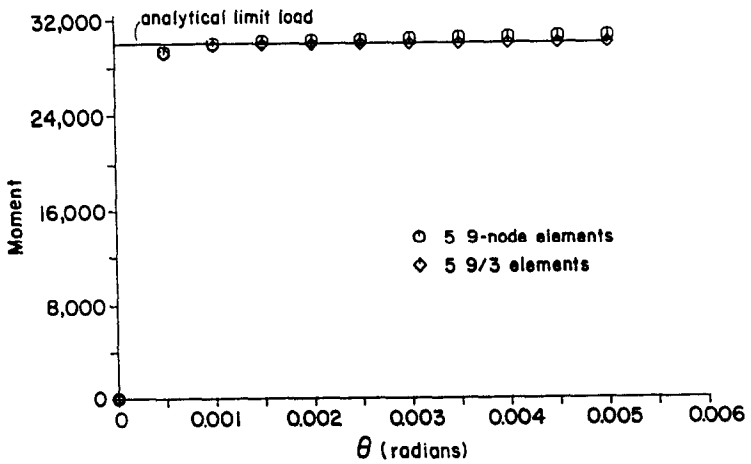

Fig. 6.39. Moment–rotation response of beam in bending.

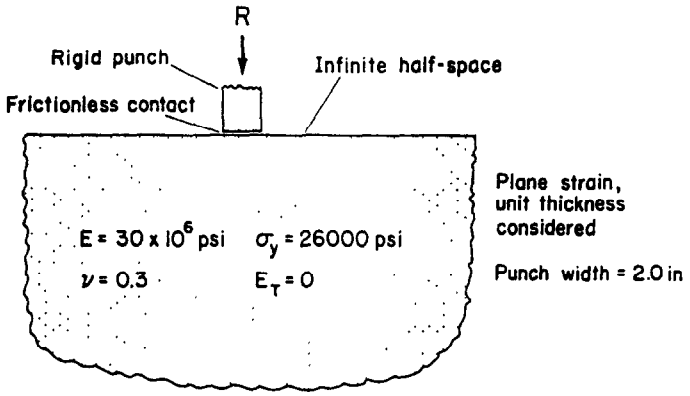

Fig. 6.40. Indentation of an elastic–perfectly plastic half-space by a smooth punch.

analysis to be considered, J can also be conceptually evaluated using

$$J = -\frac{1}{B}\frac{d\mathscr{W}}{da}, \tag{6.18}$$

where B is the specimen thickness, $\mathscr{W}$ is the work input to the specimen and a is the crack length. Although there are theoretical questions regarding the use of the J-integral in elasto-plastic analysis when an incremental elasto-plastic material description is used, there is evidence that the J-integral can be a useful fracture criterion [54].

A limit load estimate for this problem is provided by Rice's upper bound slip-line solution [55]. Using the procedure discussed in [55], we obtain the slip-line solution for this problem (shown in Fig. 6.45) and the limit load $R_L = 459.72$ MN.

For elastic conditions, the stress intensity factor for this problem is [56]:

$$K_I = 1.99\sigma_\infty\sqrt{\pi a}, \tag{6.19}$$

where σ_∞ is the far-field stress, which gives J for elastic conditions. For plastic conditions, the J-integral vs displacement curve is not known. However, we can estimate the final slope of this curve as follows:

$$\left.\frac{dJ}{d\Delta}\right|_{\text{limit}} = -\frac{1}{B}\left.\frac{d\left(\frac{d\mathscr{W}}{d\Delta}\right)}{da}\right|_{\text{limit}} = -\frac{1}{B}\frac{dR_L}{da}$$

$$\doteq -\frac{1}{B}\left(\frac{R_L\Big|_{a_2} - R_L\Big|_{a_1}}{a_2 - a_1}\right), \tag{6.20}$$

where a_1 and a_2 are two crack lengths. Repeating the calculations for Rice's upper bound solution with a crack length of 0.376 m gives

$$R_L\Big|_{a=0.376} = 458.34 \text{ MN}$$

and therefore

$$\frac{dJ}{d\Delta} \doteq 1380 \frac{\text{MN}}{\text{m}^2}.$$

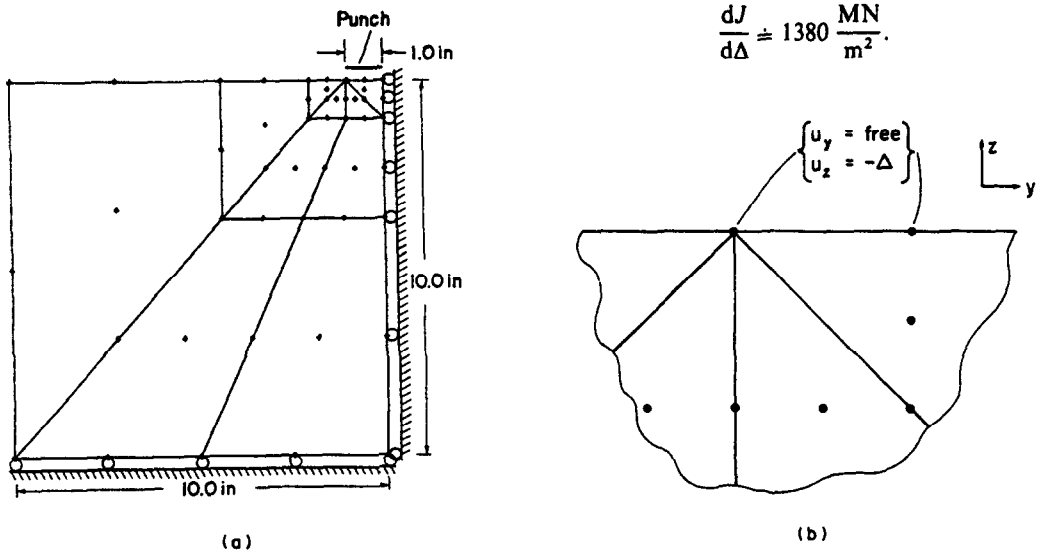

Fig. 6.41. Ten element mesh for indentation problem. (a) Mesh layout. (b) Boundary conditions used to model punch.

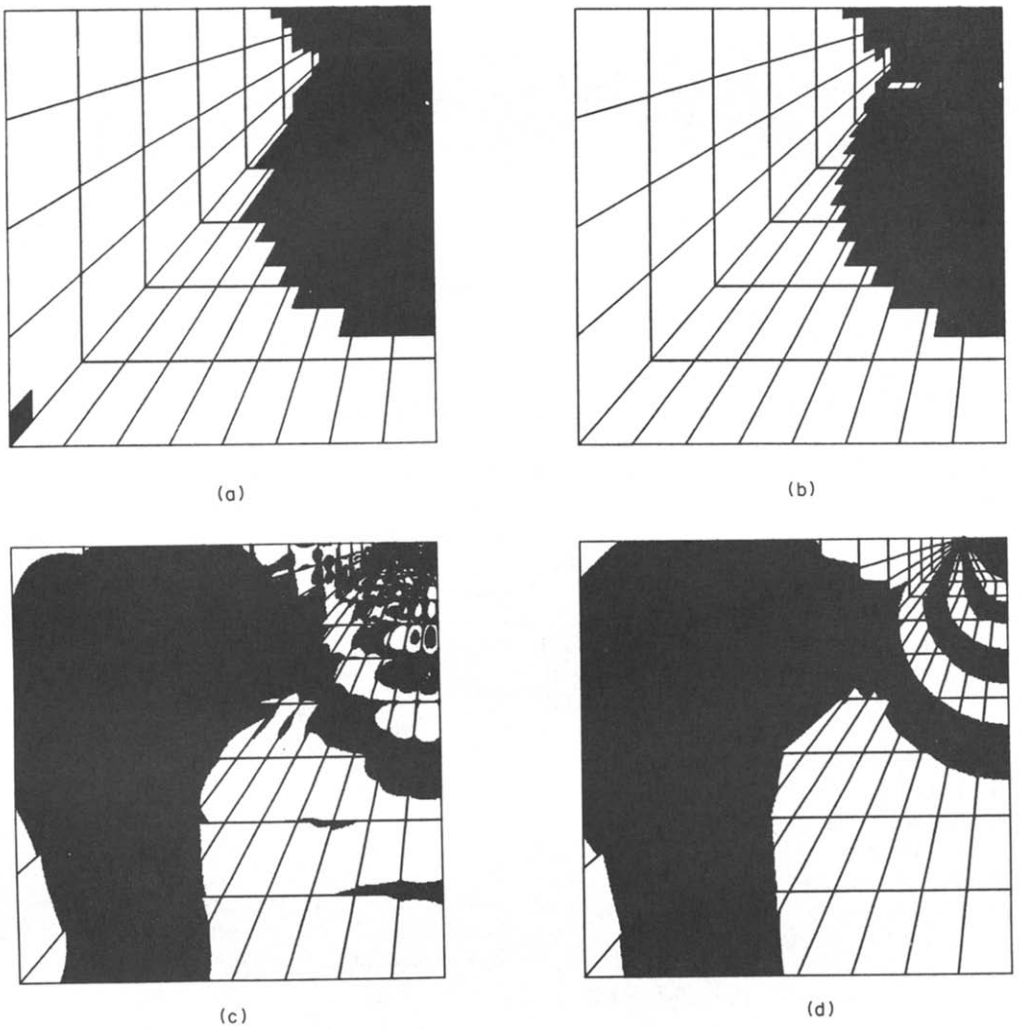

Fig. 6.42. Results for 160 element meshes of indentation problem. (a) Plastic zone plot, 9-node elements. (b) Plastic zone plot, 9/3 elements. (c) Pressure band plot, 9-node elements, band width = 10,000 psi. (d) Pressure band plot, 9/3 elements, band width = 10,000 psi.

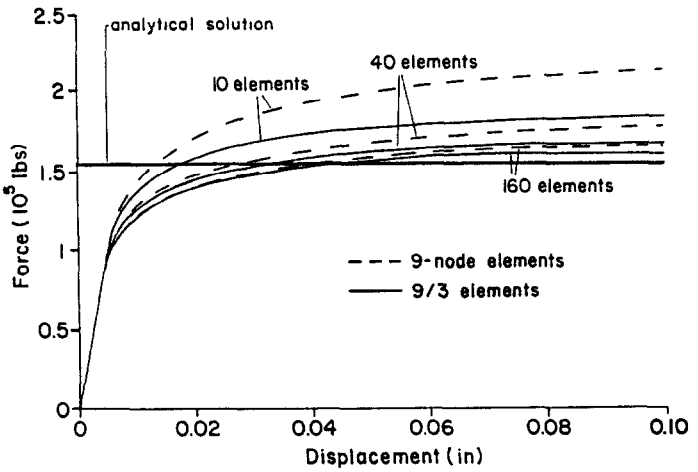

Fig. 6.43. Force–deflection curves for indentation problem.

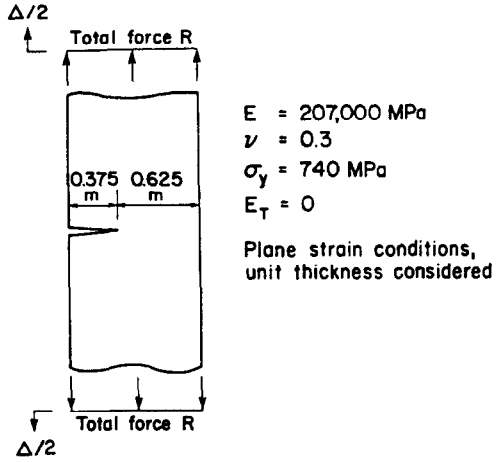

Fig. 6.44. Elastic–plastic cracked specimen in tension.

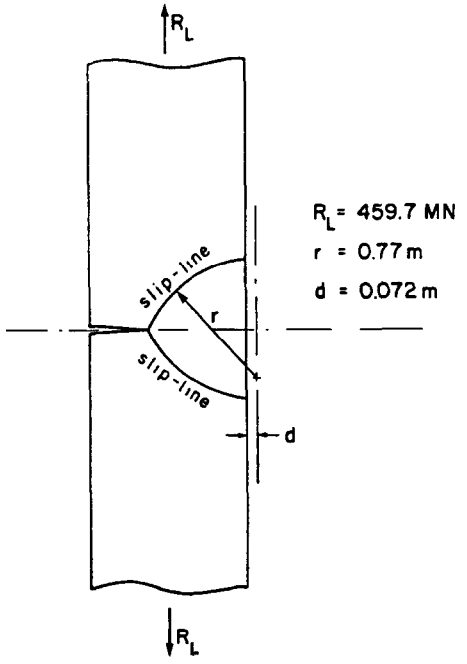

Fig. 6.45. Rice's upper bound slip-line solution for cracked specimen.

The mesh layouts we use, shown in Fig. 6.46, contain 15 elements, 68 elements and 156 elements. We use both 9-node elements and 9/3 elements to solve this problem. Figure 6.47 shows the model of the crack tip for the 15 element mesh; note that independent degrees of freedom are assigned for the nodes on the collapsed element sides to allow the mesh to contain a $1/r$ strain singularity. We model a crack tip advance by moving the crack tip node by 0.001 m and shifting all nodes that are closer than 0.05 m from the crack tip as shown in Fig. 6.48. At the top of the mesh, the load is applied by specifying the displacement $u = \Delta/2$ of the center node. Rigid links along the top line transmit this displacement across the top of the mesh. Note that the top line is also allowed to rotate rigidly during the analysis.

A displacement of $u = 0.04$ m is applied in 80 equal load steps. The force–deflection curves for the

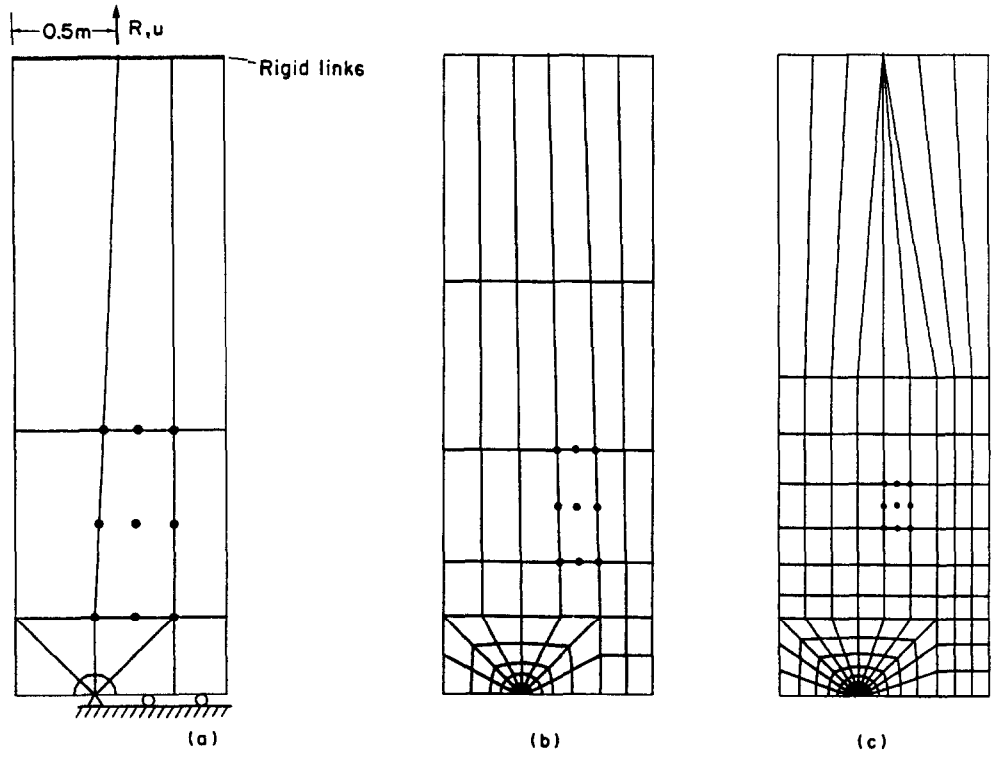

Fig. 6.46. Meshes used for cracked specimen. (a) 15 element mesh. (b) 68 element mesh. (c) 156 element mesh.

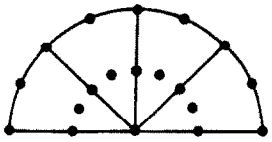

Fig. 6.47. Detail at crack tip of 15 element mesh for cracked specimen.

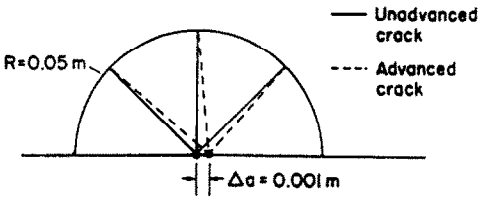

Fig. 6.48. Modeling of crack tip advance for cracked specimen.

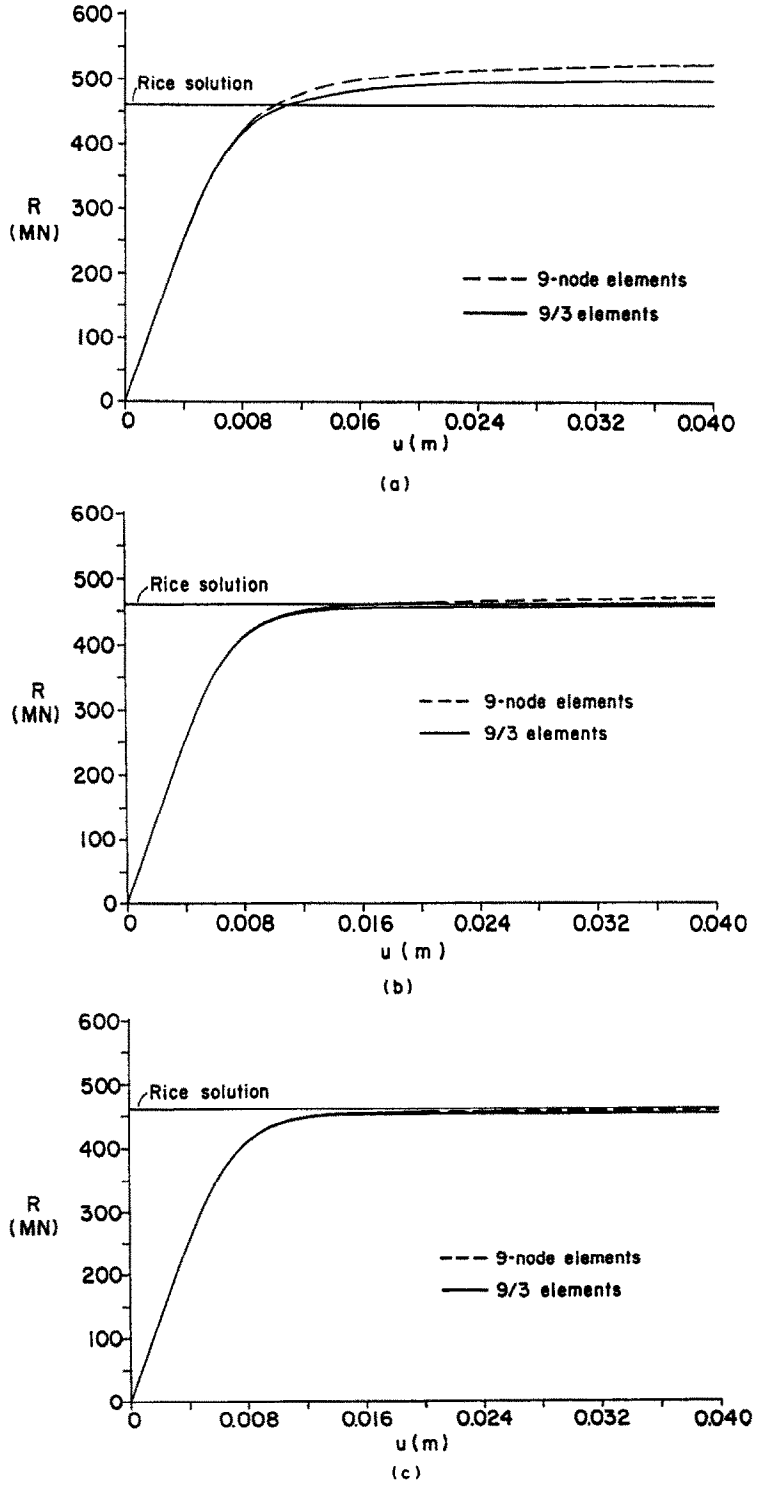

Fig. 6.49. Force–deflection curves for cracked specimen. (a) 15 element mesh. (b) 68 element mesh (c) 156 element mesh.

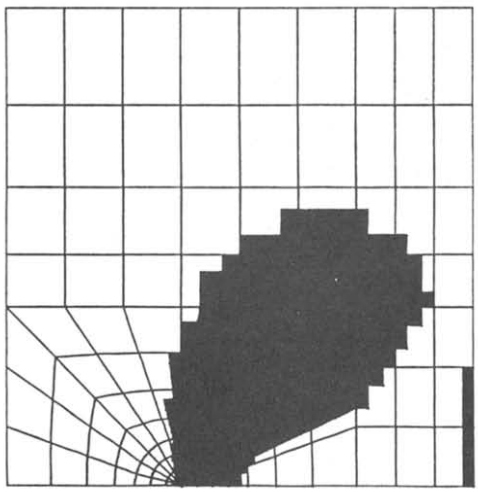

(a)

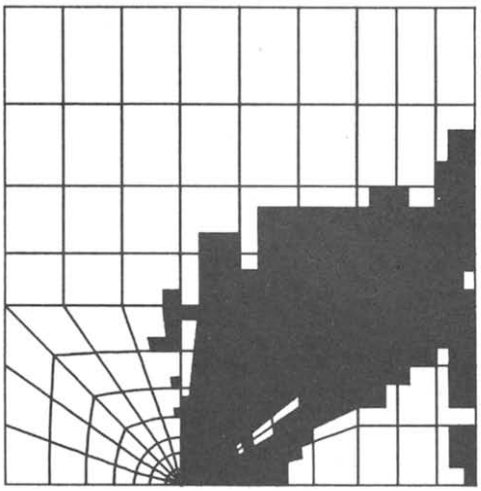

(d)

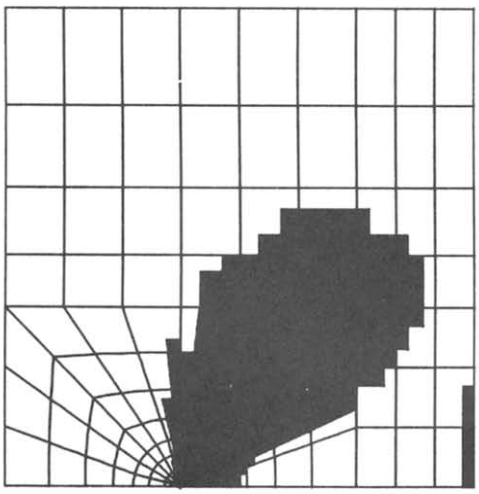

(b)

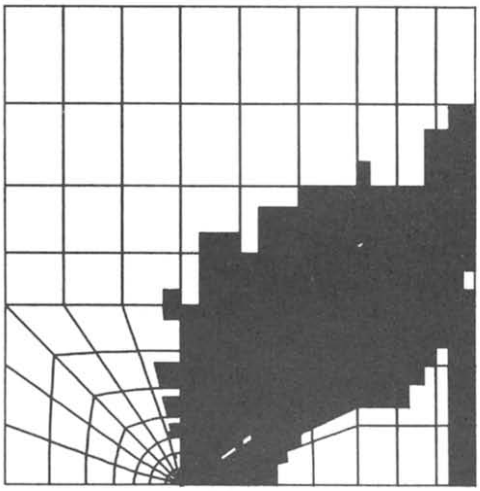

(e)

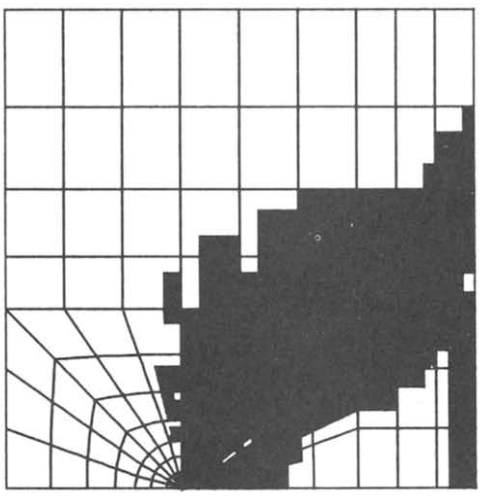

(c)

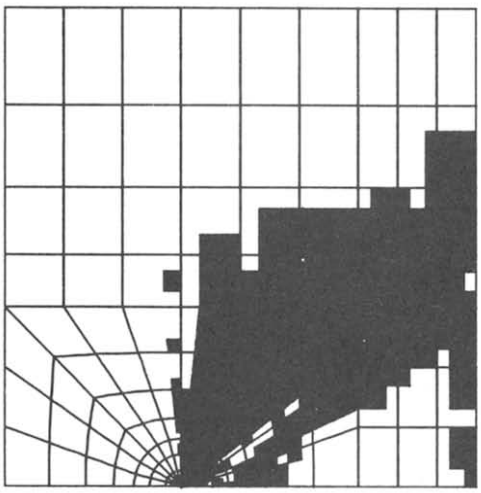

(f)

Fig. 6.50.

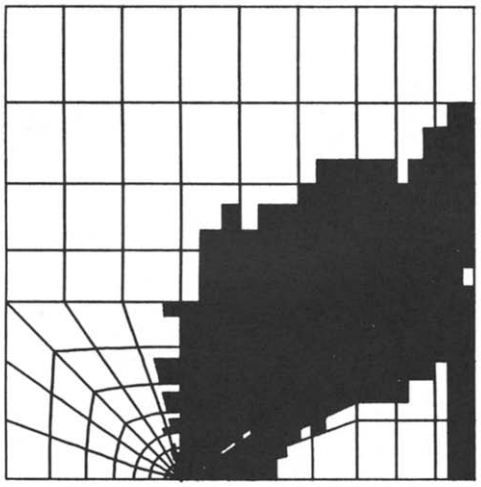

(g)

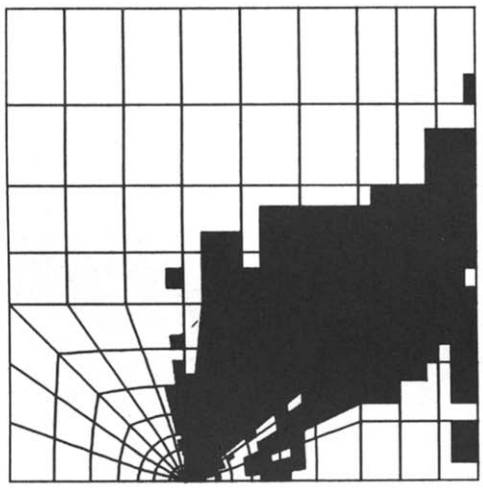

(h)

Fig. 6.50. Plastic zone plots for 156 element mesh of cracked specimen. (a) $u = 0.01$ m, 9-node elements. (b) $u = 0.01$ m, 9/3 elements. (c) $u = 0.02$ m, 9-node elements. (d) $u = 0.02$ m, 9/3 elements. (e) $u = 0.03$ m, 9-node elements. (f) $u = 0.03$ m, 9/3 elements. (g) $u = 0.04$ m, 9-node elements. (h) $u = 0.04$ m, 9/3 elements.

three meshes are shown in Fig. 6.49. It is seen that, for the same mesh layout, the u/p elements give a more accurate limit load than the displacement-based elements. Notice that the Rice upper bound solution is in close agreement with the 156 element mesh results.

Plastic zone plots for the 156 element mesh solutions are shown in Fig. 6.50. Both solutions give some elastic integration points totally surrounded by plastic regions and isolated plastic integration points. Of special interest is the region just to the right of the crack tip when the u/p formulation is used. This region is plastic at $u = 0.01$ m but partially unloads as the displacement is increased.

Pressure band plots for the 156 element mesh are shown in Fig. 6.51. In all of the pressure band plots

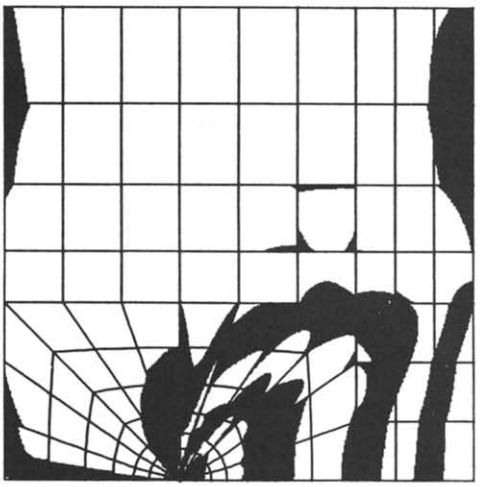

(a)

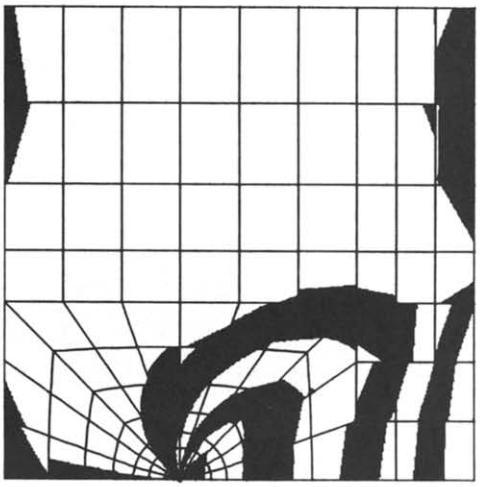

(b)

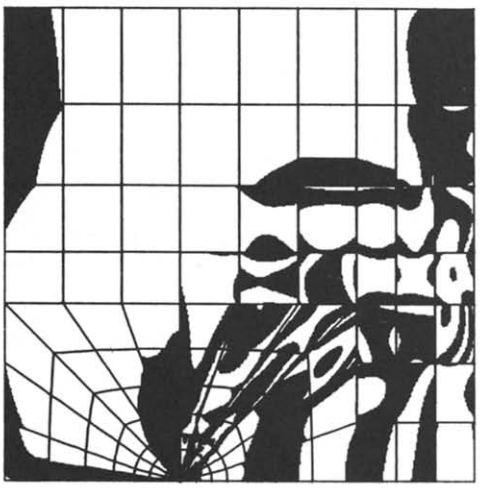

(c)

Fig. 6.51.

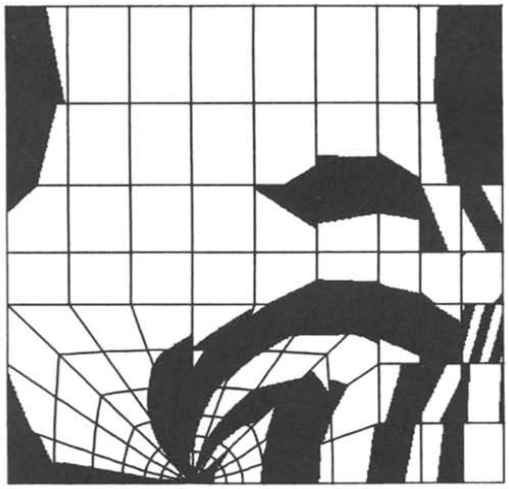

(d)

(g)

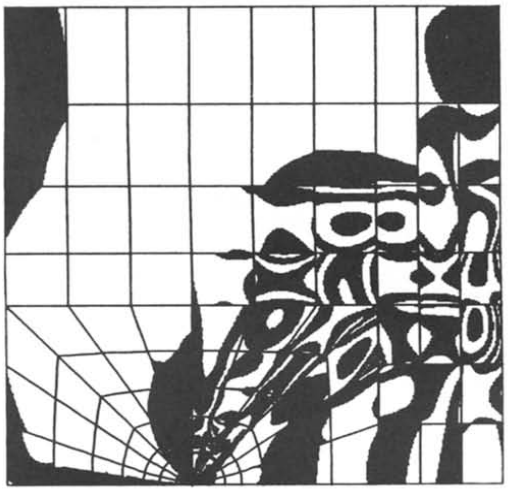

(e)

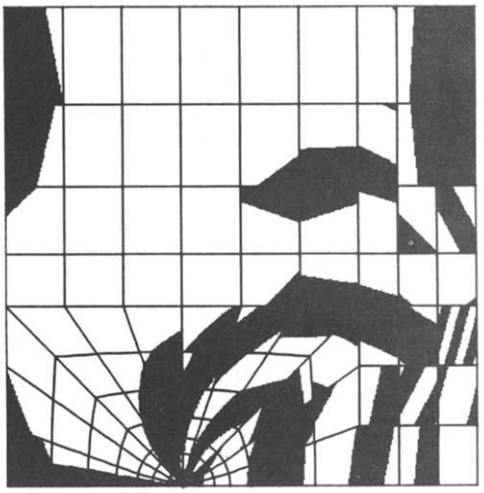

(h)

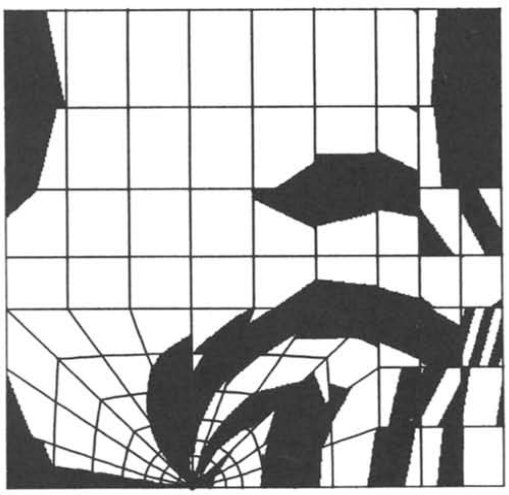

(f)

Fig. 6.51. Pressure band plots for 156 element mesh of cracked specimen. (a) $u = 0.01$ m, 9-node elements, band width = 218 MPa. (b) $u = 0.01$ m, 9/3 elements, band width = 218 MPa. (c) $u = 0.02$ m, 9-node elements, band width = 228 MPa. (d) $u = 0.02$ m, 9/3 elements, band width = 226 MPa. (e) $u = 0.03$ m, 9-node elements, band width = 228 MPa. (f) $u = 0.03$ m, 9/3 elements, band width = 226 MPa. (g) $u = 0.04$ m, 9-node elements, band width = 229 MPa. (h) $u = 0.04$ m, 9/3 elements, band width = 226 MPa.

given in this example, the band width is set to one-half of the current applied stress. The pressure bands are quite smooth for the u/p formulation solution (except for one element on the right-hand-side). The pressure bands from the displacement-based solution are distinguishable for $u = 0.01$ m, but they degenerate as the displacement is increased further.

For each load step, the J-integral is calculated by numerically differentiating the current work input for crack lengths of 0.375 and 0.376 m (see eqn 6.15). The work input is computed by numerically integrating the obtained force–deflection curve with the

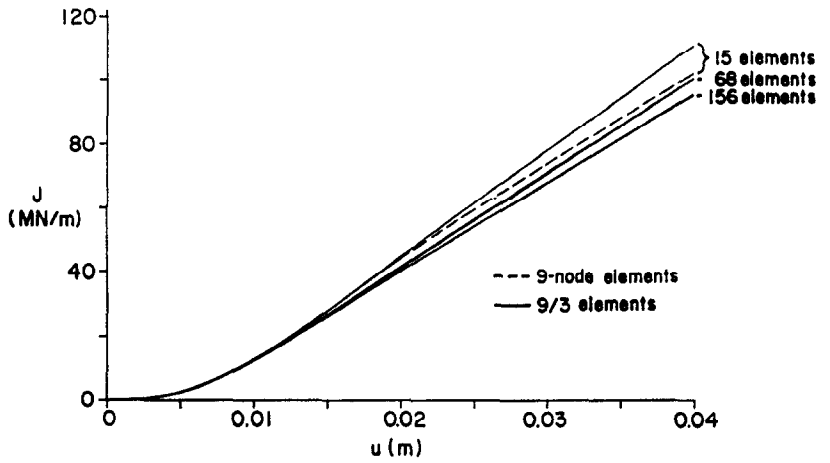

Fig. 6.52. J-integral vs displacement curves for cracked specimen.

trapezoidal rule. Figure 6.52 shows the J-integral vs displacement curves for all of the analyses. For the 15 element mesh, the u/p formulation gives higher J-integral values than does the displacement-based formulation. For the more refined meshes, both formulations give almost the same results. As the mesh is refined, the J-integral values tend to decrease.

Table 6.2 shows the elastic stress intensity factors and the final slopes of the J-integral vs displacement curves. The stress intensity factors are all close to the exact solution. For the 156 element mesh, the final slopes of the J-integral vs displacement curves agree quite well with the estimate derived above.

6.4.4 *Torsion of an elastic–plastic cylinder.* We consider a simple three-dimensional problem in this example. Figure 6.53 shows a solid cylinder, made of an elastic–perfectly plastic material, subjected to a twisting moment. We would like to determine the moment–rotation curve and, in particular, the limit moment. The analytical solution (assuming only material nonlinearities) is [57]:

$$M = \frac{\pi r^4 G}{2}\left(\frac{\theta}{L}\right) \quad \text{(elastic)} \tag{6.21a}$$

$$= \frac{2\pi r^3 \sigma_y}{3\sqrt{3}}\left[1 - \left(\frac{1}{4}\right)\left(\frac{\sigma_y}{\sqrt{3}G}\right)^3\left(\frac{L}{r\theta}\right)^3\right] \quad \text{(plastic)} \tag{6.21b}$$

where r is the radius of the cylinder, G is the elastic shear modulus, L is the length of the cylinder and θ is the total rotation. From these expressions, the limit moment is

$$M_L = \frac{2\pi r^3 \sigma_y}{3\sqrt{3}} \tag{6.22}$$

and substituting material and geometric data for this problem gives $M_L = 0.1119$ MN-m.

In this example, we contrast the solutions obtained as the basic mesh layout of eight collapsed 27-node elements shown in Fig. 6.54 is distorted. We consider the use of both displacement-based elements and 27/4 elements. The meshes we employ are a relatively undistorted mesh in which all the nodes are in their 'natural' locations (Fig. 6.55(a)), a mesh in which only the element internal nodes are shifted slightly (Fig. 6.56(a)), and a mesh in which all structural internal nodes are randomly shifted (Fig. 6.57(a)). In all cases, the boundary conditions and loadings are as follows. On the far end of the cylinder, all of the nodes are fixed. On the near end, the angular displacement of the center node is prescribed and rigid links placed between this node and the other nodes on the near end cause the entire cross-section to rotate by this amount.

Table 6.2. Elastic stress intensity factors and limit slopes of J-integral curves for cracked specimen (the 15 element, displacement-based solution results happen to be quite accurate)

	$\frac{K_I}{\sigma_\infty\sqrt{\pi a}}$	$\frac{dJ}{d\Delta}\Big\|_{a=0.04\text{ m}}$ (MN/m^2)
15 elements, displacement-based	1.97	1390
15 elements, u/p formulation	1.98	1650
68 elements, displacement-based	1.98	1450
68 elements, u/p formulation	1.98	1490
156 elements, displacement-based	1.98	1370
156 elements, u/p formulation	1.98	1390
Analytical stress intensity factor	1.99	—
$dJ/d\Delta$ from eqn (6.20)	—	1380

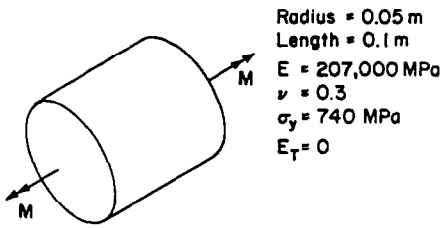

Fig. 6.53. Elastic–plastic cylinder in torsion.

We applied a total angular displacement of 0.1 rad in ten equal load steps. The moment–rotation curves for the undistorted mesh are shown in Fig. 6.55(b). Both the displacement-based formulation and the u/p formulation give the exact solution. The moment–rotation curves for the slightly distorted mesh are shown in Fig. 6.56(b). Now neither formulation gives the exact solution, but the u/p formulation is more accurate. The moment–rotation curves for the mildly distorted mesh are shown in Fig. 6.57(b). The displacement-based formulation curve has a nonzero final slope; however, the u/p formulation curve has an almost zero final slope and the limit moment obtained is still quite accurate.

7. CONCLUDING REMARKS

We have presented a displacement–pressure (u/p) finite element formulation intended primarily for the analysis of almost incompressible materials. The u/p formulation can be used to solve problems involving elastic material descriptions (such as rubber-like nonlinear elasticity) and problems involving inelastic material descriptions (such as elasto-plasticity). Our formulation explicitly combines the following features:

- The tangent stiffness matrix is symmetric.
- The pressure computed from the displacements is completely replaced by a separately interpolated pressure.

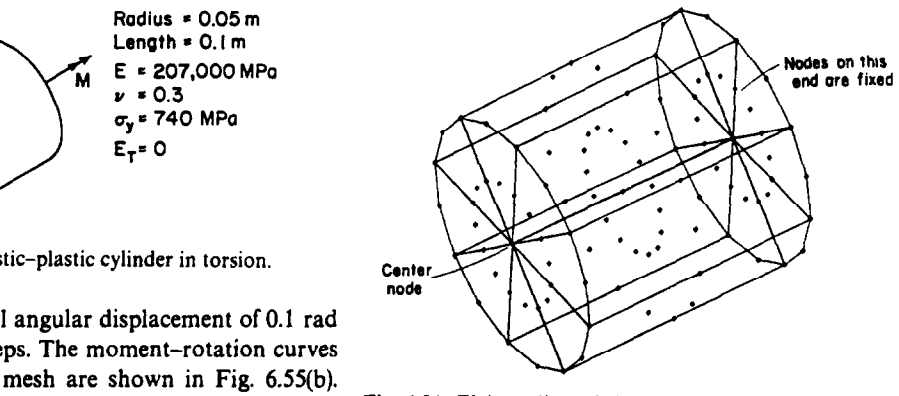

Fig. 6.54. Eight collapsed 27/4 element mesh for elastic–plastic cylinder.

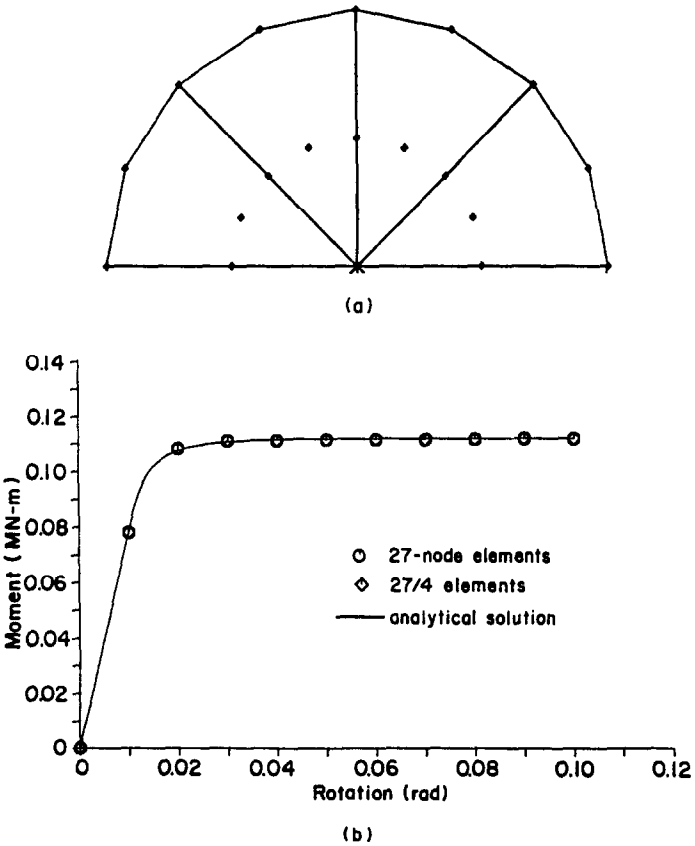

Fig. 6.55. 'Undistorted' mesh results for elastic–plastic cylinder. (a) End view of cylinder. (b) Moment–rotation response.

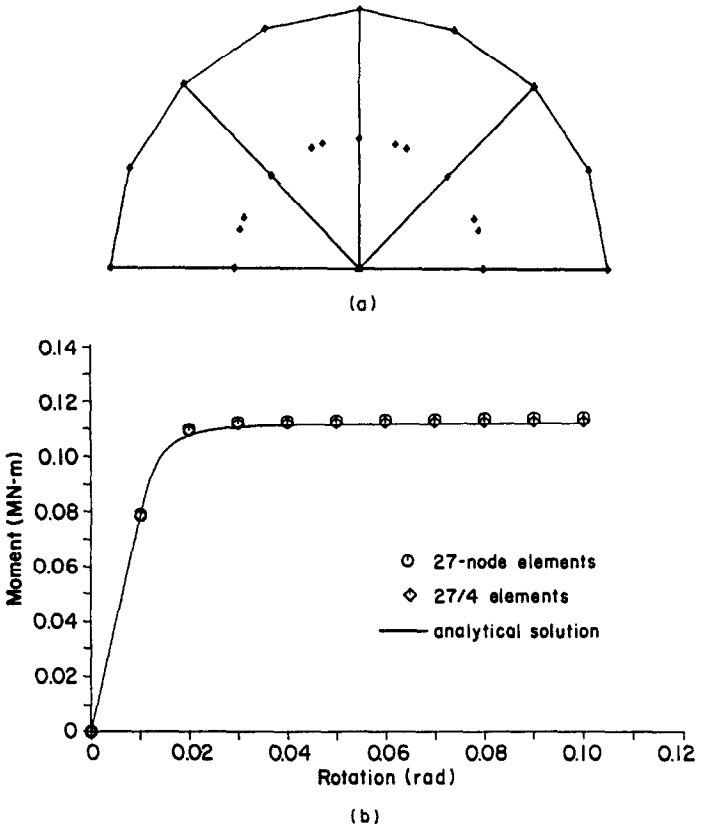

Fig. 6.56. Slightly distorted mesh results for elastic–plastic cylinder. (a) End view of cylinder. (b) Moment–rotation response.

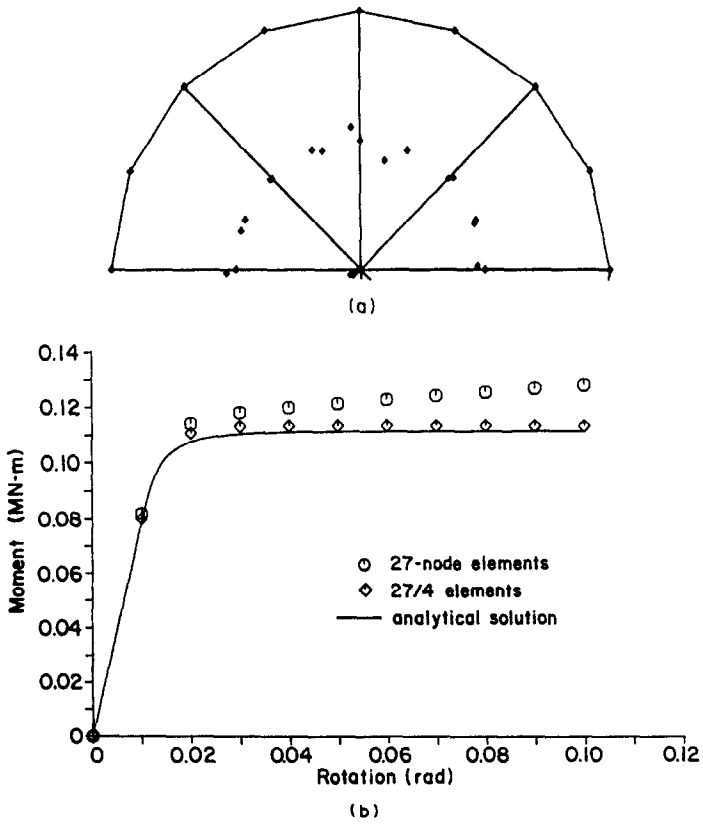

Fig. 6.57. Mildly distorted mesh results for elastic–plastic cylinder. (a) End view of cylinder. (b) Moment–rotation response.

- The pressure constraint equation is realistic.
- The u/p formulation includes the displacement-based formulation as a special case.

We show that these features imply a material restriction; roughly speaking, only materials with a constant bulk modulus can be used with the u/p formulation. However, for many practical analyses, this restriction is not very serious.

We describe the implementation of linear elastic isotropic and orthotropic material descriptions, a simple elasto-plastic material description and some rubber-like material descriptions (Mooney–Rivlin and Ogden).

In incremental nonlinear analysis, both the nodal point displacements and the pressure variables are incrementally updated during each equilibrium iteration. In contact analysis, we use the appropriate out-of-balance force vector for contact reaction calculations. These procedures enable us to efficiently solve nonlinear problems using a simple load stepping algorithm with full Newton–Raphson equilibrium iterations.

The elements that we recommend are those that pass the Brezzi–Babuška condition: the 9/3 element for two-dimensional analysis and the 27/4 element for three-dimensional analysis. The consequences of using some other element types are shown in a brief study.

Our examples demonstrate the wide range of problems that can be analyzed with the u/p formulation. In rubber analysis, problems involving contact conditions (such as seal problems) can be effectively solved and material instabilities can be accurately predicted. In elasto-plastic analysis, for the same mesh layouts, the u/p formulation gives more accurate limit load and pressure predictions than does the displacement-based formulation.

We conclude that the u/p formulation is a robust analysis procedure, suitable for the solution of a wide variety of problems. Surely many more research topics in incompressible analysis, such as the viscoelastic modeling of rubber-type materials and the analysis of fiber-reinforced rubber components, can be addressed. Regarding the topics discussed in this paper, there is a need for new, more effective u/p elements, especially in three-dimensional analysis. Also, the analysis of rubber wrinkling under large stresses needs more attention.

REFERENCES

1. K. J. Bathe, *Finite Element Procedures in Engineering Analysis*. Prentice-Hall, Englewood Cliffs, NJ (1982).
2. R. W. Penn, Volume changes accompanying the extension of rubber. *Trans. Soc. Rheology* **14**, 509–517 (1970).
3. L. R. Herrmann, Elasticity equations for incompressible and nearly incompressible materials by a variational theorem. *AIAA Jnl* **3**, 1896–1900 (1965).
4. J. T. Oden and J. E. Key, Numerical analysis of finite axisymmetric deformations of incompressible elastic solids of revolution. *Int. J. Solids Struct.* **6**, 497–518 (1970).
5. S. W. Key, A variational principle for incompressible and nearly-incompressible anisotropic elasticity. *Int. J. Solids Struct.* **5**, 951–964 (1969).
6. J. H. Argyris, P. C. Dunne, T. Angelpoulos and B. Bichat, Large natural strains and some special difficulties due to non-linearity and incompressibility in finite elements. *Comp. Meth. appl. Mech. Engng* **4**, 219–278 (1974).
7. J. C. Nagtegaal, D. M. Parks and J. R. Rice, On numerically accurate finite element solutions in the fully plastic range. *Comp. Meth. appl. Mech. Engng* **4**, 153–177 (1974).
8. T. Sussman and K. J. Bathe, Studies of finite element procedures—stress band plots and the evaluation of finite element meshes. *Engng Comput.* **3**, 178–191 (1986).
9. M. H. Gadala, Numerical solutions of nonlinear problems of continua—II. Survey of incompressibility constraints and software aspects. *Comput. Struct.* **22**, 841–855 (1986).
10. R. L. Taylor, K. S. Pister and L. R. Herrmann, On a variational theorem for incompressible and nearly-incompressible orthotropic elasticity. *Int. J. Solids Struct.* **4**, 875–883 (1968).
11. M. Crouzeix and P. A. Raviart, Conforming and nonconforming finite element methods for solving the stationary Stokes equations I. *R.A.I.R.O.* **7**, R-3, 33–76 (1973).
12. F. Brezzi, On the existence, uniqueness and approximation of saddle-point problems arising from Lagrangian multipliers. *R.A.I.R.O.* **8**, R-2, 129–151 (1974).
13. I. Babuška, The finite element method with Lagrangian multipliers. *Num. Math.* **20**, 179–192 (1973).
14. I. Babuška, The finite element method with penalty. *Math. Comp.* **27**, 221–228 (1973).
15. M. Fortin, An analysis of the convergence of mixed finite element methods. *R.A.I.R.O. Num. Anal.* **11**, 341–354 (1977).
16. J. T. Oden and N. Kikuchi, Finite element methods for constrained problems in elasticity. *Int. J. Numer. Meth. Engng* **18**, 701–725 (1982).
17. R. L. Sani, P. M. Gresho, R. L. Lee and D. F. Griffiths, The cause and cure (?) of the spurious pressures generated by certain FEM solutions of the incompressible Navier–Stokes Equations, Parts 1 and 2. *Int. J. Numer. Meth. Fluids* **1**, 17–43, 171–204 (1981).
18. D. S. Malkus and T. J. R. Hughes, Mixed finite element methods—reduced and selective integration techniques: a unification of concepts. *Comp. Meth. appl. Engng* **15**, 63–81 (1978).
19. M. Bercovier, Y. Hasbani, Y. Gilon and K. J. Bathe, On a finite element procedure for nonlinear incompressible elasticity. In *Hybrid and Mixed Finite Element Methods*, Ch. 26 (Edited by S. N. Atluri *et al.*). John Wiley, New York (1983).
20. M. S. Engelman, R. L. Sani, P. M. Gresho and M. Bercovier, Consistent vs. reduced integration penalty methods for incompressible media using several old and new elements. *Int. J. Numer. Meth. Fluids* **2**, 25–42 (1982).
21. M. Bercovier, Perturbation of mixed variational problems. Application to mixed finite element methods. *R.A.I.R.O. Num. Anal.* **12**, 211–236 (1978).
22. B. Häggblad and K. J. Bathe, Finite element analysis of rubber-like solids. *Int. J. Numer. Meth. Engng* (to appear).
23. B. Häggblad and J. A. Sundberg, Large strain solutions of rubber components. *Comput. Struct.* **17**, 835–843 (1983).
24. E. Jankovich, F. Leblanc, M. Durand and M. Bercovier, A finite element for the analysis of rubber parts,

experimental and analytical assessment. *Comput. Struct.* **14**, 385–391 (1981).
25. A. B. Zdunek and M. Bercovier, Numerical evaluation of finite element methods for rubber parts. *Proceedings of the Sixth International Conference on Vehicle Structural Mechanics*, Society of Automotive Engineers, Detroit (1986).
26. A. Mendelson, *Plasticity: Theory and Applications*. Macmillan, New York (1968).
27. R. Hill, On constitutive inequalities for simple materials, Parts I and II. *J. Mech. Phys. Solids* **16**, 229–242, 315–332 (1968).
28. M. Kojić and K. J. Bathe, The 'effective-stress-function' algorithm for thermo-elasto-plasticity and creep. *Int. J. Numer. Meth. Engng* (in press).
29. R. S. Rivlin, Large elastic deformations of isotropic materials IV. Further developments of the general theory. *Phil. Trans. A* **241**, 379–397 (1948).
30. L. R. G. Treloar, *The Physics of Rubber Elasticity*, 2nd Edition. Oxford University Press, London (1958).
31. R. W. Ogden, Volume changes associated with the deformation of rubber-like solids. *J. Mech. Phys. Solids* **24**, 323–338 (1976).
32. L. R. G. Treloar, Dilation of rubber on extension. *Polymer* **19**, 1414–1420 (1978).
33. R. W. Ogden, Large deformation isotropic elasticity—on the correlation of theory and experiment for incompressible rubber-like solids. *Proc. R. Soc. Lond.* **A326**, 565–584 (1972).
34. F. Brezzi and K. J. Bathe, Studies of finite element procedures—the inf-sup condition, equivalent forms and applications. In *Reliability of Methods for Engineering Analysis* (Edited by K. J. Bathe and D. R. J. Owen). Pineridge Press, Swansea, U.K. (1986).
35. M. Bercovier, An optimal 3D finite element for incompressible media. In *Finite Element Methods for Nonlinear Problems* (Edited by P. G. Bergan, K. J. Bathe and W. Wunderlich). Springer, Berlin (1985).
36. K. J. Bathe, Finite elements in CAD and ADINA. *J. Nucl. Engng Des.* **98**, 57–67 (1986).
37. C. F. Shih and A. Needleman, Fully plastic crack problems, Part 1: solutions by a penalty method. *J. appl. Mech.* **51**, 48–56 (1984).
38. C. G. Floyd, The determination of stresses using a combined theoretical and experimental analysis approach. *2nd Int. Conf. on Computational Methods and Experimental Measurements* (Edited by C. A. Brebbia). Springer, Berlin (1984).
39. T. Sussman and K. J. Bathe, Studies of finite element procedures—on mesh selection. *Comput. Struct.* **21**, 257–264 (1985).
40. C. A. Brebbia, S. Umetani and J. Trevelyan, Critical comparison of boundary element and finite element methods for stress analysis. *BETECH 85, Proc. First Boundary Element Tech. Conf.* (Edited by C. A. Brebbia and B. J. Noye), pp. 225–256 (1985).
41. S. G. Lekhnitskii, *Theory of Elasticity of an Anisotropic Body*. Mir, Moscow (1977).
42. K. J. Bathe and A. Chaudhary, A solution method for planar and axisymmetric contact problems. *Int. J. Numer. Meth. Engng* **21**, 65–88 (1985).
43. P. B. Lindley, Compression characteristics of laterally-unrestrained rubber O-rings. *J. Instn Rubb. Ind.* **4**, 209–213 (1967).
44. R. J. Roark and W. C. Young, *Formulas for Stress and Strain*, 5th Edition. McGraw-Hill, New York (1975).
45. E. F. Göbel, *Rubber Springs Design*. Newnes-Butterworth, London (1974).
46. E. W. Wilkes, On the stability of a circular tube under end thrust. *Q. J. Mech. appl. Math.* **8**, 88–100 (1955).
47. T. H. Miller, A finite element study of instabilities in rubber elasticity. Ph.D. Dissertation, The University of Texas at Austin, Texas (1982).
48. P. W. Allen, P. B. Lindley and A. R. Payne (eds), Use of rubber in engineering. Proceedings, Conference, Imperial College, London (1966).
49. A. B. Zdunek, private communication.
50. R. S. Rivlin, Large elastic deformations of isotropic materials III. Some simple problems in cylindrical polar co-ordinates. *Phil. Trans. A* **240**, 509–525 (1948).
51. H. G. deLorenzi and C. F. Shih, On the use of 2D isoparametric elements for calculations in the fully plastic range. *Int. J. Fract.* **13**, 507–511 (1977).
52. R. Hill, *The Mathematical Theory of Plasticity*. Oxford University Press, London (1950).
53. J. R. Rice, A path independent integral and the approximate analysis of strain concentration by notches and cracks. *J. appl. Mech.* **35**, 379–386 (1968).
54. J. A. Begley and J. D. Landes, The *J*-integral as a fracture criterion. *Fracture Toughness, Proceedings of the 1971 National Symposium on Fracture Mechanics, Part II*, ASTM STP 514 (1972).
55. J. R. Rice, The line spring model for surface flaws. In *The Surface Crack: Physical Problems and Computational Solutions* (Edited by J. L. Swedlow). ASME, New York (1972).
56. D. P. Rooke and D. J. Cartwright, *Compendium of Stress Intensity Factors*. H.M.S.O., London (1976).
57. S. H. Crandall *et al.*, *An Introduction to the Mechanics of Solids*, 2nd Edition. McGraw-Hill, New York (1978).
58. F. Tabaddor and J. R. Stafford, Some aspects of rubber composite finite element analysis. *Comput. Struct.* **21**, 327–339 (1985).
59. A. E. Green and W. Zerna, *Theoretical Elasticity*. Clarendon Press, Oxford (1954).
60. H. Reismann and P. S. Pawlik, *Elasticity: Theory and Applications*. John Wiley, New York (1980).

APPENDIX A: THE STRESSES AND TANGENT CONSTITUTIVE TENSOR FOR THE COMPRESSIBLE MOONEY-RIVLIN MATERIAL DESCRIPTION

We derive the 2nd Piola-Kirchhoff stress tensor and the tangent constitutive tensor for the compressible Mooney-Rivlin material description, assuming general three-dimensional deformations. The strain energy density for the compressible Mooney-Rivlin material description is†

$$ {}^{t}_{0}W = C_1({}^{t}_{0}J_1 - 3) + C_2({}^{t}_{0}J_2 - 3) + \tfrac{1}{2}\kappa({}^{t}_{0}J_3 - 1)^2. \quad \text{(A.1)} $$

First we discuss some fundamental concepts and introduce a new notation. As is well known, the 2nd Piola-Kirchhoff stress tensor is derived using

$$ {}^{t}_{0}S_{ij} = \frac{1}{2}\left(\frac{\partial\, {}^{t}_{0}W}{\partial\, {}^{t}_{0}\varepsilon_{ij}} + \frac{\partial\, {}^{t}_{0}W}{\partial\, {}^{t}_{0}\varepsilon_{ji}}\right) \quad \text{(A.2)} $$

and the constitutive tensor is obtained using

$$ {}_{0}C_{ijrs} = \frac{1}{2}\left(\frac{\partial\, {}^{t}_{0}S_{ij}}{\partial\, {}^{t}_{0}\varepsilon_{rs}} + \frac{\partial\, {}^{t}_{0}S_{ij}}{\partial\, {}^{t}_{0}\varepsilon_{sr}}\right). \quad \text{(A.3)} $$

The use of the operator

$$ \frac{1}{2}\left(\frac{\partial}{\partial\, {}^{t}_{0}\varepsilon_{ij}} + \frac{\partial}{\partial\, {}^{t}_{0}\varepsilon_{ji}}\right) \quad \text{(A.4)} $$

instead of $\partial/\partial\, {}^{t}_{0}\varepsilon_{ij}$ is consistent with the fact that ${}^{t}_{0}\varepsilon_{ij}$ is a symmetric tensor and ensures that ${}^{t}_{0}S_{ij}$ and ${}_{0}C_{ijrs}$ have the correct symmetries [59]. Since we will apply the operation

† In Appendices A and B, we omit the overbar used in the body of the paper to denote 'computed from displacements'.

(A.4) often, we use the abbreviation

$$( )^{*}_{ij} = \frac{1}{2}\left(\frac{\partial}{\partial\, {}^{t}_{o}\varepsilon_{ij}} + \frac{\partial}{\partial\, {}^{t}_{o}\varepsilon_{ji}}\right) \tag{A.5}$$

which, since ${}^{t}_{o}\varepsilon_{ij} = \frac{1}{2}({}^{t}_{o}C_{ij} - \delta_{ij})$, may be written as

$$( )^{*}_{ij} = \frac{\partial}{\partial\, {}^{t}_{o}C_{ij}} + \frac{\partial}{\partial\, {}^{t}_{o}C_{ji}}. \tag{A.6}$$

Note that the operator $( )^{*}_{ij}$ is a linear operator and may be manipulated using the usual rules of chain differentiation.

Applying the operator (A.6) to eqn (A.1) gives

$${}^{t}_{o}S_{ij} = C_1({}^{t}_{o}J_1)^{*}_{ij} + C_2({}^{t}_{o}J_2)^{*}_{ij} + \kappa({}^{t}J_3 - 1)({}^{t}_{o}J_3)^{*}_{ij}, \tag{A.7}$$

where

$$({}^{t}_{o}J_1)^{*}_{ij} = ({}^{t}_{o}I_3)^{-1/3}({}^{t}_{o}I_1)^{*}_{ij} - \tfrac{1}{3}({}^{t}_{o}I_1\, {}^{t}_{o}I_3^{-4/3})({}^{t}_{o}I_3)^{*}_{ij} \tag{A.8a}$$

$$({}^{t}_{o}J_2)^{*}_{ij} = ({}^{t}_{o}I_3)^{-2/3}({}^{t}_{o}I_2)^{*}_{ij} - \tfrac{2}{3}({}^{t}_{o}I_2\, {}^{t}_{o}I_3^{-5/3})({}^{t}_{o}I_3)^{*}_{ij} \tag{A.8b}$$

$$({}^{t}_{o}J_3)^{*}_{ij} = \tfrac{1}{2}({}^{t}_{o}I_3)^{-1/2}({}^{t}_{o}I_3)^{*}_{ij} \tag{A.8c}$$

and

$$({}^{t}_{o}I_1)^{*}_{ij} = 2\delta_{ij} \tag{A.9a}$$

$$({}^{t}_{o}I_2)^{*}_{ij} = 2\, {}^{t}_{o}I_1\delta_{ij} - ({}^{t}_{o}C_{ij} + {}^{t}_{o}C_{ji}) \tag{A.9b}$$

$$({}^{t}_{o}I_3)^{*}_{ij} = ({}^{o}_{t}C_{ij} + {}^{o}_{t}C_{ji})(\det\, {}^{t}_{o}C) \tag{A.9c}$$

where ${}^{o}_{t}C_{ij} = ({}^{t}_{o}C_{ij})^{-1}$. An alternative way to write eqn (A.9c) is [60]:

$$({}^{t}_{o}I_3)^{*}_{ij} = \tfrac{1}{2}(\hat{\varepsilon}_{ibc}\,\hat{\varepsilon}_{jdf} + \hat{\varepsilon}_{jbc}\,\hat{\varepsilon}_{idf})\, {}^{t}_{o}C_{bd}\, {}^{t}_{o}C_{cf}. \tag{A.10}$$

Now we derive the constitutive tensor. Applying the operator (A.6) to eqn (A.7) gives

$${}_{o}C_{ijrs} = C_1({}^{t}_{o}J_1)^{**}_{ijrs} + C_2({}^{t}_{o}J_2)^{**}_{ijrs} + \kappa[({}^{t}_{o}J_3)^{*}_{ij}({}^{t}_{o}J_3)^{*}_{rs} + ({}^{t}J_3 - 1)({}^{t}_{o}J_3)^{**}_{ijrs}], \tag{A.11}$$

where

$$\begin{aligned}({}^{t}_{o}J_1)^{**}_{ijrs} = {} & ({}^{t}_{o}I_3)^{-1/3}({}^{t}_{o}I_1)^{**}_{ijrs} \\ & - \tfrac{1}{3}({}^{t}_{o}I_3)^{-4/3}[({}^{t}_{o}I_1)^{*}_{ij}({}^{t}_{o}I_3)^{*}_{rs} \\ & + ({}^{t}_{o}I_3)^{*}_{ij}({}^{t}_{o}I_1)^{*}_{rs} + ({}^{t}_{o}I_1)({}^{t}_{o}I_3)^{**}_{ijrs}] \\ & + \tfrac{4}{9}({}^{t}_{o}I_1\, {}^{t}_{o}I_3^{-7/3})({}^{t}_{o}I_3)^{*}_{ij}({}^{t}_{o}I_3)^{*}_{rs}\end{aligned} \tag{A.12a}$$

$$\begin{aligned}({}^{t}_{o}J_2)^{**}_{ijrs} = {} & ({}^{t}_{o}I_3)^{-2/3}({}^{t}_{o}I_2)^{**}_{ijrs} \\ & - \tfrac{2}{3}({}^{t}_{o}I_3)^{-5/3}[({}^{t}_{o}I_2)^{*}_{ij}({}^{t}_{o}I_3)^{*}_{rs} \\ & + ({}^{t}_{o}I_3)^{*}_{ij}({}^{t}_{o}I_2)^{*}_{rs} + ({}^{t}_{o}I_2)({}^{t}_{o}I_3)^{**}_{ijrs}] \\ & + \tfrac{10}{9}({}^{t}_{o}I_2\, {}^{t}_{o}I_3^{-8/3})({}^{t}_{o}I_3)^{*}_{ij}({}^{t}_{o}I_3)^{*}_{rs}\end{aligned} \tag{A.12b}$$

$$\begin{aligned}({}^{t}_{o}J_3)^{**}_{ijrs} = {} & -\tfrac{1}{4}({}^{t}_{o}I_3)^{-3/2}({}^{t}_{o}I_3)^{*}_{ij}({}^{t}_{o}I_3)^{*}_{rs} \\ & + \tfrac{1}{2}({}^{t}_{o}I_3)^{-1/2}({}^{t}_{o}I_3)^{**}_{ijrs}\end{aligned} \tag{A.12c}$$

and

$$({}^{t}_{o}I_1)^{**}_{ijrs} = 0 \tag{A.13a}$$

$$({}^{t}_{o}I_2)^{**}_{ijrs} = 4\delta_{ij}\delta_{rs} - 2(\delta_{ir}\delta_{js} + \delta_{is}\delta_{jr}) \tag{A.13b}$$

$$\begin{aligned}({}^{t}_{o}I_3)^{**}_{ijrs} = {} & [\hat{\varepsilon}_{irc}\,\hat{\varepsilon}_{jsf} + \hat{\varepsilon}_{isc}\,\hat{\varepsilon}_{jrf} + \hat{\varepsilon}_{jrc}\,\hat{\varepsilon}_{isf} \\ & + \hat{\varepsilon}_{jsc}\,\hat{\varepsilon}_{irf}]\, {}^{t}_{o}C_{cf}.\end{aligned} \tag{A.13c}$$

APPENDIX B: THE STRESSES AND TANGENT CONSTITUTIVE TENSOR FOR THE COMPRESSIBLE OGDEN MATERIAL DESCRIPTION

We derive the 2nd Piola–Kirchhoff stress tensor and the tangent constitutive tensor for the Ogden material description, assuming a two-dimensional plane strain or axisymmetric analysis. The strain energy density for the Ogden material description is

$${}^{t}_{o}W = {}^{t}_{o}W^{D} + {}^{t}_{o}W^{H}, \tag{B.1}$$

where

$${}^{t}_{o}W^{D} = \sum_{n=1}^{3}\frac{\mu_n}{\alpha_n}[(L_1^{\alpha_n/2} + L_2^{\alpha_n/2} + L_3^{\alpha_n/2})(L_1L_2L_3)^{-\alpha_n/6} - 3] \tag{B.2}$$

and

$${}^{t}_{o}W^{H} = \tfrac{1}{2}\kappa({}^{t}J_3 - 1)^2. \tag{B.3}$$

First we derive the 2nd Piola–Kirchhoff stress tensor. Using the notation of Appendix A, we write, using the chain rule for differentiation,

$${}^{t}_{o}S_{ij} = \frac{\partial\, {}^{t}_{o}W^{D}}{\partial L_a}(L_a)^{*}_{ij} + \kappa({}^{t}J_3 - 1)({}^{t}_{o}J_3)^{*}_{ij}, \tag{B.4}$$

where

$$\frac{\partial\, {}^{t}_{o}W^{D}}{\partial L_1} = \sum_{n=1}^{3}\mu_n[\tfrac{1}{3}L_1^{(\alpha_n/2-1)} - \tfrac{1}{6}(L_2^{\alpha_n/2} + L_3^{\alpha_n/2})L_1^{-1}](L_1L_2L_3)^{-\alpha_n/6} \tag{B.5}$$

with suitable permutations of the L_a for $\partial\, {}^{t}_{o}W^{D}/\partial L_2$ and $\partial\, {}^{t}_{o}W^{D}/\partial L_3$. Since in two-dimensional analysis

$$L_1 = \frac{C_{11} + C_{22}}{2} + \sqrt{\left(\frac{C_{11} - C_{22}}{2}\right)^2 + C_{12}C_{21}} \tag{B.6}$$

$$L_2 = \frac{C_{11} + C_{22}}{2} - \sqrt{\left(\frac{C_{11} - C_{22}}{2}\right)^2 + C_{12}C_{21}} \tag{B.7}$$

$$L_3 = C_{33} \tag{B.8}$$

(we omit the left subscripts and superscripts on the Cauchy–Green deformation tensor for brevity), we obtain

$$(L_1)^{*}_{11} = 1 + \left(\frac{C_{11} - C_{22}}{2}\right)\left[\left(\frac{C_{11} - C_{22}}{2}\right)^2 + C_{12}C_{21}\right]^{-1/2} \tag{B.9a}$$

$$(L_1)^*_{22} = 1 - \left(\frac{C_{11} - C_{22}}{2}\right)\left[\left(\frac{C_{11} - C_{22}}{2}\right)^2 + C_{12}C_{21}\right]^{-1/2} \tag{B.9b}$$

$$(L_1)^*_{12} = \tfrac{1}{2}(C_{12} + C_{21})\left[\left(\frac{C_{11} - C_{22}}{2}\right)^2 + C_{12}C_{21}\right]^{-1/2} \tag{B.9c}$$

and

$$(L_2)^*_{11} = 1 - \left(\frac{C_{11} - C_{22}}{2}\right)\left[\left(\frac{C_{11} - C_{22}}{2}\right)^2 + C_{12}C_{21}\right]^{-1/2} \tag{B.10a}$$

$$(L_2)^*_{22} = 1 + \left(\frac{C_{11} - C_{22}}{2}\right)\left[\left(\frac{C_{11} - C_{22}}{2}\right)^2 + C_{12}C_{21}\right]^{-1/2} \tag{B.10b}$$

$$(L_2)^*_{12} = -\tfrac{1}{2}(C_{12} + C_{21})\left[\left(\frac{C_{11} - C_{22}}{2}\right)^2 + C_{12}C_{21}\right]^{-1/2} \tag{B.10c}$$

with $(L_a)^*_{ij} = (L_a)^*_{ji}$ and all other terms zero. In axisymmetric analysis

$$(L_3)^*_{33} = 2 \tag{B.11}$$

with all other derivatives of L_3 zero; in plane strain analysis

$$(L_3)^*_{ij} = 0. \tag{B.12}$$

Now we derive the tangent consitutitive tensor. The basic relationship for the constitutive tensor is

$$ {}_oC_{ijrs} = \frac{\partial^2\, {}_oW^D}{\partial L_a\, \partial L_b}(L_a)^*_{ij}(L_b)^*_{rs} + \frac{\partial\, {}_oW^D}{\partial L_a}(L_a)^{**}_{ijrs} + \kappa[({}^tJ_3)^*_{ij}({}^tJ_3)^*_{rs} + ({}^tJ_3 - 1)({}^tJ_3)^{**}_{ijrs}], \tag{B.13}$$

where

$$\frac{\partial^2\, {}_oW^D}{\partial L_1^2} = \sum_{n=1}^{3} \mu_n\left[\left(\frac{\alpha_n}{9} - \frac{1}{3}\right)L_1^{(\alpha_n/2-2)} + \left(\frac{\alpha_n}{36} + \frac{1}{6}\right)[L_2^{\alpha_n/2} + L_3^{\alpha_n/2}]L_1^{-2}\right](L_1L_2L_3)^{-\alpha_n/6} \tag{B.14}$$

and

$$\frac{\partial^2\, {}_oW^D}{\partial L_1\, \partial L_2} = \sum_{n=1}^{3} \mu_n\left[-\frac{\alpha_n}{18}(L_1^{\alpha_n/2} + L_2^{\alpha_n/2}) + \frac{\alpha_n}{36}L_3^{\alpha_n/2}\right] \times (L_1L_2)^{-1}(L_1L_2L_3)^{-\alpha_n/6} \tag{B.15}$$

with suitable permutations of the L_a for the other strain energy derivatives. Also

$$(L_1)^{**}_{1111} = C_{12}C_{21}\left[\left(\frac{C_{11} - C_{22}}{2}\right)^2 + C_{12}C_{21}\right]^{-3/2} \tag{B.16a}$$

$$(L_1)^{**}_{1122} = -(L_1)^{**}_{1111} \tag{B.16b}$$

$$(L_1)^{**}_{1112} = -\left(\frac{C_{11} - C_{22}}{2}\right)C_{12}\left[\left(\frac{C_{11} - C_{22}}{2}\right)^2 + C_{12}C_{21}\right]^{-3/2} \tag{B.16c}$$

$$(L_1)^{**}_{2222} = (L_1)^{**}_{1111} \tag{B.16d}$$

$$(L_1)^{**}_{2212} = -(L_1)^{**}_{1112} \tag{B.16e}$$

$$(L_1)^{**}_{1212} = \left(\frac{C_{11} - C_{22}}{2}\right)^2\left[\left(\frac{C_{11} - C_{22}}{2}\right)^2 + C_{12}C_{21}\right]^{-3/2}, \tag{B.16f}$$

where the symmetries

$$(L_1)^{**}_{ijrs} = (L_1)^{**}_{jirs} = (L_1)^{**}_{ijsr} = (L_1)^{**}_{jisr} \tag{B.17}$$

apply and all of the other second derivatives of L_1 are zero. By inspection,

$$(L_2)^{**}_{ijrs} = -(L_1)^{**}_{ijrs} \tag{B.18}$$

and

$$(L_3)^{**}_{ijrs} = 0. \tag{B.19}$$

Now we consider the special case of repeated roots ($L_1 = L_2$). For this investigation, it is convenient to define

$$A = \frac{C_{11} + C_{22}}{2} \tag{B.20}$$

$$h\cos\theta = \frac{C_{11} - C_{22}}{2} \tag{B.21}$$

$$h\sin\theta = C_{12} \tag{B.22}$$

so that

$$h = \sqrt{\left(\frac{C_{11} - C_{22}}{2}\right)^2 + C_{12}C_{21}} \tag{B.23}$$

(note that C_{12} numerically equals C_{21}). As $h \to 0$, the stretches L_1 and L_2 become equal. Using A, θ, h, we write the stretches

$$L_1 = A + h \tag{B.24a}$$

$$L_2 = A - h, \tag{B 24b}$$

the first stretch derivatives

$$(L_1)^*_{11} = 1 + \cos\theta, \qquad (L_2)^*_{11} = 1 - \cos\theta \tag{B.25a, b}$$

$$(L_1)^*_{22} = 1 - \cos\theta, \qquad (L_2)^*_{22} = 1 + \cos\theta \tag{B.26a, b}$$

$$(L_1)^*_{12} = \sin\theta, \qquad (L_2)^*_{12} = -\sin\theta \tag{B.27a, b}$$

and the second stretch derivatives

$$(L_1)^{**}_{1111} = \frac{\sin^2\theta}{h} \tag{B.28a}$$

$$(L_1)^{**}_{1122} = -\frac{\sin^2\theta}{h} \tag{B.28b}$$

$$(L_1)^{**}_{1112} = -\frac{\sin\theta\cos\theta}{h} \tag{B.28c}$$

$$(L_1)^{**}_{2222} = \frac{\sin^2\theta}{h} \tag{B.28d}$$

$$(L_1)^{**}_{2212} = \frac{\sin\theta\cos\theta}{h} \tag{B.28e}$$

$$(L_1)^{**}_{1212} = \frac{\cos^2\theta}{h}. \tag{B.28f}$$

The first and second stretch derivatives depend on θ, so it appears at first that the stresses and the constitutive tensor also depend on θ when $h = 0$. However, from physical considerations, the stresses and the constitutive tensor do not depend on θ when $h = 0$; therefore the easiest approach is simply to evaluate the stretch derivatives using $\theta = 0$. When this procedure is used, the stresses are evaluated without difficulty. However, the sum

$$\frac{\partial {}^t_0W^D}{\partial L_1}(L_1)^{**}_{1212} + \frac{\partial {}^t_0W^D}{\partial L_2}(L_2)^{**}_{1212} \tag{B.29}$$

requires special attention because $(L_1)^{**}_{1212}$ and $(L_2)^{**}_{1212}$ become unbounded as $h \to 0$. We evaluate (B.29) by expanding $\partial {}^t_0W^D/\partial L_1$ and $\partial {}^t_0W^D/\partial L_2$ as first-order Taylor series in h. The results are

$$\frac{\partial {}^t_0W^D}{\partial L_1} \doteq Q + Rh \tag{B.30a}$$

$$\frac{\partial {}^t_0W^D}{\partial L_2} \doteq Q - Rh, \tag{B.30b}$$

where

$$Q = \sum_{n=1}^{3} \mu_n[\tfrac{1}{6}A^{\alpha_n/2-1} - \tfrac{1}{6}L_3^{\alpha_n/2}A^{-1}](A^2L_3)^{-\alpha_n/6} \tag{B.31}$$

$$R = \sum_{n=1}^{3} \mu_n\left[\left(\frac{\alpha_n}{4} - \frac{1}{6}\right)A^{\alpha_n/2-2} + \tfrac{1}{6}L_3^{\alpha_n/2}A^{-2}\right] \times (A^2L_3)^{-\alpha_n/6}. \tag{B.32}$$

Therefore the sum (B.29) becomes

$$\frac{\partial {}^t_0W^D}{\partial L_1}(L_1)^{**}_{1212} + \frac{\partial {}^t_0W^D}{\partial L_2}(L_2)^{**}_{1212} = (Q + Rh)\left(\frac{1}{h}\right) + (Q - Rh)\left(-\frac{1}{h}\right) = 2R, \tag{B.33}$$

which is well-defined.